Synthesis, Characterization and Unique Properties of a Novel, Completely Aliphatic TAML Activator and Applications of TAML Catalysis for Oxygen Evolution and Pollution Remediation

Dissertation by

Matthew R. Mills

In Partial Fulfillment of the Requirements for the Degree of

Doctor of Philosophy

Thesis advisor

Terrence J. Collins

Carnegie Mellon University

Pittsburgh, Pennsylvania

Submitted 08/05/2016

Abstract

The novel TAML activator **4**, which replaces the aromatic moiety of TAML generation **1** ligands with an aliphatic one, is synthesized and its physical and kinetic properties are characterized. This new catalyst is found to have quite low reactivity at pH 7 compared to catalysts of generations **1**, **2**, and **3**. The stability under oxidative conditions is high compared to these same catalysts, however it is determined that the relationship between the rate of oxidation of the azo dye Orange II, measured by the rate constant k_{II}, and catalyst inactivation, measured by the rate constant k_i, is similar to that of previous catalysts. This provides evidence that oxidation of the aromatic moiety of the ligand is not a significant contributor to the suicidal inactivation of TAML activators. The unique properties of TAML activator **4** stemming from the increased steric bulk are explored, which include the counterintuitive resistance to acid-induced demetalation and the lack of dimerization in the iron(IV) state. The combination of these properties allow for clean cyclic voltammetry studies from pH 2 to 13, which has revealed a proton-coupled electron-transfer mechanism in the electrochemical oxidation of **4** in water. Additionally the iron(V)oxo derivative of **4**, along with a high-spin iron(IV) complex can be prepared in pure water chemically or through bulk electrolysis.

The use of the prototype TAML Activator **1a** for electrocatalytic oxygen evolution under alkaline conditions is explored, with evidence for homogeneous oxygen evolution along with in-situ electrodeposition onto the electrode surface of a heterogeneous catalyst. The turnover frequency of homogeneous electrocatalytic oxygen evolution 1,000 ± 100 s^{-1} is the highest reported for iron-based catalysts operating under alkaline condtions. As a

heterogeneous catalyst, the **1a**-activated electrode exhibits high performance at pH 14 in terms of overpotential, at 400 mV. The combined effects make **1a** one of the best iron-based catalysts for catalytic oxygen evolution under aqueous conditions.

TAML Activators **1a** and **1b** are investigated in the catalytic decomposition of 17α-ethinylestradiol (EE2) with hydrogen peroxide from pH 6 to 9. The rate constant for decomposition of EE2, k_{II}, is found to be $(8.6 \pm 0.5) \times 10^5$ M^{-1} s^{-1}, which is approximately half the rate of horseradish peroxidase-catalyzed oxidation. The ecotoxicity, specifically the estrogenicity, is found to be greatly reduced after TAML/peroxide treatment according to a Yeast Estrogen Screen and an assay using fathead minnows. The TAML/peroxide treatment remains effective in mitigating EE2 in wastewater effluent samples.

Acknowledgements

Six years ago I told my pregnant wife that I wanted to leave my job and go back to grad school. I am somehow still alive to tell this tale. Nikki has been incredibly supportive of this somewhat quixotic endeavor, and I truly could not have done it without her. I cannot express how grateful I am to her for this. We also have two amazing and intelligent sons, Daniel and Calvin. Getting home to see my family provided great incentive to work efficiently

Professor Terry Collins has many traits that make him a great professor, but perhaps the best is that he sees potential more than credentials. Prof. Collins had no qualms over taking on a student from a small school and with limited research experience. I greatly appreciate that he took a chance on accepting me into his research group. His passion for chemistry and sustainability is contagious. The freedom he has allowed me to pursue research projects that excited me enabled my academic growth.

The yin to Terry's yang is Professor Alexander Ryabov, or Sasha. Terry is the architect and Sasha is the contractor who puts all the pieces together. I have learned an incredible amount from Sasha; kinetics, mechanistic study, and the more nuanced skills of how to run experiments efficiently. Sasha has never accepted anything less than my best work, which was incredibly frustrating at times, but I know that it made me a better researcher.

To my fellow group members I also owe a large helping of appreciation. Karla Arias-Salazar was a postdoc in our group when I first arrived. She was a tremendous help in my ability to hit the ground running, as we worked side-by-side for the better part of a year on the degradation of 17α-ethinylestradiol with TAML activators which makes up Chapter 5 of this work. Karla was incredibly supportive, and I like to think that we both made each other more productive. Soumen Kundu, as a senior graduate student, taught me an incredible amount about kinetics and experimentation. He was always willing to answer questions, and the bulk of Chapter 2 stemmed from our discussions on high-

valent states of TAML activators. Matt Denardo has always had good suggestions to offer on mechanism or synthetic techniques, and I feel that our work together, presented in Chapter 1, was mutually beneficial. I have also greatly benefited from the broad range of experience and skills that the rest of my group members have shared with me during my time at CMU. Longzhu Shen, Liang Tang, Genoa Warner, Yogesh Somasundar and Paul Kornbluh have all contributed to this thesis through their willingness to share ideas and help when it was needed.

Of course I would be remiss if I did not acknowledge the horde of undergraduates with whom I had the opportunity to work. Their work has contributed to multiple publications and hopefully several more to come. Abby Burton performed a significant amount of the work presented in Chapter 2 before moving on to initiate a study in the degradation of propranolol. I worked with Austin Cheng for three full years, starting with the summer after his freshman year, and he initiated the study of the difference in the mechanism of degradation of substrates with hypochlorite when catalyzed by TAML activators, which has since furthered significantly by Sam Joyce-Farley. David Zhang has conducted much of the work on the acid-induced demetalation of the new catalyst, which is seen in Chapter 1, and has carried it on further. David Kaplan, Clarissa Enslin, Ximena Olivares, Christopher Schuler, and Dylan Mori also made significant contributions to the work found in this thesis, or in publications that have been or will be submitted soon. These young researchers taught me a lot about mentorship, training and motivation.

The other students at CMU have been very gracious with their time and expertise. Danielle Chirdon got me started with electrochemistry. I've kept Andrew Weitz busy running EPR and Mossbauer samples for me to help establish the presence of iron(V)oxo in water, which is found in Chapter 3.

The faculty in the Department of Chemistry are very supportive and provide a great environment in which to conduct research. I would like to thank Profs. Stefan Bernhard and Kevin Noonan for being in my advisory committee. Profs. Mark Bier and Roberto Gil excel at designing mass spectrometry and NMR experiments, respectively,

and keeping our precious instrumentation in shape. Dr. Gayathri Withers gets so passionate about NMR experiments that sometimes I'll catch her processing my spectra before I can get back to the NMR lab.

I am fortunate to have most of my extended family living in Pittsburgh with me. This has been a tremendous blessing, and their support and encouragement has been greatly appreciated. My wife's family has also been incredibly supportive as well, and I definitely could not have done this without their help as well.

Table of Contents

Index of Figures

Chapter 1

Chapter 2

Chapter 3

Chapter 4

Chapter 5

Index of Tables

Chapter 1

Chapter 2

Index of Schemes

Chapter 1

Chapter 1

Synthesis, Characterization and Catalytic Performance of a Novel Completely Aliphatic TAML Catalyst

1.1 Introduction

Transition-metal catalysts are vital parts in many chemical reactions of both academic and industrial importance. Some catalysts, such as the Grubbs catalysts for olefin metathesis reactions,[1] are well-defined coordination compounds with discrete structures. Others, like the Ziegler-Natta catalysts for olefin polymerization,[2] are complex mixtures of metal salts and reagents. For well-defined coordination compounds, Crabtree has recently written on the importance of analyzing the deactivation of catalysts as a part of the design process.[3] The following is from the introduction of this review (emphasis mine):

> Deactivation leads to loss of catalyst activity or selectivity with increasing reaction time, but has attracted less academic attention in homogeneous catalysis than is justified by its importance. *Ultimate deactivation is inevitable, but catalyst performance can be greatly affected depending on the balance between the rates of deactivation and of productive catalysis.* Even a small improvement in this rate ratio can have a big effect on performance in terms of turnover number (TON) and thus also increases the reaction yield for a given catalyst loading.

The balance between productive catalysis and the rates of deactivation of TAML activators has been the central tenet of Prof. Collins' iterative design cycle for TAML activators (Figure 1-1).[4] As illustrated by the degradation of 17α-ethinylestradiol described in Chapter 5, and in numerous other studies, TAML activators are potent catalysts for the oxidative degradation of organic compounds in water with hydrogen peroxide or other oxidants.[5–12] The iterative design process undertaken by Collins and coworkers served to identify aspects of the ligands that made them susceptible to degradation. Ligands could then be designed to address these weak points. Ultimately this

process resulted in the development of oxidatively stable catalysts capable of performing high numbers of turnovers in a wide range of operating conditions.[13]

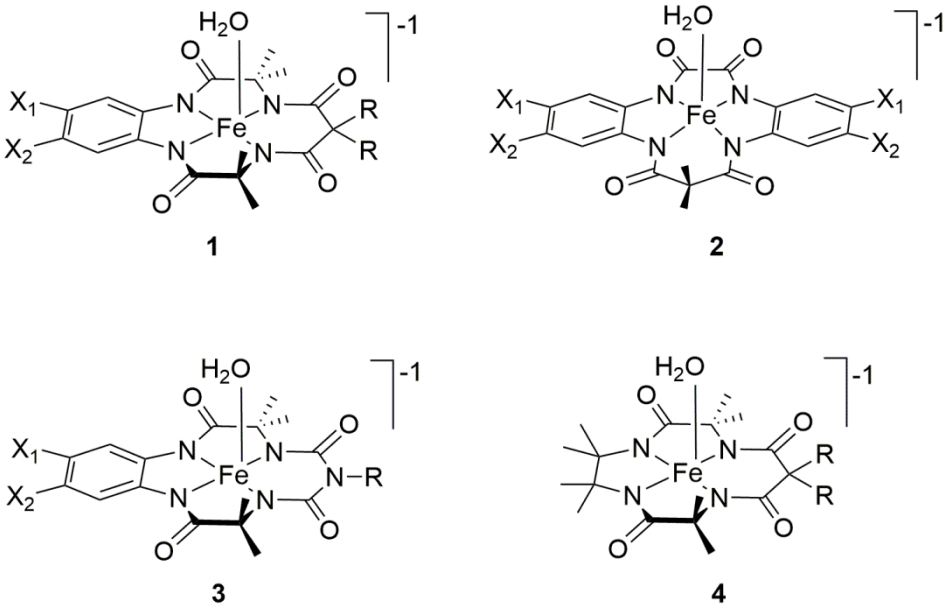

Figure 1-1. Four generations of TAML Activators. Catalyst **4** deviates from the other catalysts by eliminating the aromatic groups in the ligand and is the focus of this work.

Thorough kinetic analysis of the TAML-catalyzed oxidation of organic and inorganic compounds in water has led to the development of the catalytic mechanism described in Scheme 1.[14] The top row of this scheme is the desired 'productive catalysis'. The first step of the catalytic reaction entails an oxidant, usually hydrogen peroxide, taking the resting catalyst (Rc) to the active catalyst (Ac). The Ac then oxidizes the substrate and returns to the resting state for further reactions.

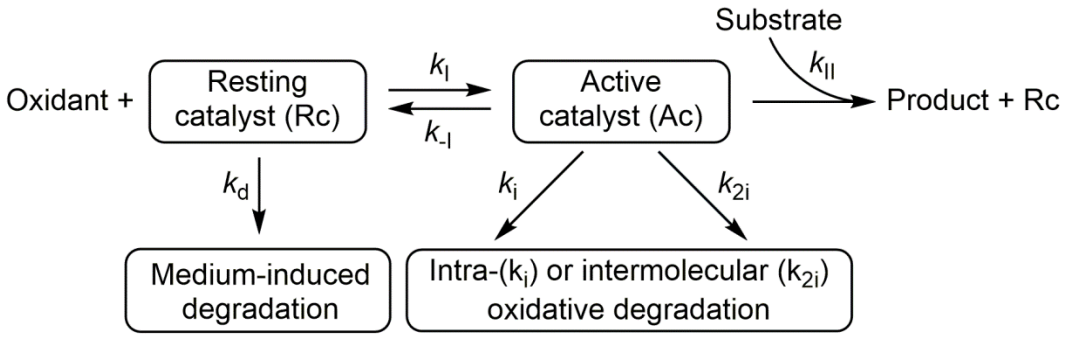

Scheme 1-1. Rate constants associated with TAML-catalyzed degradation of substrates with an oxidant.

$$\frac{-d[\text{Substrate}]}{d\text{t}} = \frac{k_\text{I}k_\text{II}[\text{Fe}][\text{H}_2\text{O}_2][\text{Substrate}]}{k_{-\text{I}} + k_\text{I}[\text{H}_2\text{O}_2] + k_\text{II}[\text{Substrate}]} \qquad (1-1)$$

Equation 1-1 details the rate law for productive catalysis derived from the mechanism shown in Scheme 1–1. The initial rate of substrate oxidation has a linear dependence on total catalyst concentration ([Fe]), and a hyperbolic dependence on hydrogen peroxide and substrate. Plotting the inverse of both reagent and rate allows the determination of both k_I and k_II via the slope and intercept of a double-inverse plot. Conversely, by controlling the concentrations of the reactions in order that k_II[Substrate] >>> $k_\text{I}[\text{H}_2\text{O}_2]$ and assuming that k_{-1} is negligible,[17] Equation 1–1 simplifies to rate = $k_\text{I}[\text{H}_2\text{O}_2]$[Fe]. In the same way, Equation 1–1 simplifies to rate = k_II[Substrate][Fe] when the condition $k_\text{I}[\text{H}_2\text{O}_2]$ >>> k_II[Substrate] holds. Measurement of the initial rates of reaction under conditions in which either formation of Ac or oxidation of substrate is rate-limiting enables the use of pseudo-first order kinetic analysis to determine k_I or k_II, respectively.

The bottom row of Scheme 1–1 represents the primary catalyst deactivation pathways. Medium-induced degradation, described by k_d can be either specific[15] or general[17] acid-induced demetalation. At pH 7, these effects are essentially negligible. Intermolecular oxidative degradation, described by the rate constant k_{2i}, can occur through the oxidation of the ligand of another TAML catalyst. There is also the possibility of two active catalysts comproportionating to form a much less reactive dimer, such as the iron(III)iron(IV) μ-oxo dimer.[18] However, under most operating conditions TAML activators are present in low nanomolar to low micromolar concentrations, which mitigates any intermolecular degradation effects.

While the medium-induced degradation and intermolecular degradation pathways are negligible under normal operating conditions at pH 7, the intramolecular degradation pathway, characterized by k_i is not.[13] Thus, the intramolecular inactivation pathway of the active catalyst is a source of intense interest in our research group, as it apparently holds the key to catalyst longevity.

Recently, a collaboration with a team of mathematicians has verified that the rate constant for the deactivation of the active catalyst can be determined in a straightforward manner under all conditions by measuring the amount of substrate remaining (S_∞) after all catalyst has undergone inactivation.[12] Provided that k_{II} is known, Equation 1–2 can be used to determine the value for k_i.

$$\ln\frac{S_0}{S_\infty} = \frac{k_{II}}{k_i}[\text{TAML}] \qquad (1-2)$$

In Equation 1–2, S_0 is the initial concentration of substrate. The determination of k_i using this technique requires an initial concentration of TAML activator that is much

smaller than would be typically used for kinetic analysis or for effective remediation of the target substrate, as it is necessary that S_∞ be greater than 25% of S_0 for accurate measurements. Using this powerful analytical tool, a fellow student undertook the ambitious project of measuring k_I, k_{II}, and k_i for the TAML activators that had been synthesized to date. This work spanned fourteen catalysts over three generations of TAML activators and revealed that a plot of logk_{II} versus logk_i showed a strong correlation between the two rate constants as seen in Figure 1–2. The catalysts that were more reactive toward substrate oxidation (higher k_{II}) also underwent faster deactivation (higher k_i) and ultimately performed approximately the same number of substrate turnovers.

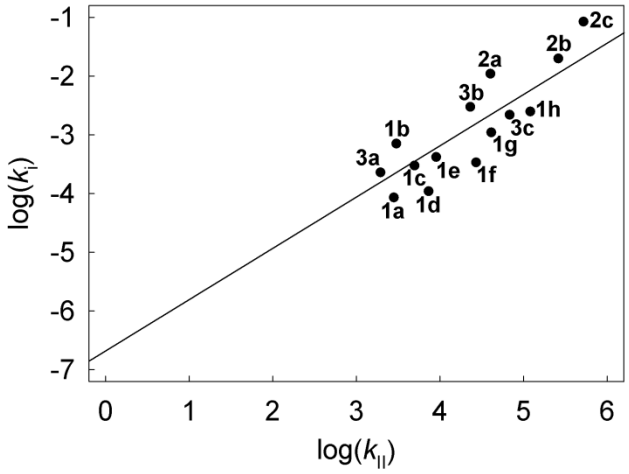

Figure 1-2. Plot of log k_{II} vs. log k_i for fourteen TAML activators. Conditions: 0.01 M pH 7 phosphate buffer, 25 °C, 0.1–1 × 10^{-6} M TAML activator. The catalysts to which the labels correspond can be found in Table 1–1.

In the interest of preparing a catalyst with lower k_i relative to k_{II}, it was proposed to determine whether oxidation of the aromatic moiety of the ligand was a significant

pathway for catalyst inactivation. A previous computational study in our group had identified the aromatic ring of the TAML ligand as a potential source of oxidative degradation.[20] The goal of this study was to synthesize and characterize a new generation of catalyst, which would replace the aromatic moiety with an aliphatic one in order to test whether oxidation of the aromatic moiety of the ligand is a significant contributor to the inactivation of the active catalyst. If so, the newly synthesized catalyst may have a favorable k_{II} to k_i ratio relative to other TAML activators.

1.2 Results and Discussion

1.2.1 Synthesis

The synthesis of catalyst **4** (Figure 1-1) followed the synthetic procedure established for the catalysts of generation **1** with an additional step required to prepare 2,3-diamino-2,3-dimethylbutane from the respective dinitro compound. The synthetic procedure is shown in Scheme 1–2 and described in detail in Section 1.4.3. The overall yield for the ligand is 20% and 6% for the metalated complex relative to the 2,3-dimethyl-2,3-dinitrobutane starting material.

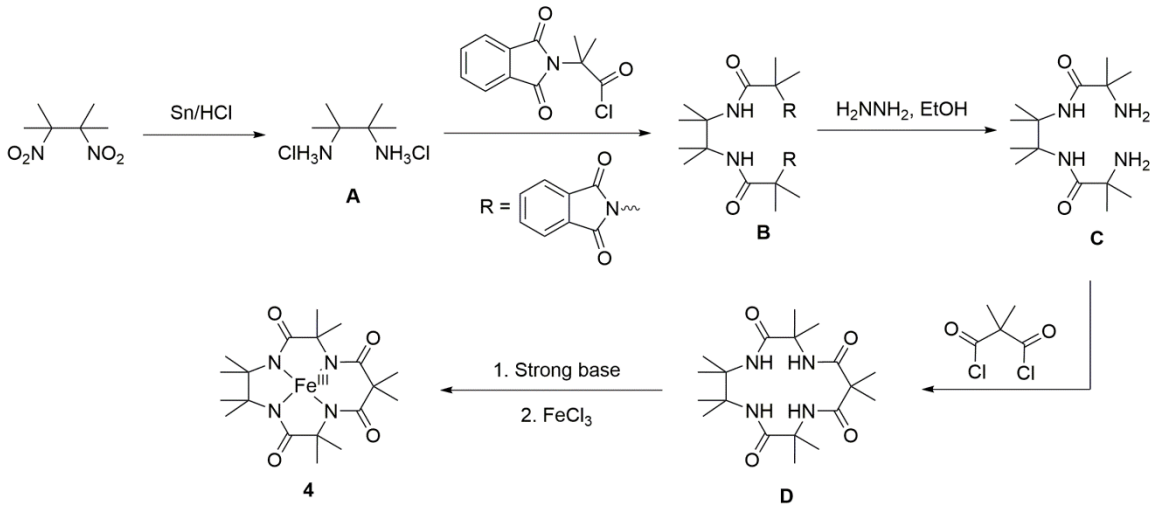

Scheme 1-2. Simplified synthetic scheme for TAML **4**.

1.2.2 Complex Properties

Complex **4** is isolated as a yellow to light orange solid, which is stable in dry air, but is slightly hygroscopic with lithium or sodium as the counterion. If the lithium or sodium cation is replaced with tetramethylammonium, no hygroscopic tendencies are observed. ESI-MS of **4** shows a peak at 434 m/z, which corresponds to **4** with no counterion or axial ligands. Elemental analysis (Section 1.4.3.7) corresponded to the sodium salt with triethylamine, which was used in the mobile phase during chromatographic purification.

The UV-Vis spectrum of **4** also displays features similar to other Fe-TAML catalysts with a peak near 400 nm, which shifts slightly depending on the solvent. The UV-Vis spectrum of complex **4** was found to obey Beer's law at concentrations from 1.35×10^{-5} M to 5.4×10^{-4} M in water and from 1.12×10^{-5} M to 1.19×10^{-4} M in methanol. The extinction coefficients were 7,200 M^{-1} cm^{-1} at 368 nm and 7,800 M^{-1} cm^{-1} at 379 nm in water and methanol, respectively.

Recrystallization of the tetramethylammonium salt of **4** by diffusion of ether into acetonitrile or the evaporation of acetone under anoxic conditions gives small clumps of yellow needles, which do not diffract well enough to attain a crystal structure. Therefore DFT studies were performed in order to gain insight on the structure of the complex (Figure 1-3). It was particularly interesting to analyze the effects brought about by the $(CMe_2)_2$ unit of **4** which replaced the traditional phenylene ring in TAML activators of previous generations (cf. structures **1**–**3**). The aromatic ring is referred to as the "head" part of TAML activators. The calculated geometry of "beheaded" **4** should be compared with the X-ray structural data collected for **1a**.[15] The Fe–O bond is significantly elongated in **4** at 2.285 Å versus 2.097 Å in **1a,** perhaps due to the electron-donating effect of the $(CMe_2)_2$ unit. The iron atom lies just 0.20 Å above the average plane of four deprotonated amide nitrogens versus 0.36 Å in **1a**. In turn, this places the $C(1)H_3$ group very close to the oxygen of the axial water ligand, the C(1)···O separation being 3.415 Å. The latter value matches the sum of the van der Waals radii of CH_3 (2.0) and O (1.4 Å). On the other hand the average Fe–N distance in **4** (1.881) is close to that in **1a** (1.885 Å) suggesting that the $(CMe_2)_2$ unit translates its influence primarily at the axial ligand. As it will be shown below, the Fe–O bond elongation agrees perfectly with a pronounced increase in the pK_a of coordinated water.

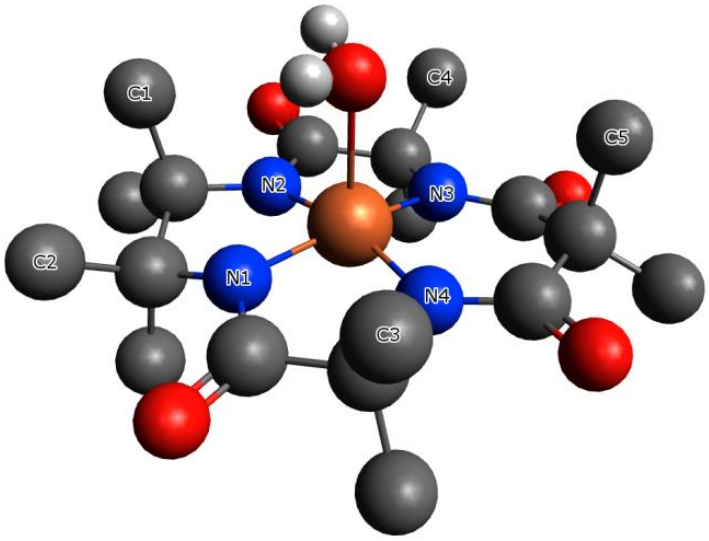

Figure 1-3. Optimized geometry for **4**. Geometry optimized using Gaussian09 with the B3LYP functional and the 6-31G(d) basis set

It is worth noting that the carbon atom periplanar to C1 sits close to Fe, the separation being 3.415 Å. This suggests a steric repulsion between the C atom and the sixth (aqueous) ligand in water, where previous TAMLs are octahedral with two axial H_2O ligands ($[FeL(OH_2)_2]^-$).[17] Optimization of $[FeL(OH_2)_2]^-$ for **4** by DFT in vacuum confirmed this hypothesis. The calculated Fe–O bonds appeared very different, viz. of 2.273 and 3.418 Å, suggesting that one of water ligands should be much more weakly bound to iron(III).

In water, TAML catalysts bind with two axial water ligands, which are susceptible to deprotonation. As discussed previously, the optimized geometry for **4** suggests that only one axial water ligand is strongly bound to the iron center, with the second being weakly bound. The pH-dependent speciation of **4** was thus investigated to

further explore these properties. As the speciation of the complex has large effects on the reactivity, knowing the pK_a is valuable,[21] and is easily measured by spectrophotometric titration (Figure 1-4) as detailed in Section 2.4.3. At pH 7 the spectra of **4** has one dominant peak at 368 nm. This spectrum remains unchanged until approximately pH 9.5, at which point the peak at 368 nm decreases significantly with increasing pH and a smaller peak at 330 nm and a broad peak at 433 nm appear. Clear isosbestic points are seen at 311, 343, and 406 nm, indicating the existence of only two absorbing species in solution. The spectral changes are completely reversible upon changing the pH from 7 to 13 and from 13 to 7, indicating that both the protonated and deprotonated species of **4** are stable under these conditions. The pK_a was determined by fitting the absorbance at 368 nm to Equation 1-3, where A_H, A_{OH}, and A are the absorbance at neutral, basic, and intermediate pH, respectively and setting the slope equal to 1. The pK_a of 11.38 ± 0.01 is the highest yet measured for TAML catalysts by one full pH unit.

$$\log \frac{A_H - A}{A - A_{OH}} = \mathrm{pH} - \mathrm{p}K_a \qquad (1-3)$$

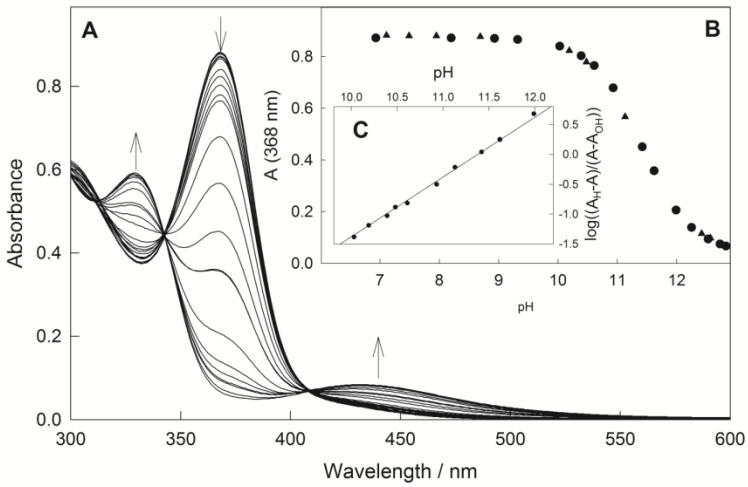

Figure 1-4. Spectrophotometric pH titration of **4**. Figures 4A shows the spectra of **4** from pH 7-13. Figure 4B shows the change in absorbance at the λ_{max} of 368 nm as a function of pH. Circles and triangles are values measured from changing the pH from 7 to 13, and from 13 to 7, respectively Figure 1-4C shows the linearization of data in plot 1-4B to determine the pK_a value. Conditions: 1.2×10^{-4} M **4**, Carmody buffer, 25 °C.

Electron paramagnetic resonance (EPR) data also shows a distinction between the complex of **4** at high and low pH (Figure 1-5). All samples were found to be intermediate spin, S = 3/2. Samples prepared at pH 2 and pH 10.5 are essentially the same, with g = 5.2, D = 1.2 cm^{-1} and E/D = 0.11. . The pH 13 sample showed a significant shift, with g = 4.5, D = 1.3 cm^{-1} and E/D = 0.21. Interestingly, the spectrum obtained at pH 13 contained elements of the spectrum obtained at 10.5, with spin quantitation indicating approximately a 1:1 ratio between the two species. This is difficult to reconcile as **4** has a pK_a value of 11.4, so at pH 13, over 95 % of the complex should be the deprotonated species. A possible explanation is that freezing the sample affects the coordination of the second axial ligand, which DFT studies show is weakly coordinated.

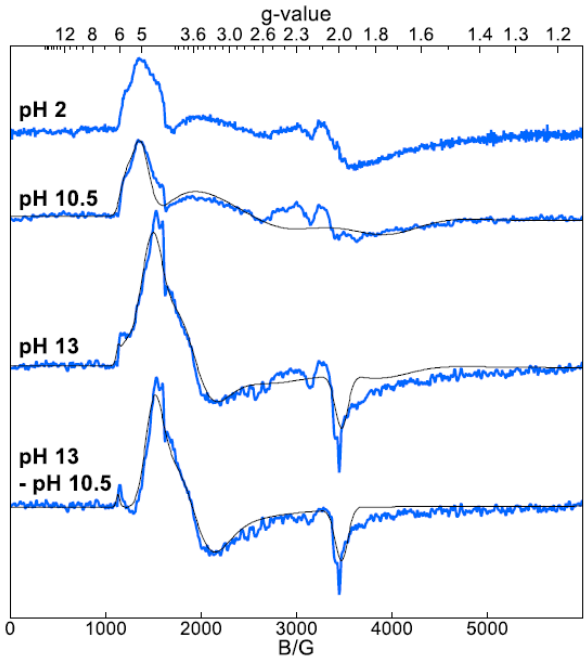

Figure 1-5. EPR spectra of iron(III) **4** showing the speciation at pH 2, 10.5 and 13. Conditions: Samples prepared 5×10^{-4} M **4** in Carmody buffer with 10 % glycerol. EPR spectra recorded as described in Section 1.4.7

1.2.3 Catalytic Bleaching of Orange II in Water with Hydrogen Peroxide

The azo dye Orange II is a convenient substrate for the measurement of the rate constants k_I and k_{II}. Orange II has been used to study oxidative catalysis with enzymes,[22] electrocatalysts,[23] and photocatalysts,[24] among many others. Two plots for the oxidation of Orange II with H_2O_2 catalyzed by **4** at pH 7 are shown in Figure 1-6. Figure 1-6A shows the hyperbolic dependence of the initial rates of bleaching of Orange II as a function of hydrogen peroxide. By plotting the inverse of both initial rate and peroxide concentration, k_I and k_{II} can be obtained from the slope and intercept, respectively. Analysis of this data gives values for k_I and k_{II} of 0.63 ± 0.02 M^{-1} s^{-1} and 1.19 ± 0.03 M^{-1}

s^{-1}, respectively. The k_I at this pH is about 50 times lower than that of catalyst **1a** and three times lower than that of **1b**, the previous lowest activity catalyst. Figure 1-6B shows the linear dependence of the initial rate of Orange II bleaching as a function of Orange II concentration. For most TAML activators, as with many other synthetic oxidation catalysts, it is difficult to obtain such a plot at pH 7, as k_{II} is 2-3 orders of magnitude higher than k_I, and peroxide concentrations much above 10 mM, catalase-like activity becomes non-negligible.[25] Thus, maintaining $k_I[H_2O_2]$ >>> k_{II}[Substrate] becomes difficult over a range where Orange II has significant absorbance. However, for **4** k_i and k_{II} are almost equal and obtaining a linear dependence of initial rate on Orange II concentration is straightforward. The k_{II} value obtained from this plot is 1.11 ± 0.03 M^{-1} s^{-1}, which is in good agreement with the value determined from the double inverse plot.

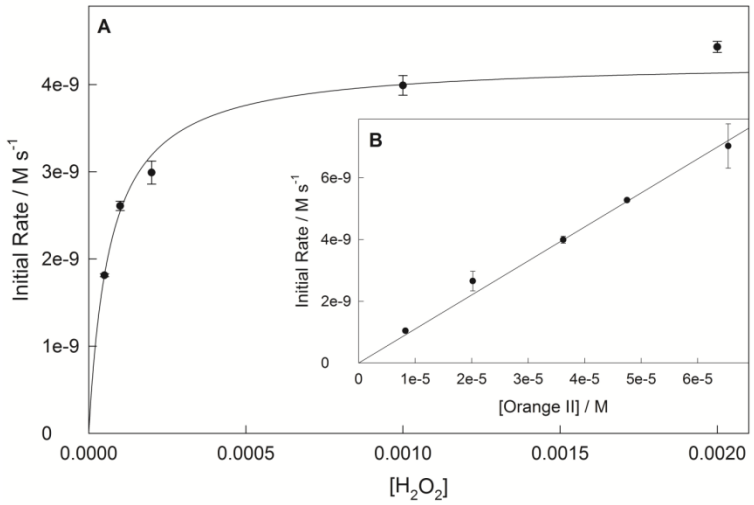

Figure 1-6. Hyperbolic dependence of initial rate of Orange II degradation on $[H_2O_2]$ (A) and linear dependence of initial rate on [Orange II] (B). Conditions: (A), 0.01 M pH 7 phosphate buffer, $1.0x10^{-4}$ M **4**, $3.6x10^{-5}$ M Orange II, 25 ± 1 °C. (B), 1×10^{-3} M H_2O_2, 1×10^{-4} M **4** (See text for details).

1.2.4 Catalytic Rate Constants as a Function of pH

TAML activators are, in general, more effective under basic conditions. In order to assess the effect of pH on the catalytic activity of **4,** the rate constants for the oxidation of Orange II with **4** and hydrogen peroxide were measured from pH 7 to pH 12 (Figure 1-7). The values for k_I show a strong dependence on pH, with a peak value of (1.2 ± 0.03) × 10^3 M^{-1} s^{-1}, which is over three orders of magnitude higher than the value for k_I at pH 7. The high pK_a of **4** drives the maximum reactivity for oxidation of the catalyst to pH 11.75, which is the most basic for TAML activators**.**

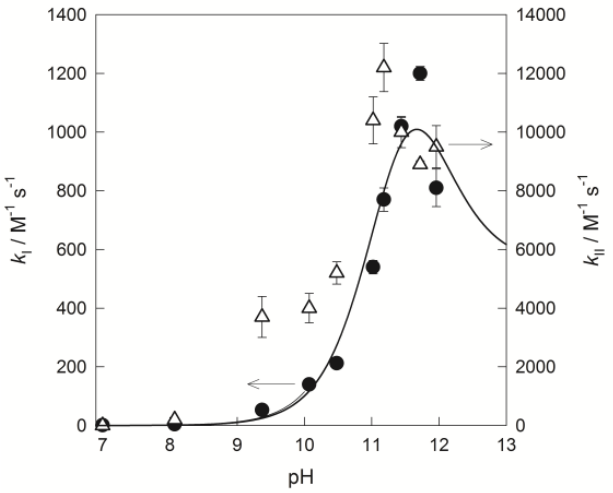

Figure 1-7. Values of k_I and k_{II} as a function of pH. The circles and triangles represent the k_I and k_{II} values respectively. The line is calculated based on the values of the intrinsic rate constants and the measured pK_a values of **4** and hydrogen peroxide.

The values of k_{II} do not have the same pH dependence as for k_I, with a quick rise from 0.85 ± 0.04 M^{-1} s^{-1} to (3.7 ± 0.7) × 10^3 M^{-1} s^{-1} on going from pH 7 to pH 9 followed by a plateau until pH 11 where it rises again to (1.04 ± 0.08) × 10^4 M^{-1} s^{-1}. This reactivity profile is possibly due to the pH-dependent tautomerization of Orange II, which has a pK_a

value of 11.4. A similar phenomenon has been reported by Oakes et al. in the oxidation of azo dyes with peracids wherein the highest observed reaction rates were at a pH intermediate between the pK_a of the peracid and the dye.[26]

The deprotonation of the axial water ligands and H_2O_2 leads to four combinations of reactants for the activation of the catalyst, measured by k_I, and are outlined in Scheme 1–3. This results in the rate constant k_I being divided into four intrinsic rate constants which combine to form k_I according to pH as illustrated by Equation 1–4. The pK_a of **4** is quite close to that of hydrogen peroxide, allowing for a simplification of Equation 1-4 into Equation 1-5, with the assumption that $K_{a1} = K_{a2} = K_a$. The k_I values in Figure 1-7 were fitted manually to Equation 1–4 using 3.16×10^{-12} for K_a, which corresponds to a pK_a value of 11.5, halfway between **4** and hydrogen peroxide.

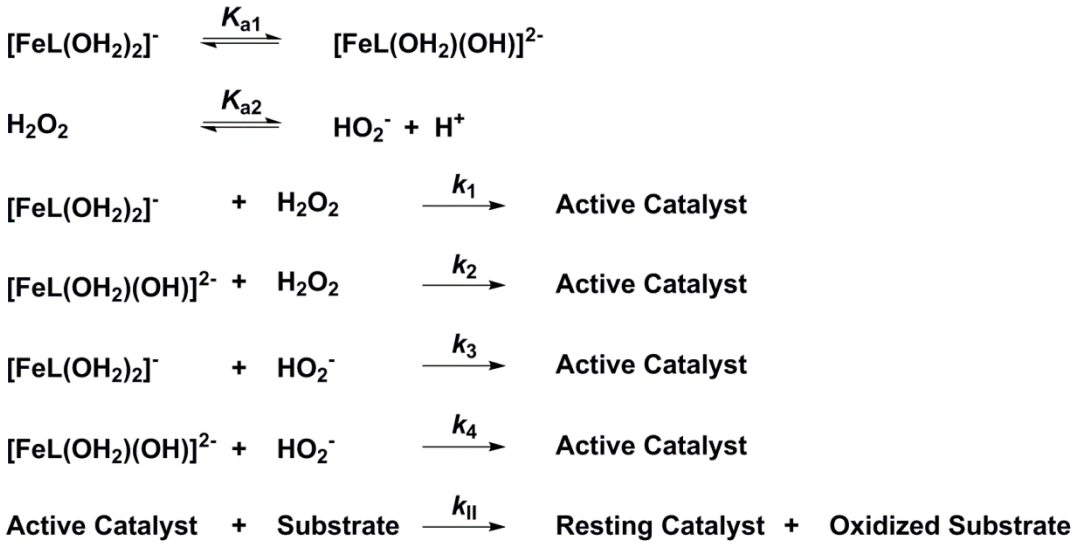

Scheme 1-3. Detailed description of the reactions involving the pH-dependent species found in aqueous systems.

$$k_{\mathrm{I}} = \frac{k_1[\mathrm{H}^+]^2 + (k_2 K_{\mathrm{a1}} + k_3 K_{\mathrm{a2}})[\mathrm{H}^+] + k_4 K_{\mathrm{a1}} K_{\mathrm{a2}}}{[\mathrm{H}^+]^2 + (K_{\mathrm{a1}} + K_{\mathrm{a2}})[\mathrm{H}^+] + K_{\mathrm{a1}} K_{\mathrm{a2}}} \qquad (1-4)$$

$$k_{\mathrm{I}} = \frac{k_1[\mathrm{H}^+]^2 + 2k_{2/3} K_{\mathrm{a}}[\mathrm{H}^+] + k_4 K_{\mathrm{a}}^2}{[\mathrm{H}^+]^2 + 2K_{\mathrm{a}}[\mathrm{H}^+] + K_{\mathrm{a}}^2} \qquad (1-5)$$

The value of 0.63 ± 0.03 M^{-1} s^{-1}, which was measured at pH 7, can be assumed to be the upper limit for the intrinsic rate constant k_1, as fitting the data gives greater than 100% error for this parameter. The low value of this intrinsic rate constant means that the reaction between $[FeL(OH_2)_2]^-$ and HOOH is by far the slowest of the four possible reaction pathways. The value of k_4, for the reaction between $[FeL(OH_2)(OH)]^{2-}$ and HOO^- was determined to be 550 ± 70 M^{-1} s^{-1}, which is two orders of magnitude higher than k_1, due to the higher electron density of both species. The value for $k_{2/3}$, 1,600 ± 200 M^{-1} s^{-1} is a further order of magnitude higher than k_4, indicating that perhaps the electrostatic repulsion of the two deprotonated species at higher pH mitigates the higher reactivity due to increased electron density. The dominant reaction pathway described by $k_{2/3}$, either $[FeL(OH_2)_2]^-$ + HOO^- or $[FeL(OH_2)(OH)]^{2-}$ + HOOH is kinetically indistinguishable, however the increased electron density on the metal center of the $[FeL(OH_2)(OH)]^{2-}$ complex would probably favor the k_2 pathway.

1.2.5 Catalyst Inactivation under Oxidative Conditions

Because TAML activators are powerful oxidative catalysts, they are often capable of oxidizing the products of reaction with the initial substrate, sometimes to the point of mineralization.[19] It is for this reason that turnover number (TON), the number of moles of

product produced per mole of catalyst, is not an adequate parameter to describe TAML activators. Therefore, the relationship between the rate of substrate oxidation and that of catalyst inactivation is the best measure of the overall effectiveness of TAML catalysts. This ratio is ultimately more useful in understanding how modifying the TAML ligand affects the rate of catalyst inactivation. In order to determine the value of k_i for **4** incomplete degradation studies were performed (Figure 1-8).

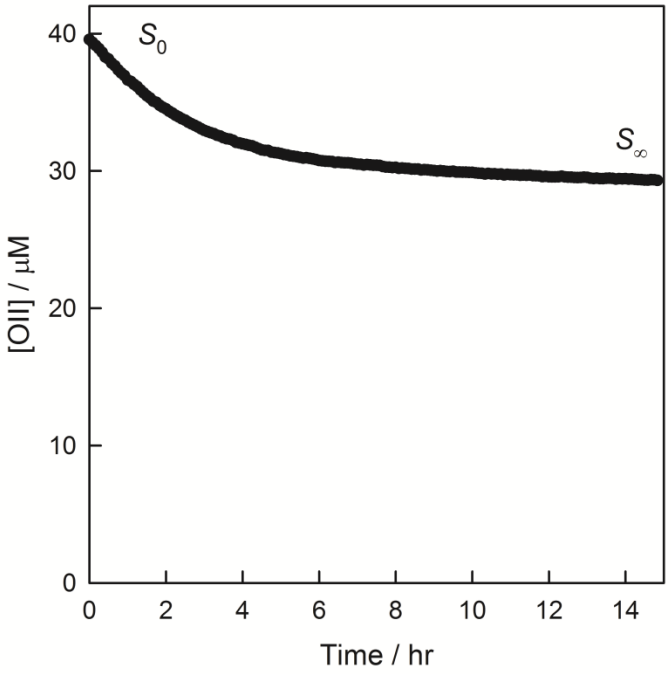

Figure 1-8. Incomplete bleaching of Orange II at pH 7. Conditions: 1 x 10^{-7} M **4**, 2.5 × 10^{-3} M H_2O_2, 0.01 M phosphate buffer, pH 7, 25 °C

Using Equation 1–2 to determine k_i from the values of S_0 and S_∞, a value of (4.1 ± 0.1) × 10^{-7} s^{-1} was calculated, which is the lowest measured value to date. However, when compared to the other TAML activators, the ratio of logk_{II} to logk_i is comparable, as it falls on the same line as that of the previously measured catalysts (Figure 1-9).[27]

Therefore, in conjunction with the correlation between k_{II} and k_i for tail substitution, there is strong evidence against the main degradation pathway being intramolecular oxidation of the aromatic 'head' moiety or the substituents on the 'tail'. Thus, while TAML catalysts are highly tunable in terms of reaction rates, at neutral pH catalysts of generations **1**-**4** perform approximately the same amount of turnovers on a substrate given enough time. This knowledge is inspiring the design of the next generation of TAML activators, which will seek to strengthen the amide units against decomposition.

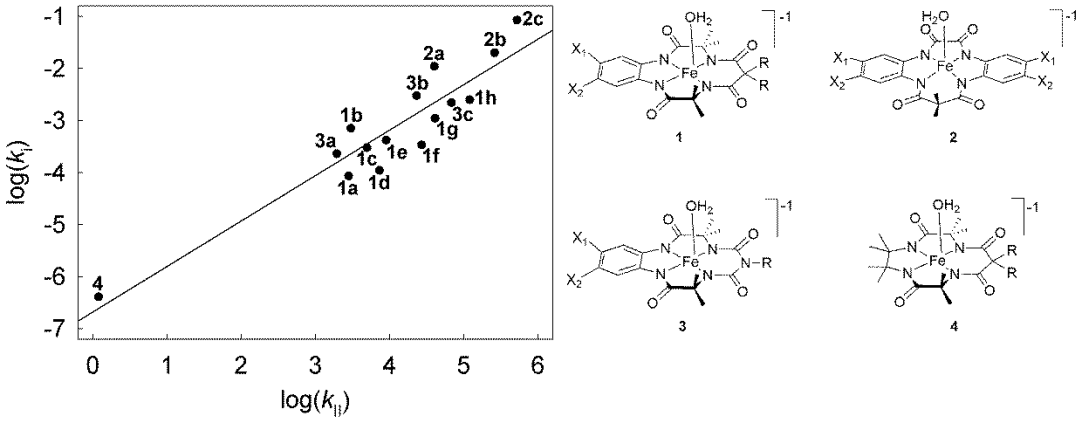

Figure 1-9. Plot of logk_{II} vs. log k_i including catalyst **4**.

Table 1-1. Rate constants k_I, k_{II}, and k_i for fifteen TAML catalysts. Values for catalysts **3a**, **3b**, and **3c** are from reference 28, all others are from reference 27. Conditions: 0.01 M pH 7 phosphate buffer, 25 °C, $1 \times 10^{-7} - 1 \times 10^{-4}$ M TAML activator.

TAML	$X_1/X_2/R$	k_I / M^{-1} s^{-1}	$10^{-4} \times k_{II}$ / M^{-1} s^{-1}	$10^{3} \times k_i$ / s^{-1}
1a	H/H/Et	1.8 ± 0.1	0.28 ± 0.01	0.09 ± 0.01
1b	NH_2/H/Me	28 ± 2	0.42 ± 0.02	1.15 ± 0.07
1c	H/H/Me	31.4 ± 0.1	0.495 ± 0.002	0.30 ± 0.01
1d	CO_2Me/H/Me	38 ± 1	0.73 ± 0.01	0.11 ± 0.01
1e	Me/Me/Me	49 ± 3	0.90 ± 0.05	0.42 ± 0.01
1f	NO_2/H/Me	152 ± 5	2.7 ± 0.2	0.34 ± 0.02
1g	NO_2/H/F	350 ± 2	4.1 ± 0.1	1.1 ± 0.3
1h	Cl/Cl/F	361 ± 1	12 ± 1	2.50 ± 0.03
2a	Cl/Cl/Me	1490 ± 20	4.0 ± 0.2	11.0 ± 0.4
2b	CN/H/Me	1850 ± 90	26 ± 1	20 ± 1
2c	NO_2/H/Me	1900 ± 100	52 ± 7	85 ± 6
3a	H/H/Ph	85 ± 3	0.19 ± 0.01	0.23 ± 0.05
3b	H/H/Me	140 ± 20	2.3 ± 0.2	3.0 ± 0.4
3c	NO_2/H/Me	1500 ± 30	6.8 ± 0.7	2.2 ± 0.3
4	-/-/Me	0.63 ± 0.02	$(1.19 \pm 0.03) \times 10^{-4}$	$(4.1 \pm 0.1) \times 10^{-4}$

1.2.6 Kinetics of Acid-Induced Iron Ejection from 4

The rate of medium-induced degradation at pH 7 in 0.01 M phosphate buffer is negligible for **4**, which was verified by measuring the spectrum of a 1.0×10^{-4} M solution of **4** in 0.01 M pH 7 phosphate buffer every 5 minutes for over 16 hours. After 16 hours the spectrum showed no change, indicating that $k_d \approx 0$ under these conditions. At pH 4 and below TAML **1a** undergoes proton-induced demetalation which occurs according to Equation 1-5.[15] The process is kinetically interesting due to its rate law, viz. $k_{obs} = k_1[H^+]$

+ $k_3[H^+]^3$. The third-order term in H^+ was rationalized by the peripheral protonation of the tail amide oxygens of **1a** because its **1c** analogue with the fluorine tail appeared to be by orders of magnitude more resistant to demetalation.[15]

$$[FeL(OH_2)_2]^- + 4\ H^+ \rightarrow Fe^{III} + H_4L + 2\ OH_2 \qquad (1\text{–}5)$$

According to our present understanding of the demetalation mechanism, **4** should be the most susceptible to acid, as it is by far the most electron-rich TAML activator, as reflected by the pK_a of 11.38. It was with great surprise that **4** was found to be remarkably stable in acidic solution, comparable to the best measured TAML activators, **1h** (X = Cl, R = F) and **1i** (X = H, R = F) (Table 1-1). Therefore, it has been thrilling to probe the concept through the kinetic investigation of reaction represented by Equation 1-5 with complex **4**. It should be emphasized first that **4** is markedly more resistant to H^+ than **1a**, since we were able to manipulate **4** at pH 2 for a span of 8 h without any evidence for its collapse. Correspondingly, the acid-induced demetalation of **4** was studied in the range of $[H^+]$ 0.003–2.5 M by following the exponential decrease in absorbance at 368 nm at 25 °C. Pseudo-first order rate constants k_{obs} depend strictly linearly on $[H^+]$ in the range of 0.003–0.25 M with the corresponding second order rate constant k_1* of (3.41 ± 0.05) × 10^{-4} M^{-1} s^{-1} (Figure 1-10). Above 0.25 M H^+ the dependence of k_{obs} on $[H^+]$ appears to be hyperbolic. There is no evidence for higher-order terms in the acid concentration suggesting that peripheral protonation does not assist the Fe ejection from **4** and the rate-limiting step involves a proton attack at one of the Fe–N bonds as previously proposed.[15] Since the 'beheaded' (tetramethylated) part of **4** could be more susceptible to the electrophilic attack compared to its 'tail' part, it is likely that the proton attacks Fe–N(1) or Fe–N(2) bond (Figure 1-3) Peripheral

protonation of **1** was considered to involve the tail part of TAML.[15] If similar 'tail' protonation occurs in the case of **4**, the actual reactive Fe–N(1) or Fe–N(2) sites are too far away from the protonation site and therefore the peripheral phenomena do not affect the rate of acid-induced demetalation in the case of **4**.

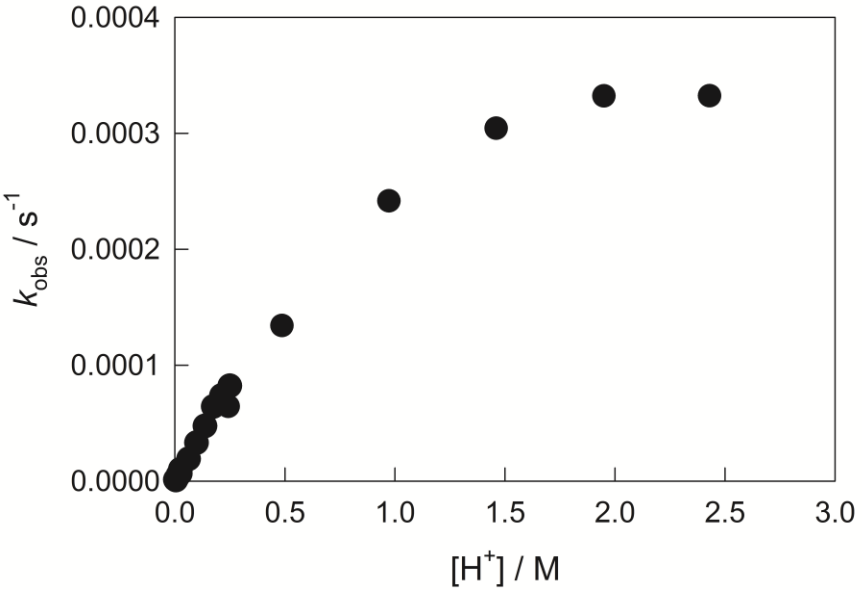

Figure 1-10. Pseudo-first order rate constants k_{obs} versus [H^+] for the demetalation of **4** at 25 °C.

Table 1-2. Rate constants for the acid-induced demetalation of five TAML activators.

TAML	$X_1/X_2/R$	k_1* / M^{-1} s^{-1}	k_3* / M^{-3} s^{-1}
1c	H/H/Me	2.2 ± 0.7	$(6.7 \pm 0.2) \times 10^{5}$
1h	Cl/Cl/F	$(3.7 \pm 0.4) \times 10^{-5}$	$(4.8 \pm 0.6) \times 10^{-5}$
1i	H/H/F	$(1.6 \pm 0.1) \times 10^{-4}$	$(1.6 \pm 0.2) \times 10^{-4}$
3a	H/H/Me	$(3.7 \pm 0.5) \times 10^{-3}$	$(1.04 \pm 0.04) \times 10^{-1}$
4	-/-/Me	$(3.41 \pm 0.05) \times 10^{-4}$	--

The value of k_1* displays 10,000 and 10-fold resistance of **4** to acid compared to TAMLs **1a** and **3a**, with k_1* values of 2.2 ± 0.7 and (3.7 ± 0.5) × 10^{-3} M^{-1} s^{-1} respectively.[15,29] The opposite trend could be anticipated because **4** is more electron-rich than **1a** and therefore should be more prone to electrophilic demetalation. Therefore the retardation might have steric origin. The methyl groups of the $(CMe_2)_2$ unit may function as a fence that prevents the proton attack at Fe–N(1) or Fe–N(2) sites revealing a rare case of steric retardation of the reaction involving specific acid catalysis.[25] This may also explain why there is no indication of a third-order dependence on $[H^+]$ in this concentration range. The lack of a third-order dependence on $[H^+]$ is of great interest, as **4** is just one order of magnitude less resistant to acid in terms of k_1* than the most resistant catalyst, **1h**. However, as **4** exhibits saturation with increasing $[H^+]$ as opposed to a third-order dependence, at extremely high concentrations of H^+ **4** is the most acid-resistant TAML activator yet prepared. In fact, at 2.5 M $[H^+]$ it takes three hours for **4** to completely degrade. This unique acid stability has enabled studies on catalyst oxidation at low pH which were previously impossible and will be discussed in depth in later chapters.

1.3 Conclusion

The novel TAML activator **4,** which has a 'beheaded' ligand replacing the aromatic ring of previous TAML activator with an aliphatic moiety, has been synthesized and characterized. TAML **4** has several features in common with previous TAML activators; axial ligation of water or hydroxide of the iron(III) state which is pH-dependent, the pH dependence of the k_I and k_{II} terms, the S = 3/2 spin state, and, unfortunately, the

correlation of the rate constants k_{II} and k_i. This work has shown that oxidation of the aromatic moiety of TAML activators is not a significant contributor to the catalyst inactivation process measured by k_i. This has reinforced the Collins' group design target for the next generation of TAML activators, which is currently underway.

Of more interest than the similarities of **4** to TAML activators are the differences. Section 1.2.6 discussed the unique stability of **4** toward acid-induced demetalation. Additionally, the increased steric bulk of the added methyl groups of the ligand affect the structure of the oxidized states of **4** in both acetonitrile and water. This will be explored in much greater detail in the following chapters.

1.4 Experimental

1.4.1 Materials

2,3-Dimethyl-2,3-dinitrobutane was purchased from TCI Chemicals and used as received. Dimethylmalonyl chloride and α-aminoisobutyric acid were purchased from Aldrich and used as received. Triethylamine was purchased from Aldrich and distilled over CaH_2. Tetrahydrofuran, acetonitrile, ether and ethanol were dried using a JC Meyer Solvent Dispensing System.

1.4.2 Equipment

All ^{1}H and ^{13}C NMR spectra were recorded with either a Bruker 300 MHZ Avance or Bruker 500 MHz Avance III spectrometer at 300 K. The spectra were analyzed using TopSpin 3.1 software and referenced to the residual solvent peak. Melting points were recorded using a Mel-Temp II.

1.4.3 Synthesis of 4

1.4.3.1 2-Methyl-2-phthalimidopropanoic acid[30]

Phthalic anhydride (35 g, 236 mmol) and α-aminoisobutyric acid (20 g, 194 mmol) were ground together with mortar and pestle and transferred to a 500 mL round-bottom flask. The flask was heated to 190 °C in an oil bath until formation of water vapor ceased (about 45 min), allowed to cool slightly and the contents added to 200 mL saturated $NaHCO_3$. The flask was rinsed with 100 mL saturated $NaHCO_3$ and 100 mL 1% NaOH. The combined aqueous portions were filtered to remove a white insoluble material. Concentrated HCl was added to the filtrate to adjust the pH below 2. A white precipitate formed was collected and dried under vacuum at 70 °C to give 39.2 g (86%) of 2-methyl-2-phthalimidopropanoic acid. ^{1}H NMR ($CDCl_3$) δ 7.81 (m, 2H, ArH), 7.73 (m, 2H, ArH), 1.88 (s, 6H, CH_3). ESI-MS: 232.1 (M – H, MeOH, negative mode). mp 146-148 °C (Lit. 153-154 °C).[17]

1.4.3.1 2-Methyl-2-phthalimidopropanoyl chloride[30]

2-Methyl-2-phthalimidopropanoic acid (23.3 g, 0.1 mol) was weighed into a 250 mL oven-dried round-bottom flask fitted with a reflux condenser. The system was purged with argon, $SOCl_2$ (36 mL, 0.5 mol) was added, the mixture was refluxed for 1 h and allowed to cool to ca. 25 °C. Then, $SOCl_2$ was removed under vacuum. Diethyl ether was added and removed under vacuum twice to eliminate all traces of $SOCl_2$. The resulting material was recrystallized from petroleum ether to yield 2-methyl-2-phthalimidopropanoyl chloride as a colorless solid (15.48 g, 61%). ^{1}H NMR ($CDCl_3$) δ 7.86 (m, 2H, ArH), 7.78 (m, 2H, ArH), 1.93 (s, 6H, CH_3). mp 79 °C (Lit. 79 °C).[31]

1.4.3.3 2,3-Diamino-2,3-dimethylbutane dihydrochloride (A)

2,3-Diamino-2,3-dimethylbutane dihydrochloride was synthesized as previously described[31] applying insignificant modifications. 2,3-Dimethyl-2,3-dinitrobutane (6 g, 34 mmol) was mixed with concentrated HCl (100 mL) at room temperature, the mixture was gently warmed and granulated tin (68.2 g, 0.575 mol) was added in ca. 5 g batches at 10 min intervals. Refluxing for 2 h made the mixture colorless. After cooling on ice, concentrated KOH (45 g in 50 mL H_2O) was added dropwise to give a gray precipitate, which was filtered off through a bed of sand and Celite. The filtrate was distilled until the distillate was no longer basic and the distillate was acidified with concentrated HCl. The remaining water was removed under vacuum to yield 3.91 g of **A** as a white solid (61%). ^{1}H NMR (500 MHz, D_2O) δ 1.55 (s, 6H). ESI-MS: 117.1 (M + H, H_2O, positive mode)

1.4.3.4 *N,N'*-(2,3-Dimethylbutane-2,3-diyl)bis(2-(1,3-dioxoisoindolin-2-yl)-2-methylpropanamide) (B)

A (3.79 g, 20 mmol) was added to a 500 mL round-bottom flask followed by CH_2Cl_2 (250 mL) and NEt_3 (20.9 mL, 0.15 mol). The flask was cooled to 0 °C on ice. 2-Methyl-2-phthalimidopropanoyl chloride (10.6 g, 42 mmol) dissolved in 25 mL CH_2Cl_2 was added dropwise, the mixture was refluxed for 2 h and treated with 150 mL 1 M KOH, 150 mL 0.01 M HCl, 150 mL 1 M HCl and 150 mL brine. The organic layer was separated, dried with $MgSO_4$, filtered and the solvent removed under reduced pressure. The residue was dried under vacuum to give 10.7 g of a light brown, foamy solid, which was dissolved in CH_2Cl_2 and passed through a silica plug to yield 8.89 g of **B** as a white solid, which was used further without purification. ^{1}H NMR (500 MHz, $CDCl_3$) δ 7.74

(m, 4H, ArH), 7.67 (m, 4H, ArH), 6.99 (s, 2H, NH), 1.70 (s, 12H, CH_3), 1.39 (s, 12H, CH_3). ESI-MS: 545.4 (acetonitrile, negative mode).

1.4.3.5 *N*,*N*'-(2,3-Dimethylbutane-2,3-diyl)bis(2-amino-2-methylpropanamide) (C)

B (8.89 g, 16.2 mmol) was dissolved in 250 mL ethanol and heated to near reflux. Hydrazine hydrate (64% hydrazine, 1.65 mL, 34 mmol) was added and the mixture was refluxed using an oil bath at 98 °C for 18 h. The solvent was removed under reduced pressure and 2 M HCl (500 mL) added. The mixture was heated at 80 °C for 10 min, cooled to room temperature, filtered, the pH of the filtrate was adjusted to 12 with solid KOH (55 g) after which the reaction mixture turned a faint pink and then yellow. After extraction with 4×150 mL CH_2Cl_2 and drying with $MgSO_4$, the solvent was removed under reduced pressure to give 4.15 g of **C** (73%, based on **A**) as a white solid. ^{1}H NMR (500 MHz, $CDCl_3$) δ 8.33 (br, 2H, NH), 1.51 (br, 4H, NH_2), 1.43 (s, 12H, CH_3), 1.33 (s, 12H, CH_3). ^{13}C NMR (126 MHz ,d_6-DMSO) δ 178.42, 60.59, 55.38, 28.92, 22.14. ESI-MS: 287.1 (M + H, methanol, positive mode).

1.4.3.6 2,2,5,5,6,6,9,9,12,12-Decamethyl-1,4,7,10-tetraazacyclotridecane-3,8,11,13-tetraone (D)

Triethylamine (1.23 mL, 8.8 mmol) was mixed with 20 mL THF in a 100 mL round-bottom flask. Dimethylmalonyl chloride (0.528 mL, 4 mmol) and **C** (1.14 g, 4 mmol) were dissolved in 20 mL THF each and placed in two syringes. These solutions were added to the flask in a matter of 2 h at 0 °C with stirring. The mixture was then warmed to ca. 25 °C, stirred for 2 h, filtered, and the solvent removed under reduced pressure to give a white solid, which was recrystallized from ethyl acetate to yield **D** (652 mg, 43%

based on **C**). ^{1}H NMR (500 MHz, d_6-dmso) δ 7.62 (s, 2H, NH), 5.81 (s, 2H, NH), 1.42 (s, 6H, CH_3), 1.30 (s, 12H, CH_3), 1.27 (s, 12H, CH_3). ^{13}C NMR (126 MHz ,d_6-dmso) δ 172.78, 171.18, 61.82, 58.26, 51.92, 21.30 ESI-MS: 383.3 (M – H, methanol, positive mode).

1.4.3.7 TAML Activator 4

Macrocycle **D** (100 mg, 0.26 mmol) was dissolved in 20 mL dry THF in a 50 mL 3-neck round-bottom flask and cooled to 0 °C with an ice bath. Sodium hexamethyldisilazane (0.52 mL of a 2 M solution in THF, 1.04 mmol) was added and the mixture was stirred for 30 min to form a yellowish precipitate. Then, $FeCl_3$ (47 mg, 0.37 mmol) was added and the mixture was stirred for 16 h to produce a brown precipitate. The solvent was removed in vacuo and the residue was purified by column chromatography on basic alumina using CH_2Cl_2/MeOH/NEt_3 (90%/5%/5%) to give **4** as an orange solid (45 mg, 31%). ESI-MS: 434 (M, methanol, negative mode). This is the expected mass of the anionic complex without axial ligands. Anal.: found C, 53.32; H, 7.72; N, 13.01. $Na[Fe^{III}\{(Me_2CNCOCMe_2NCO)_2CMe_2\}NMe_3]$: C, 53.76; H, 8.12; N, 12.54%.

1.4.4 Spectrophotometric Titration

A universal buffer (Carmody buffer) consisting of 0.1 M boric acid, 0.025 M citric acid and 0.05 M K_3PO_4 was used to prepare a 0.12 mM solution of **4** at pH 7.[33] Concentrated KOH and H_3PO_4 were used for further pH adjustments. The spectral data were collected using a double beam Shimadzu UV-1800 instrument.

1.4.5 Kinetic Studies

Kinetic studies were conducted at 25 °C in 0.01 M phosphate buffer. Stock solutions of **4**, Orange II, and H_2O_2 were prepared in HPLC grade water. Appropriate volumes of the buffer, compound **4** and Orange II were added to polystyrene cuvettes and the reactions were initiated by the addition of an aliquot of H_2O_2. Reaction progress was followed by measuring the decrease in absorbance at 484 nm (λ_{max} for Orange II, $\varepsilon = 2.1\times10^4$ M^{-1} cm^{-1} at pH 7-10) using an HP 8453 diode array spectrophotometer with an eight-cell changer. Above pH 10 the following values of ε were used 17180, 14850, 12750, and 11,230 M^{-1} cm^{-1} at pH 10.5, 11, and 11.4 and 11.72 respectively. The initial rates were calculated from linear plots of Orange II concentration vs time when the conversion of the dye did not exceed 10%. Each data point reported is a mean value of at least three measurements.

1.4.6 EPR Spectroscopy

EPR Spectroscopy X-band EPR spectra was recorded on a Bruker 300 spectrometer equipped with an Oxford ESR-910 liquid helium cryostat. The signal was quantified relative to a CuEDTA spin standard. For both instruments, the microwave frequency was calibrated with a frequency counter and the magnetic field with an NMR gaussmeter. A modulation frequency of 100 kHz was used for the EPR spectra. The EPR simulation software (Spin Count) was written by one of the authors.[34] The software diagonalizes the spin Hamiltonian, (Equation 1–6) where S is the total spin of the complex (unless explicitly stated otherwise) and the parameters have the usual definitions. The quantitative simulation was least-squares fit of the experimental spectra generated with

consideration of the intensity factor, which allows the computation of simulated spectra for a specified sample concentration.

$$\mathrm{H} = \beta \mathrm{eBgS} + \mathrm{S.D.S} + \mathrm{S.A.I} \qquad (1-6)$$

1.5 References

1. Schwab, P.; Grubbs, R. H.; Ziller, J. W. *J. Am. Chem. Soc.* **1996**, *118*, 100–110.

2. Corradini, P.; Guerra, G.; Cavallo, L. *Acc. Chem. Res.* **2004**, *37*, 231–241.

3. Crabtree, R. H. *Chem. Rev.* **2015**, *115*, 127–150.

4. Collins, T. J. *Acc. Chem. Res.* **2002**, *35*, 782–790.

5. Mitchell, D. A.; Ryabov, A. D.; Kundu, S.; Chanda, A.; Collins, T. J. *J. Coord. Chem.* **2010**, *63*, 2605–2618.

6. Kundu, S.; Chanda, A.; Espinosa-Marvan, L.; Khetan, S. K.; Collins, T. J. *Catal. Sci. Technol.* **2012**, *2*, 1165.

7. Kundu, S.; Chanda, A.; Khetan, S. K.; Ryabov, A. D.; Collins, T. J. *Environ. Sci. Technol.* **2013**, *47*, 5319–5326.

8. Shen, L. Q.; Beach, E. S.; Xiang, Y.; Tshudy, D. J.; Khanina, N.; Horwitz, C. P.; Bier, M. E.; Collins, T. J. *Environ. Sci. Technol.* **2011**, *45*, 7882–7887.

9. Sen Gupta, S.; Stadler, M.; Noser, C. A.; Ghosh, A.; Steinhoff, B.; Lenoir, D.; Horwitz, C. P.; Schramm, K. W.; Collins, T. J. *Science* **2002**, *296*, 326–328.

10. Shappell, N. W.; Vrabel, M. A.; Madsen, P. J.; Harrington, G.; Billey, L. O.; Hakk, H.; Larsen, G. L.; Beach, E. S.; Horwitz, C. P.; Ro, K.; Hunt, P. G.; Collins, T. J. *Environ. Sci. Technol.* **2008**, *42*, 1296–1300.

11. Chanda, A.; Khetan, S. K.; Banerjee, D.; Ghosh, A.; Collins, T. J. *J. Am. Chem. Soc.* **2006**, *128*, 12058–12059.

12. Emelianenko, M.; Torrejon, D.; DeNardo, M. A.; Socolofsky, A. K.; Ryabov, A. D.; Collins, T. J. *J. Math. Chem.* **2014**, *52*, 1460–1476.

13. Collins, T. J. *Acc. Chem. Res.* **1994**, *27*, 279–285.

14. Chanda, A.; Ryabov, A. D.; Mondal, S.; Alexandrova, L.; Ghosh, A.; Hangun-Balkir, Y.; Horwitz, C. P.; Collins, T. J. *Chem.—Eur. J.* **2006**, *12*, 9336–9345.

15. Ghosh, A.; Ryabov, A. D.; Mayer, S. M.; Horner, D. C.; Prasuhn, D. E.; Gupta, S. Sen; Vuocolo, L.; Culver, C.; Hendrich, M. P.; Rickard, C. E. F.; Norman, R. E.; Horwitz, C. P.; Collins, T. J. *J. Am. Chem. Soc.* **2003**, *793*, 12378–12379.

16. Ellis, W. C.; Tran, C. T.; Roy, R.; Rusten, M.; Fischer, A.; Ryabov, A. D.; Blumberg, B.; Collins, T. J. *J. Am. Chem. Soc.* **2010**, *132*, 9774–9781.

17. Polshin, V.; Popescu, D. L.; Fischer, A.; Chanda, A.; Horner, D. C.; Beach, E. S.; Henry, J.; Qian, Y. L.; Horwitz, C. P.; Lente, G.; Fabian, I.; Münck, E.; Bominaar, E. L.; Ryabov, A. D.; Collins, T. J. *J. Am. Chem. Soc.* **2008**, *130*, 4497–4506.

18. Tang, L. L.; Gunderson, W. A.; Weitz, A. C.; Hendrich, M. P.; Ryabov, A. D.; Collins, T. J. *J. Am. Chem. Soc.* **2015**, *137*, 9704–9715.

19. Chahbane, N.; Popescu, D.-L.; Mitchell, D. A.; Chanda, A.; Lenoir, D.; Ryabov, A. D.; Schramm, K.-W.; Collins, T. J. *Green Chem.* **2007**, *9*, 49–57.

20. Chanda, A.; Popescu, D.; Oliveira, F. T. De; Bominaar, E. L.; Ryabov, A. D.; Mu, E.; Collins, T. J. *J. Inorg. Biochem.* **2006**, *100*, 606–619.

21. Kundu, S.; Annavajhala, M.; Kurnikov, I. V.; Ryabov, A. D.; Collins, T. J. *Chem.—Eur. J.* **2012**, *18*, 10244–10249.

22. Fertinger, C.; Hessenaue-Ilicheva, N.; Franke, A.; Van Eldik, R. *Chem.—Eur. J.* **2009**, *15*, 13435–13440.

23. Duan, T.; Chen, Y.; Wen, Q.; Duan, Y.; Qi, L. *J. Electrochem. Soc.* **2016**, *163*, H499–H507.

24. Li, R.; Song, X.; Huang, Y.; Fang, Y.; Jia, M.; Ma, W. *J. Mol. Catal. A Chem.* **2016**, *421*, 57–65.

25. Ghosh, A.; Mitchell, D. A.; Chanda, A.; Ryabov, A. D.; Popescu, D. L.; Upham, E. C.; Collins, G. J.; Collins, T. J. *J. Am. Chem. Soc.* **2008**, *130*, 15116–15126.

26. Oakes, J.; Gratton, P. *J. Chem. Soc. Perkin Trans. 2* **1998**, 1857–1864.

27. Denardo, M. A.; Mills, M. R.; Ryabov, A. D.; Collins, T. J. *J. Am. Chem. Soc.* **2016**, *138*, 2933–2936.

28. Warner, G. R.; Mills, M. R.; Enslin, C.; Pattanayak, S.; Panda, C.; Panda, T. K.; Gupta, S. Sen; Ryabov, A. D.; Collins, T. J. *Chem.—Eur. J.* **2015**, *21*, 6226–6233.

29. Panda, C.; Ghosh, M.; Panda, T.; Banerjee, R.; Sen Gupta, S. *Chem. Commun.* **2011**, *47*, 8016–8018.

30. Ghosh, A.; Ramidi, P.; Pulla, S.; Sullivan, S. Z.; Collom, S. L.; Gartia, Y.; Munshi, P.; Biris, A. S.; Noll, B. C.; Berry, B. C. *Catal. Letters* **2010**, *137*, 1–7.

31. Al-Hassan, S. S.; Cameron, R. J.; Curran, A. W. C.; Lyall, W. J. S.; Nicholson, S. H.; Robinson, D. R.; Stuart, A.; Suckling, C. J.; Stirling, I.; Wood, H. C. S. *J. Chem. Soc. Perkin Trans. 1* **1985**, 1645–1659.

32. Sayre, R. *J. Am. Chem. Soc.* **1955**, *77*, 6689–6690.

33. Carmody, W. R. *J. Chem. Educ.* **1961**, *38*, 559.

34. Petasis, D. T.; Hendrich, M. P. Iron-Sulfur Clusters in Chemistry and Biology; Rouault, T. A., Ed.; De Gruyter: Berlin, **2014**.

Chapter 2

Iron(IV) or Iron(V)? Heterolytic or Free Radical? Oxidation Pathways of TAML Activators in Acetonitrile at −40 °C

2.1 Introduction

As described in Chapter 1, TAML activators are remarkably effective synthetic peroxidase mimics. With TAML activators, as well as with other catalysts, it is of great interest to understand the full mechanism of the catalytic process. Understanding of the mechanism of catalytic oxidation of organic substrates can aid in the design of more effective catalysts by modifying ligands to emphasize a desired interaction or minimize an undesired one.[1,2] Further, mechanistic understanding can also improve reaction rates and/or selectivity by guiding the choice of reaction conditions. As TAML activators have been increasingly used as catalysts in organic synthesis, this understanding grows in importance.[3–10]

The mechanism for the oxidation of substrates with hydrogen peroxide catalyzed by TAML activators was discussed in Chapter 1 (Scheme 1-1). As part of this mechanism, the resting-state catalyst is oxidized by peroxide to give the "active catalyst". This active catalyst has long been proposed to be an iron(V)oxo species, which is in contrast to the peroxidase enzymes, which utilize an iron(IV)oxo iron center with a porphyrin radical cation, known as Compound I.[11] A number of high-valent iron TAML species have been characterized under various conditions, including iron(IV)(μ-oxo) dimer in acetonitrile and water,[12–15] iron(IV)oxo in water,[13] iron(IV)-chloro and cyano complexes[16] in acetonitrile, and an iron(V)oxo complex in acetonitrile at -40 °C (Figure 2-1).[17]

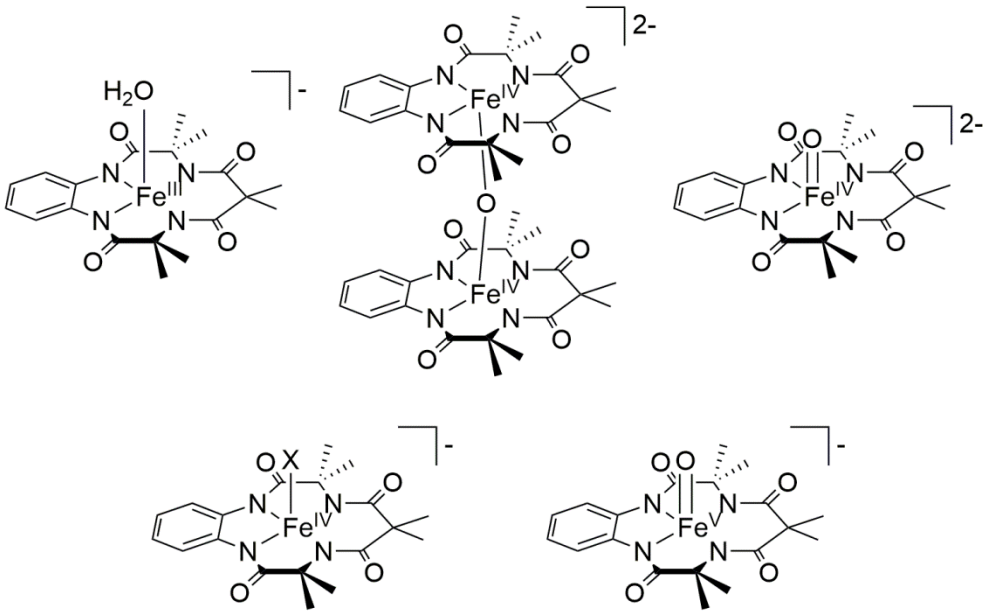

Figure 2-1. Various oxidized states of 1a. Fe(III) resting state (A), Fe(IV) µ-oxo dimer (B), Fe(IV)-oxo (C), Fe(IV)-chloride or cyanide (D), Fe(V)-oxo (E).

Generally in synthetic reactions utilizing TAML catalysts, a mechanism for catalysis is proposed which involves high-valent oxidation states of iron. In the interest of encouraging the broader use of TAML activators, we sought to clarify the oxidation states that result from the reaction of TAML activators with a variety of oxidants. As the iron(V)oxo complex had, to this point, only been observed in nitrile solvents below -40 °C, and with the extensive background work already done,[3,18,19] it was decided to use these conditions for this study. However, it should be noted that the iron(V)oxo derivative of 'biuret' TAML activator **3a** has been prepared at room temperature in acetonitrile.[20]

2.2 Results and Discussion

2.2.1 Oxidation of TAML activator 1a with *meta*-chloroperoxybenzoic acid

In nitrile solvents below -40 °C, the addition of 0.5 equivalents of *meta*-chloroperoxybenzoic acid (*m*CPBA) to a solution of **1a** or **1b** results in the formation of the iron(IV)(μ-oxo) dimer, which is easily followed by UV-vis spectroscopy (Figure 2-2, left).[3,17] Another 0.5 equivalents of *m*CPBA yields the iron(V)oxo species (Figure 2-2, right).

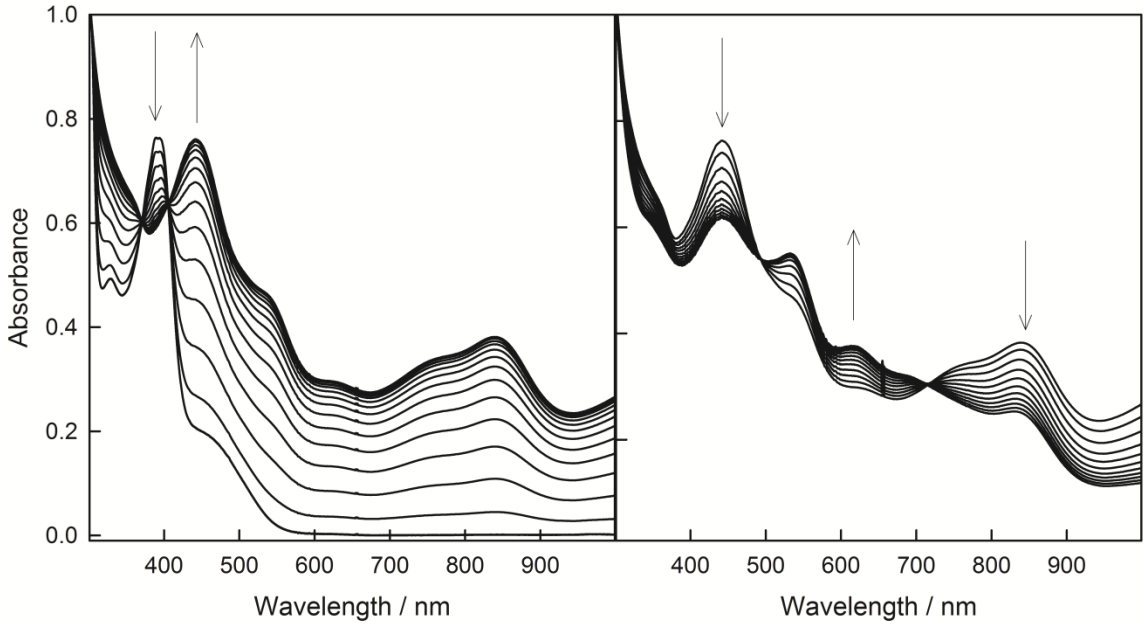

Figure 2-2. UV-Vis spectra of the reaction of **1a** with 0.5 equivalents *m*CPBA (left) and one equivalent *m*CPBA (right). The spectra indicate a transition from iron(III) to iron(IV) μ-oxo dimer (left) and from iron(IV)(μ-oxo) dimer to iron(V)oxo (right). Conditions: 1×10^{-4} M **1a**, 1×10^{-4} M *m*CPBA, -40 °C. Spectra recorded every 20 s (left) and 300 s (right).

2.2.2 Oxidation of 1a with different oxidants

As TAML activators are capable of catalytically activating a variety of stoichiometric oxidants, it was of interest to study the oxidation of **1a** with a variety of oxidants to determine the kinetics of oxidation and whether all oxidants could convert **1a** to the iron(V) species. The most immediate observation was that the strong oxo-transfer reagents *m*CPBA and sodium hypochlorite (NaClO) both converted **1a** to the iron(IV)(μ-oxo) dimer very rapidly, followed by significantly slower conversion to the iron(V)oxo monomer. The reaction with *m*CPBA is essentially quantitative with only 0.5 equivalents of *m*CPBA required to yield the iron(IV)(μ-oxo) dimer and another 0.5 equivalents needed to produce the iron(V)oxo species. The other oxidants tested; hydrogen peroxide, *tert*-butyl hydroperoxide (TBHP), *tert*-butyl peroxide, and benzoyl peroxide; were able to convert **1a** to the iron(IV)(μ-oxo) dimer, albeit at lower yields than with *m*CPBA or NaClO (Table 2-1). However, no appreciable conversion to the iron(V)oxo species was observed with these oxidants. It should be noted that the iron(V)oxo species of **1a** can be spontaneously reduced in acetonitrile to form the iron(IV)(μ-oxo dimer),[3,19] so the lack of observed iron(V)oxo species does not necessarily preclude the formation of iron(V) under these conditions. However, if the iron(V)oxo derivative is formed, the rate of oxidation of iron(IV)(μ-oxo) dimer to iron(V) is much slower than the spontaneous reduction to iron(IV).

Table 2-1. Comparison of the products of oxidation of **1a** with different oxidants. Conditions: 1×10^{-4} M **1a**, acetonitrile, -40 °C.

Oxidant	[Ox] / M	Product and yield	Reaction time
*m*CPBA	1×10^{-4}	Fe(IV): 99%	Fe(IV): 100 s
		Fe(V): 95%	Fe(V): 60 min
NaClO	2×10^{-4}	Fe(IV): 99%	Fe(IV): 5 s
		Fe(V): 95%	Fe(V): 30 min
Benzoyl peroxide	5×10^{-3}	Fe(IV): 90%	Fe(IV): 84 min
tert-Butylperoxide	6×10^{-2}	Fe(IV): 89%	Fe(IV): 185 min
Hydrogen peroxide	1×10^{-2}	Fe(IV): 83%	Fe(IV): 83 min
tert-Butylhydroperoxide	7.3×10^{-3}	Fe(IV): 89%	Fe(IV): 20 min

The difference in final oxidation state is interesting for two reasons. First, the iron(V)oxo species reacts with sulfides in acetonitrile over 10,000 times faster than the iron(IV)(μ-oxo) dimer.[3] This extreme difference in reactivity exemplifies the desire to optimize the conditions for which the iron(V)oxo species is produced as part of the catalytic cycle. The second reason of interest for the final oxidation product is that the conversion of iron(III) to the iron(IV)(μ-oxo) dimer is proposed to occur through the intermediacy of iron(V)oxo, which comproportionates with an unreacted iron(III) to form the dimer (Scheme 1-1). This proposed mechanism is harder to rationalize with the oxidants that are unable to produce the iron(V)oxo species in any measurable amount.

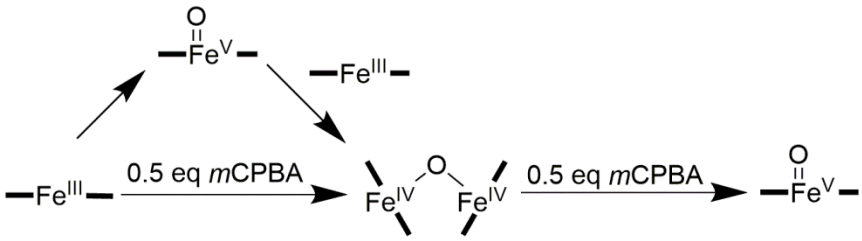

Scheme 2-1. Proposed mechanism for the formation iron(IV) µ-oxo dimer and iron(V)oxo with mCPBA. The formation of the iron(IV)(µ-oxo) dimer is thought to occur by oxidation of the initial iron(III) species to iron(V)oxo. The iron(V)oxo then comproportionates with unreacted iron(III) to yield the iron(IV)(µ-oxo) dimer.

2.2.3 Oxidation of 4 with *m*CPBA and TBHP

The direct oxidation of iron(III) to iron(V)oxo prior to comproportionation to form the iron(IV)(µ-oxo) dimer was tested with the recently synthesized catalyst **4**. This catalyst was found to have disappointing reactivity toward the dye Orange II with hydrogen peroxide at pH 7 (see Chapter 1). However, this new complex was of interest in this study due to the greatly increased steric bulk that the four aliphatic methyl groups introduced relative to **1a** (Figure 2-3). It was proposed that this steric bulk could block the formation of a dimer. This could help to 'trap' an intermediate iron(V)oxo species if one is formed en route to the iron(IV) µ-oxo dimer.

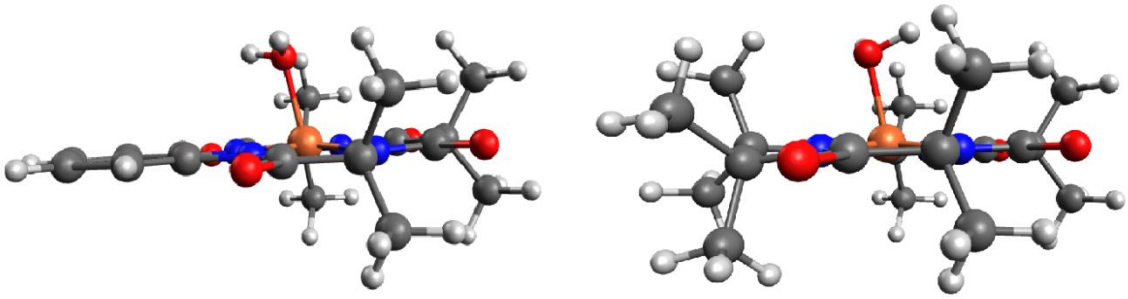

Figure 2-3. DFT structures of **1a**, left, and **4**, right, showing the increased steric bulk of catalyst **4**.

The direct conversion of iron(III) to iron(V)oxo was first tested with *m*CPBA under the same conditions as were applied to **1a**. After the addition of 0.5 equivalents of *m*CPBA, the UV-Vis spectrum changed as shown in Figure 2-4 (left) with clear isosbestic points at 301, 330, 370, and 414 nm, indicating the conversion of the starting iron(III) species to a distinct product. After the addition of another 0.5 equivalents of *m*CPBA, the spectral changes continue in the same manner, with unchanged isosbestic points. Again, this indicates that all of the initial iron(III) species has been converted into one distinct species. The same spectral changes are observed when an excess of *m*CPBA is added (Figure 2-4, right). The stability of this iron(V)oxo species is quite high relative to catalysts **1a** and **1b**, with the final spectrum showing neglible changes over the course of one hour.

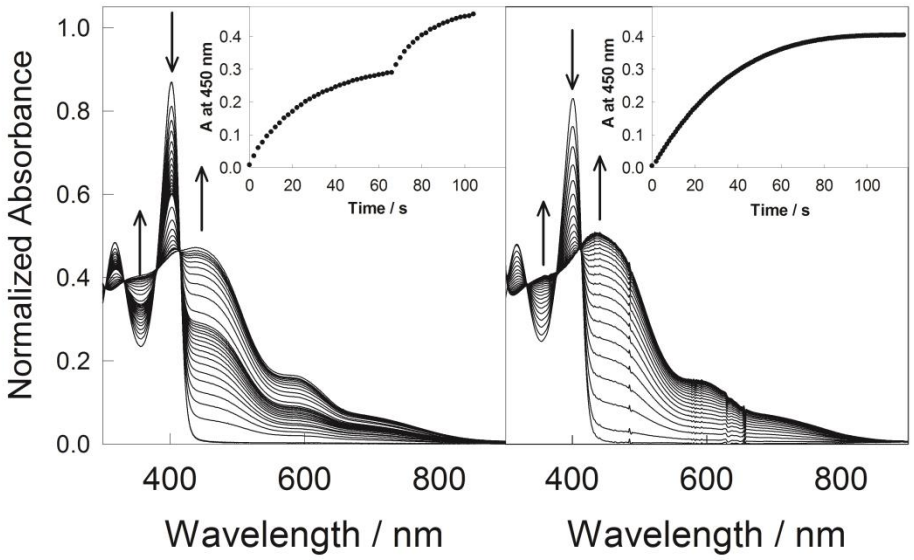

Figure 2-4. Reaction of **4** with two sequential 0.5 equivalent aliquots of *m*CPBA (left) and ten equivalents (right). Conditions: 1×10^{-4} M **4**, acetonitrile with 0.2% H_2O, -40 °C.

The final product of oxidation was examined by EPR spectroscopy (Figure 2-6) and found to be a spin 1/2 system with g = {2.017, 1.978, 1.833}, which is consistent with an iron(V)oxo species and produced in quantitative yield. This experiment showed that the steric bulk of **4** does indeed prevent the formation of a dimer under these conditions. Catalyst **4** was then reacted with excess TBHP (72 equivalents) under the same conditions. The spectral changes that occurred upon oxidation were essentially the same as those that resulted from the reaction with *m*CPBA (Figure 2-5). This shows that the oxidation from iron(III) to iron(V)oxo is indeed possible with the weaker oxidants shown in Table 2-1.

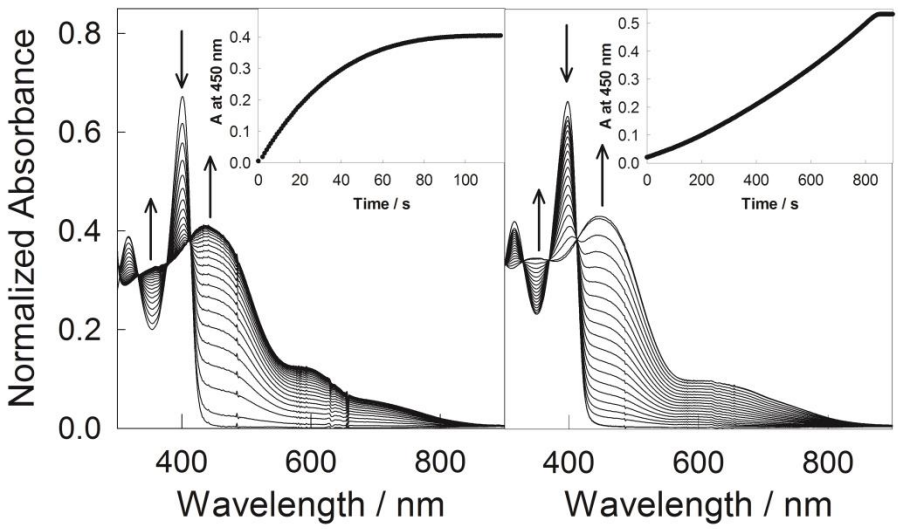

Figure 2-5. Reaction of **4** with excess *m*CPBA (left) and excess TBHP (right). Conditions: 1×10^{-4} M **4**, acetonitrile with 0.2% H_2O, -40 °C.

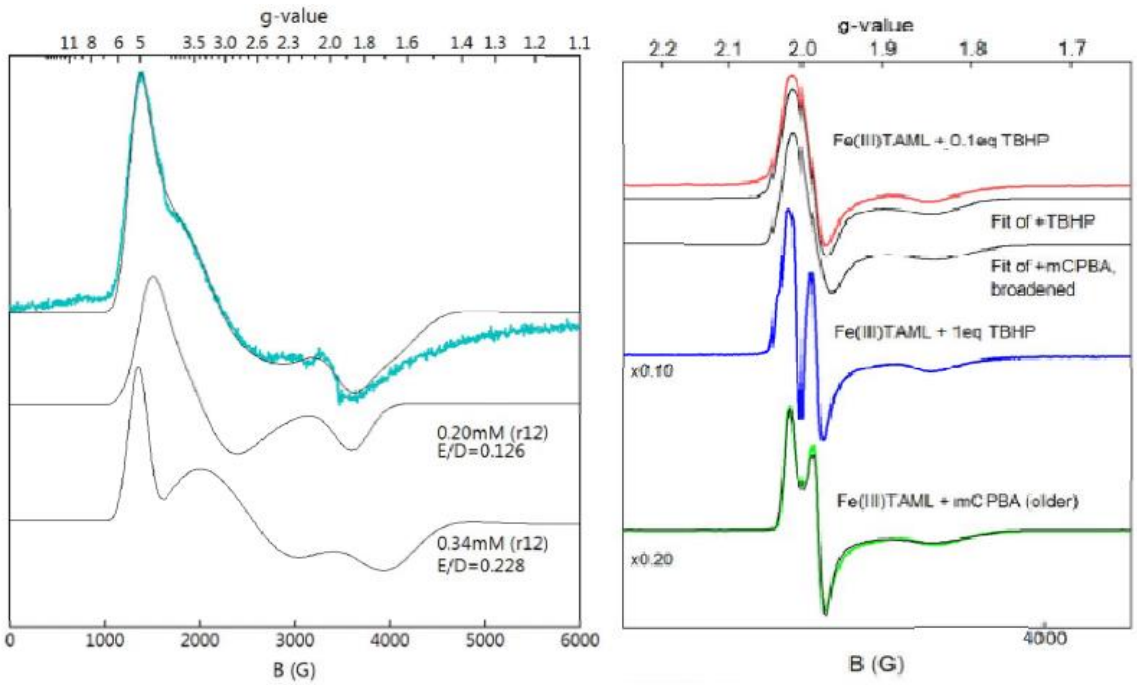

Figure 2-6. EPR spectra of iron(III) **4** (left) and iron(V) **4** (right) in acetonitrile. Conditions: acetonitrile, -40 °C, 5×10^{-4} M **4**, 5×10^{-4} M *m*CPBA (bottom right), 5×10^{-4} M TBHP (middle right).

2.2.4 Resolution of unconventional kinetics with TBHP

As seen in Figure 2-5, the reaction of **4** with TBHP results in a unique concave-up reaction trace, indicating that the rate of the reaction is accelerating. At first glance this would appear to be an autocatalytic reaction, where a product of the reaction acts as a catalyst. However, a close examination of the reaction trace reveals that the reaction finishes abruptly upon complete conversion of **4** to the iron(V)oxo. This atypical reaction trace was also seen in the reaction of TBHP with **1a**, however the final product was the iron(IV) μ-oxo dimer. As seen in Figure 2-7, no other oxidants tested showed this unusual rate acceleration. The curvature of the reaction traces of **1a** and **4** was unusually

parabolic, and the initial rates were lower than the rates measured at any time (*t*) in many cases provided $t > 0$ and, correspondingly, there was no possibility to estimate the steady-state rates for TBHP.[21] The unusual kinetic trace resulting from the reaction of **1a** with TBHP prompted us to study this reaction in more detail.

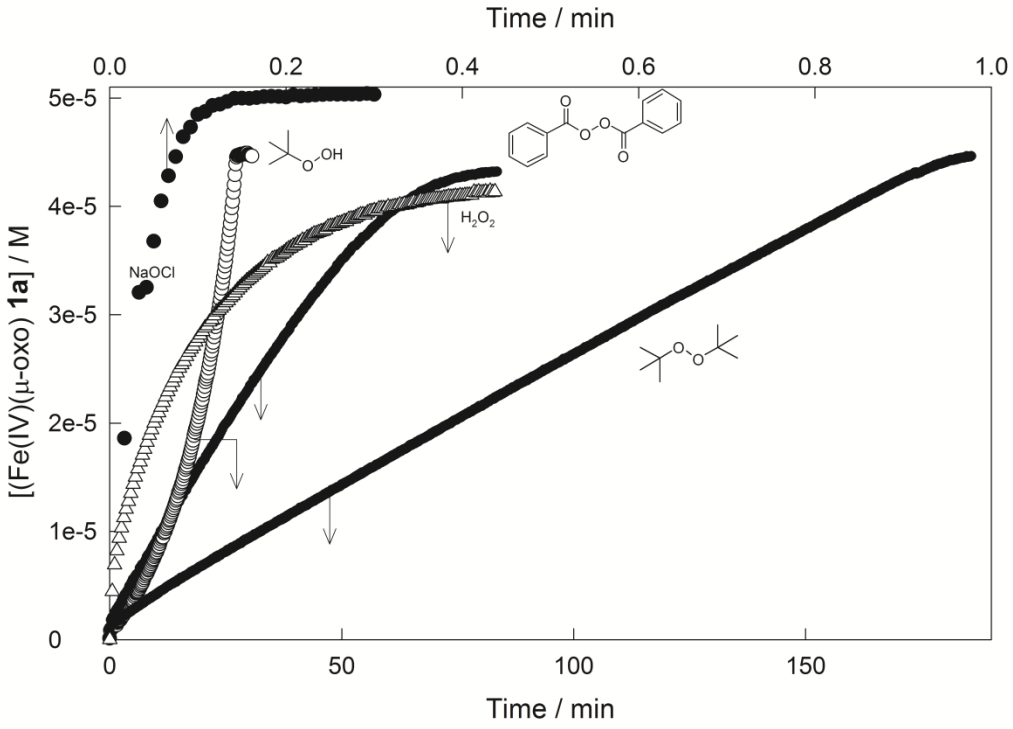

Figure 2-7. Comparison of the rates of oxidation of **1a** to the iron(IV) μ-oxo dimer with the oxidants listed in Table 2-1. The time scale for NaClO is much faster than the other oxidants and is shown as the top X-axis. Conditions: 1×10^{-4} M **1a**, acetonitrile with 0.2% H_2O, -40 °C.

2.2.4.1 NMR analysis to determine stoichiometry of reaction

Initially ^{1}H NMR was used to determine organic fragments produced from TBHP during the oxidation of **1a** into the iron(IV)(μ-oxo) dimer, which occurs in ca. 90% yield (Table 2-1). The spectra of TBHP without **1a** (**1a** is paramagnetic, which causes line

broadening) and with the diamagnetic iron(IV)(μ-oxo) dimer after the completion of the reaction presented in Figure 2-8 show almost quantitative exhaustion of TBHP (δ 1.18) which collapses into *tert*-butanol (δ 1.17 and 2.41) and acetone (δ 2.09) in 41 and 37% yield, respectively (Equation 2–1). Smaller peaks at δ 1.21, 1.36 and 1.79, the integral intensities of which equal 1, 2 and 2, respectively, arise from the three different methyl groups in **2** in the same 1:2:2 ratio.[15] A smaller peak at δ 3.29 shows that methanol is produced, albeit in lower yield than acetone or *tert*-butanol. The spectrum of organic fragments formed, particularly the accumulation of acetone and methanol, is evidence for a free radical character of the reaction between **1a** and TBHP.[22] It should also be mentioned that the sharp lines in the spectrum of products in Figure 2-8 agree with complete conversion of **1a** to iron(IV)(μ-oxo) dimer, which eliminates the paramagnetic species in the reaction medium.

$$\mathbf{1} + (H_3C)_3COOH \rightarrow \underset{100\%}{\mathbf{2}} + \underset{41\%}{(H_3C)_3COH} + \underset{37\%}{(H_3C)_2CO} + \underset{13\%}{H_3COH} \qquad (2\text{–}1)$$

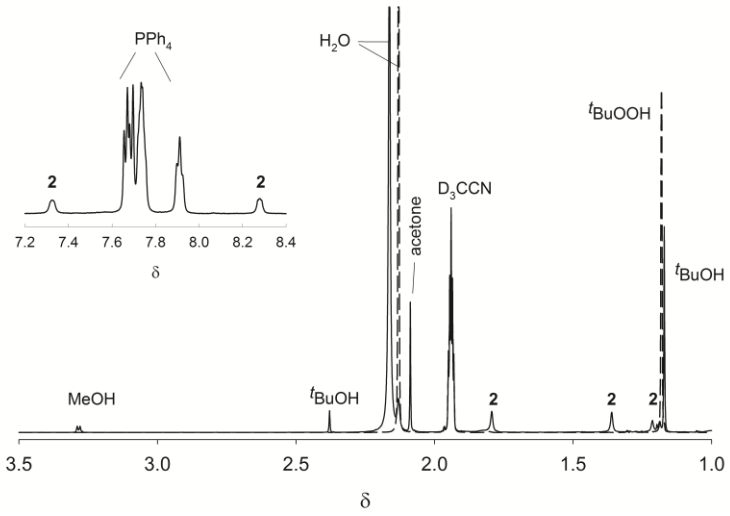

Figure 2-8. The ^{1}H NMR spectra of TBHP alone (dash line) and after its reaction with **1a** to afford iron(IV)(μ-oxo) and smaller organic fragments (solid line) in D_3CCN with 0.2% D_2O. Conditions: [TBHP] 7.32×10^{-3} M, [**1a**] 2.0×10^{-3} M.

2.2.4.2 Investigation of the effects of light and dioxygen on the rate of reaction

With evidence for a mechanism that may involve free radicals, the effects of oxygen and light intensity were studied. Figure 2-9 shows the effects of either excluding oxygen from the reaction mixture or changing the rate of measurement as indicated by the term time between recordings (TbR). The reaction was noticeably faster when spectra were registered more frequently, i.e. when the TbR of successive spectra was lower (Figure 2-9). The increased rate most likely results from the undispersed light beam in the 190-1100 nm spectral region used by the photodiode array instrument. The processes subject to "the diode array acceleration" are known and have recently been reviewed.[23] These diode array accelerated reactions often occur in the presence of O_2, and their

mechanisms, which involve radicals, are complex though these reactions do not involve species in long-lived excited states.

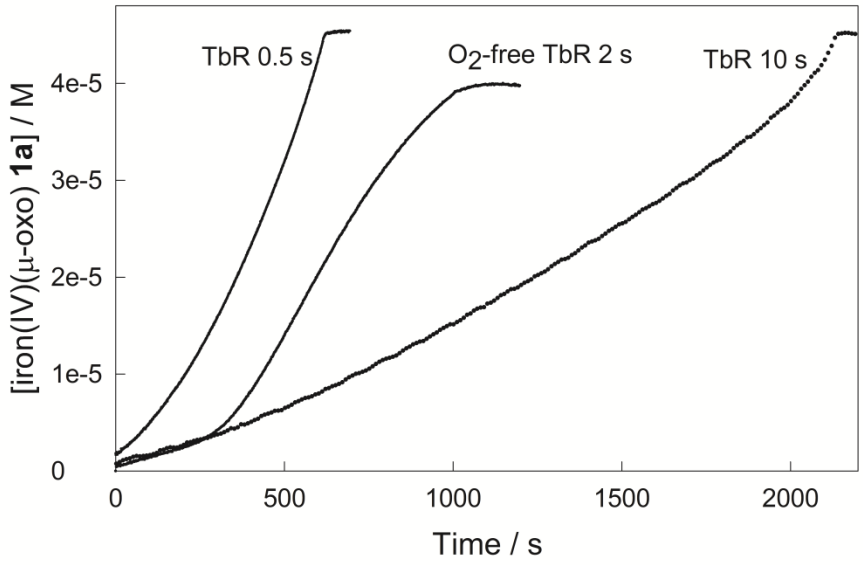

Figure 2-9. Kinetic curves for the formation of iron(IV)(μ-oxo) dimer from **1a** and TBHP under different conditions: in the absence and in the presence of O_2, and applying different time between scans (different TbR, see text for details). Conditions: MeCN with 0.2% H_2O, -40 °C

The reaction kinetics change noticeably in the absence of O_2 (Figure 2-9). The "parabolicity" vanishes, a noticeable lag period followed by the steady-state portion is observed and the reaction rate slows as the reaction nears completion. Thus, O_2 plays a significant role in the reaction, consistent with a free-radical mechanism. The radical nature of the reaction mechanism was further demonstrated by adding 2,2,6,6-tetramethylpiperidine 1-oxyl (tempo), a radical scavenger,[24] to the reaction mixture. No formation of iron(IV)(μ-oxo) dimer was observed in the presence of 1.0×10^{-2} M tempo.

2.2.4.3 Investigation of the effects of TBHP and 1a concentration on the rate of reaction

Attempts were made to compare both initial and maximal rates (when the reactions are practically complete) with the concentrations of the reagents **1a** and TBHP in aerated solutions. Figure 2-10A shows that both the initial and maximal (just before reaction completion) rates are virtually independent of [**1a**] in the range of (0.25–5.0) × 10^{-5} M. This, at least qualitatively, helps to understand the origin of the complex kinetic curves of the formation of iron(IV)(μ-oxo) in the case of TBHP presented in Figure 2-5 and Figure 2-9. In contrast, both the initial and maximal rates depend linearly on [TBHP]. The results in Figure 2-10 suggest that the primary role in determining the overall rate of conversion of **1a** into the iron(IV)(μ-oxo) dimer belongs to TBHP, which is the key reagent during the initiation and propagation steps.

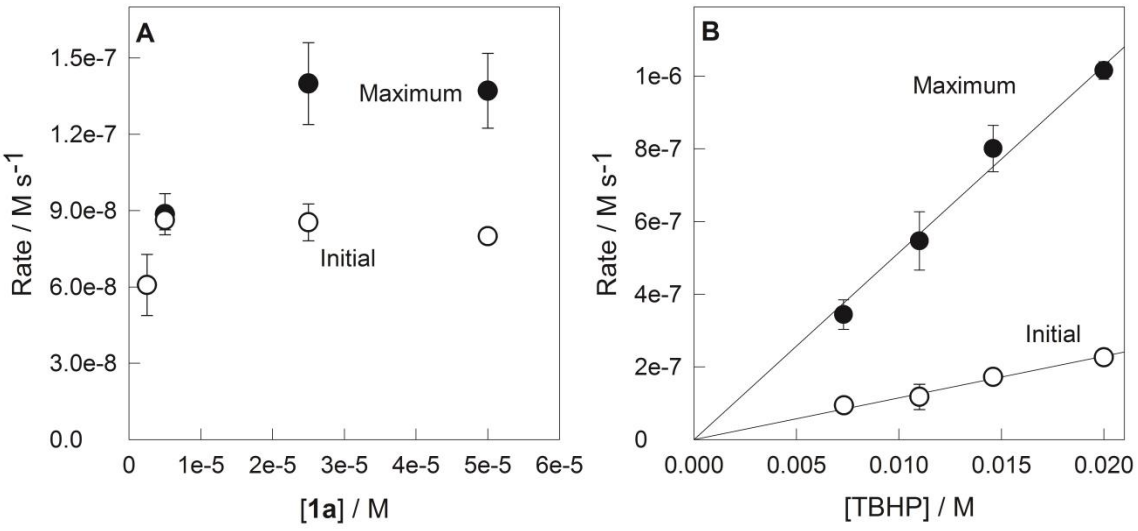

Figure 2-10. Initial and maximal rates of the reaction between **1a** and TBHP as functions of concentrations of **1a** (A) and TBHP (B). Other conditions: MeCN with 0.2% H_2O, –40 °C; A: [TBHP] 5.0 × 10^{-3} M; B: [**1a**] 1.0 × 10^{-4} M

2.2.4.4 Investigation of the effects of proton acceptors and donors on the rate of reaction.

Recently, Nishida, et al, found that proton acceptors accelerate the formation of non-heme iron(IV)oxo complexes from the corresponding iron(III) species and $[Ru(bpy)_3]^{3+}$ in aqueous MeCN.[25] Though TBHP is strikingly different oxidizing agent compared to Ru(III), we thought it might be interesting to test some additives in our system. Bases were of particular interest because they inhibit free-radical oxidations.[26] Therefore, the influence of additives shown in Table 2 on the kinetics of oxidation of **1a** by TBHP was studied.

Table 2-2. Influence of effectors on the oxidation of **1a** by TBHP in wet MeCN at –40 °C.

Effector	Concentration / M	Effect on **1a** +TBHP
1,8-Bis(dimethylamino)naphthalene (proton sponge)	0.010	No reaction
Potassium *tert*-butoxide[a)]	7.3×10^{-3}	No reaction
Sodium bis(trimethylsilyl)amide	2.5×10^{-3}	No reaction
Triethylamine	7.3×10^{-3}	No reaction
1,4-Diazabicyclo[2.2.2]octane (dabco)	$(2.5–250) \times 10^{-4}$	Strong retardation
2,2,6,6-Tetramethylpiperidine (tmpp)	$(1–100) \times 10^{-4}$	Acceleration
tert-Butanol	0.025	No effect
Acetic acid	0.025	No effect

[a)] Solubilized in the presence of 7.3×10^{-3} M 18-crown-6.

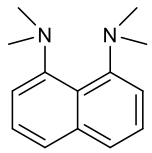

Proton sponge

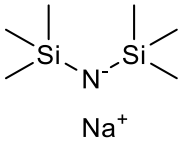

Sodium bis(trimethylsilyl)amide

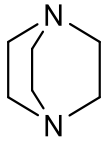

dabco

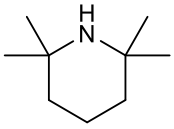

tmpp

Hydrogen donors, viz. *tert*-butanol and acetic acid, did not affect the kinetics of formation of iron(IV)(μ-oxo) dimer at all when used at concentrations in excess of both **1a** and TBHP. The effect of nitrogen bases was diverse. Most of these additives (see Table 2-2) stopped the reaction completely and the formation of iron(IV) μ-oxo dimer was not observed. More sterically congested dabco caused significant rate retardation. Rather unexpectedly, sterically restricted amine tmpp appeared to be a quite remarkable catalyst (Figure 2-11A). Higher loadings of tmpp increase the speed of formation of iron(IV) μ-oxo dimer though the steady-state rate starts to level-off at [tmpp] > 1.0×10^{-2} M. The inset to Figure 2-11A compares the kinetics of formation of iron(IV) μ-oxo dimer in the absence and in the presence of 5×10^{-4} M tmpp. Tmpp increases the initial and the maximal reaction rate by a factor of 40 and 10, respectively. Moreover, the reaction speed became unaffected by light (similar rate at TbR in the range of 0.5–10 s) and remained practically unchanged during the entire conversion of **1a** into iron(IV) μ-oxo dimer implying that the reaction was zero order in **1a**. The zero order hypothesis did not agree with the observation that the slopes of the "zero order" traces appeared to be proportional to the concentration of **1a** (Figure 2-11B). As in the absence of tmpp, the reaction remained a first order process in TBHP (Figure 2-11B).

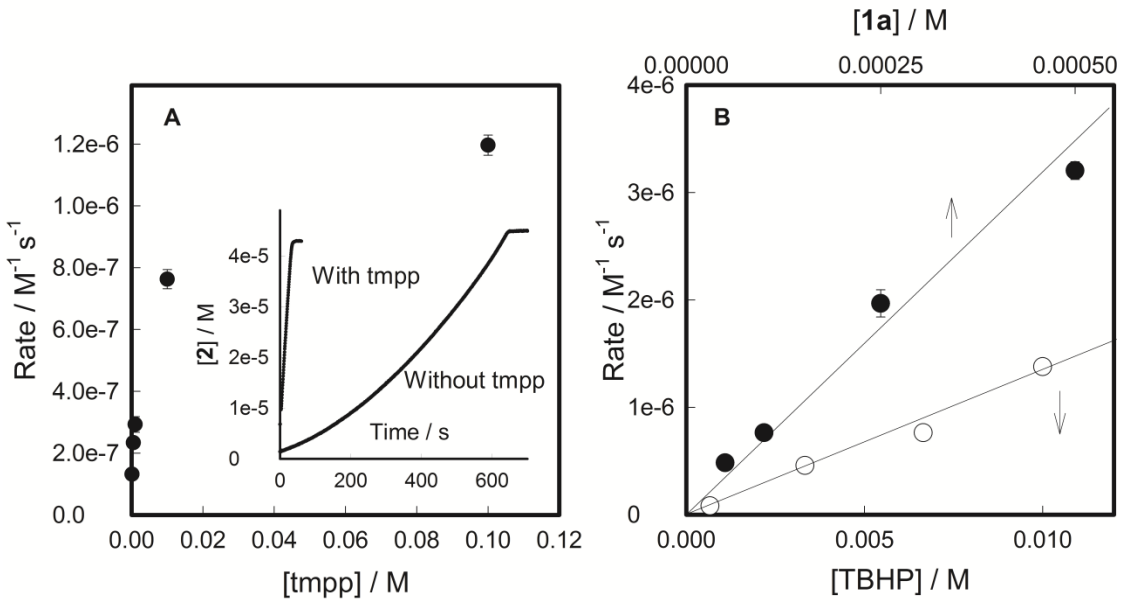

Figure 2-11. Rates of formation of iron(IV)(μ-oxo) dimer as functions of [tmpp] (A), [**1a**] and [TBHP] (B). Inset to A shows kinetic curves for formation of iron(IV)(μ-oxo) dimer with (5.0×10^{-4} M) and without tmpp. Conditions: A: [**1a**] 1.0×10^{-4} M, [TBHP] 7.32×10^{-3} M, (inset: [tmpp] 5×10^{-4} M); B (variable ^{t}BuOOH): [**1a**] 1.0×10^{-4} M, [tmpp] 1.0×10^{-3} M; B (variable **1a**) [TBHP] 6.7×10^{-3} M, [tmpp] 1.0×10^{-2} M; acetonitrile with 0.2% H_2O, –40 °C.

The diverse effect of bases (B) is presumably due to their diverse ability to bind to iron(III) of **1a**. Amines bind to iron(III) of TAML activators even in water causing minor spectral changes in the uv-vis region. Complexes of the FeB and FeB_2 type are produced blocking the axial sites of the iron polyhedron. The stability of the complexes depends of the nature of the amine.[27] We assume that the blocking of the axial sites prohibits the Fe^{III} to Fe^{IV} oxidation. When the amine nitrogen is sterically protected from binding to iron(III) as in the case of tmpp, the mechanism of retardation suggested is turned off and tmpp starts to accelerate the reaction by probably changing the activation

mechanism through the deprotonation of TBHP (Scheme 2-2). Another possibility for the inhibition of the formation of the iron(IV)(μ-oxo) dimer is that the tertiary amines may act as a substrate for the oxidized form of the catalyst forming N-oxides. This reaction has been reported previously.[28]

The concentration of water was also tested as a possible proton donor or acceptor and no difference in rate of formation of iron(IV)(μ-oxo) was observed in the range of 0.1 to 0.5 M [H_2O]. In order to maintain a consistent concentration of water in the reaction media the reactions were initiated by TBHP in anhydrous toluene.[29] As it is known that oxidized TAML species can activate C–H bonds,[3,30] the presence of toluene was tested to determine if it was contributing to the unusual reaction kinetics by acting as a reductant of the oxidized TAML species. However, reactions initiated by TBHP in wet acetonitrile gave the same results. The presence of the tetraphenylphosphonium cation by was also tested by using Na**1a**, and again the reaction rates were the same.

2.2.4.5 Proposed mechanism of oxidation of 1a by TBHP

This combined data allows us to propose two possible pathways for oxidation of **1a** by TBHP, shown in Scheme 2-2. In the absence of base, the reaction occurs as a free-radical, possibly branched, process where light-induced O_2-dependent activation of TBHP may lead to *tert*-butyl hydroperoxyl radical and/or *tert*-butoxyl radical and hydroxyl radical via step 3. The produced *tert*-butyl hydroperoxyl radical reacts in a fast step with iron(III) (step 4) to afford the alkylperoxide complex of iron(IV), which undergoes homolytic scission to afford *tert*-butyl hydroperoxyl radical and iron(V)oxo complex (step 5). The final product iron(IV)(μ-oxo) is produced through comproportionation (step 6). The

intimate details of the postulated initiation step 3 involving homolytic transformation/s of TBHP are not fully understood at a moment. It is likely that the "active" amine (tmpp) eliminates the sensitivity to light by deprotonating TBHP (step 1) and opening the channel for the formation the alkylperoxide complex of Fe(III) (step 2), which collapses to the same product as in step 5 through the heterolysis of the O–O bond. Although amines B other than tmpp may also deprotonate TBHP (step 1), the binding of *tert*-butyl hydroperoxyl anion to iron(III) is precluded due to generation of unreactive FeB and FeB_2 species with the blocked axial sites.

Steps 7 and 8, which are typical of free-radical transformations,[22] account for the formation of organic products, namely *tert*-butanol, acetone and methanol. Minor quantities of methanol are likely produced via the recombination of methyl and hydroxo radicals (the latter are presumably generated through step 3). We are completely aware of the fact that the true mechanism of the reaction studied may contain additional important steps.

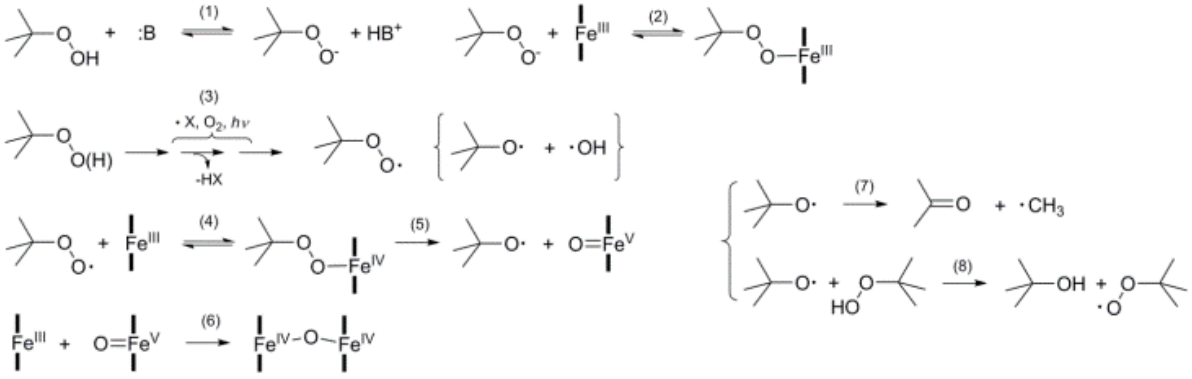

Scheme 2-2. Tentative mechanistic description of the free-radical oxidation of **1a** into iron(IV)(μ-oxo) dimer by TBHP in wet MeCN at –40 °C.

2.3 Conclusion

As opposed to **1a,** TBHP can oxidize **4** to the iron(V)oxo species indicating that peroxides are indeed capable of oxidizing the iron(III) form of all TAML activators to the iron(V)oxo species. The inability to identify the iron(V)oxo species resulting from the reaction of **1a** with organic peroxides and hydrogen peroxide could result from a higher kinetic barrier of the reaction of iron(IV)(μ-oxo) with peroxides. This would result in the rate of oxidation of the iron(IV) μ-oxo dimer with peroxides to the iron(V)oxo being much slower than the spontaneous reduction in the reverse direction. The difference in rates therefore results in no observable iron(V)oxo product..

2.4 Experimental Section

2.4.1 Chemicals

Complex **1a** was prepared from the corresponding sodium salt (GreenOx, Inc) by addition of PPh_4Cl to the aqueous solution as previously described causing the precipitation of **1a**.[15] The resulting product was recrystallized from 50% methanol/water. Anhydrous TBHP in toluene was prepared from 70% aqueous TBHP (Aldrich) as described elsewhere.[29] The additives 2,2,6,6-tetramethylpiperidine (tmpp, ≥ 99%) and 18-crown-6, which was used to solubilize potassium *tert*-butoxide, were purchased from Aldrich. Glacial acetic acid (certified ACS grade) was purchased from Fisher. Potassium *tert*-butoxide was purchased from Strem Chemicals and sublimed in vacuo. 1,8-Bis(dimethylamino)naphthalene was purchased from Sigma and recrystallized three times from ethanol. Sodium bis(trimethylsilyl)amide (98%), 1,4-diazabicyclo[2.2.2]octane (dabco), *tert*-butanol (99.5%), and (2,2,6,6-tetramethylpiperidin-1-yl)oxy (tempo, 98%)

were purchased from Acros. Dabco was purified by sublimation in vacuo. Triethylamine was distilled over calcium hydride. Acetonitrile was dried using a SciMarco solvent dispensing system. Uv-vis spectroscopy was performed using an Agilent 8453 instrument equipped with a liquid nitrogen cooled cryostat set-up from UNISOKU Scientific Instruments, Japan. All reactions were performed at –40 °C. The ^{1}H NMR spectra were registered using Bruker Avance 300 and Bruker Avance III 500 MHz NMR spectrometers.

2.4.2 Kinetic studies

Unless otherwise noted, water and acetonitrile stock solutions of **1a** or **4** and additive, if necessary, were added to a quartz cuvette with a stir bar and diluted with acetonitrile. This solution was allowed to cool to –40 °C for 5 min before oxidant was injected. The final volume of all samples was 2 mL. The formation of iron(IV)(μ-oxo) dimer was monitored by uv-vis spectroscopy at 708 nm for catalyst **1a**, which is the isosbestic point between the dimer and the iron(V)oxo species under the conditions selected. Unless otherwise noted, spectra were recorded every 2 s. The concentration of iron(IV) μ-oxo dimer was calculated using the previously determined extinction coefficient of 6280 M^{-1} cm^{-1} at 708 nm.[3] All reported rates are mean values of at least three measurements. Kinetic data in the absence of O_2 were obtained by preparing stock solutions of reagents in acetonitrile which had been subjected to three freeze-pump-thaw cycles. The reaction mixtures were prepared by adding appropriate volumes of deoxygenated stock solutions into a quartz cuvette fitted with a screw-top cap and replaceable septum which had been

purged with argon. The solution was diluted to the required volume with deoxygenated acetonitrile and the reaction conducted as described previously.

2.4.3 ^{1}H NMR studies

Due to the fact that **1a** is paramagnetic, ^{1}H NMR experiments were performed by adding **1a** to initiate the reaction. The reaction mixture was prepared by dissolving TBHP in deuterated acetonitrile to achieve the desired concentration. This sample was analyzed by ^{1}H NMR and the shimming file was saved for analysis of the next sample. This solution was then poured into a quartz cuvette and inserted into the low-temperature apparatus and allowed to cool to –40 °C. The reaction was initiated by addition of **1a** in deuterated acetonitrile and monitored as described in section 2.4.2. Upon completion of that reaction (as determined by leveling off of the uv-vis trace at 708 nm), approximately 1 mL of the reaction mixture was pipetted into a chilled NMR tube, immediately placed in liquid nitrogen and frozen. This sample was kept in liquid nitrogen until analysis by ^{1}H NMR. Then it was removed from the liquid nitrogen and allowed to warm just enough for the frozen condensation on the tube to melt and be wiped off. It was then analyzed by NMR without locking or shimming using the shim file from the previously prepared sample. Data were analyzed using a Bruker TopSpin 3.0 software.

2.5 References

1. Collins, T. J. *Acc. Chem. Res.* **1994**, *27*, 279–285.

2. Crabtree, R. H. *Chem. Rev.* **2015**, *115*, 127–150.

3. Kundu, S.; Van Kirk Thompson, J.; Ryabov, A. D.; Collins, T. J. *J. Am. Chem. Soc.* **2011**, *133*, 18546–18549.

4. Do Pham, D. D.; Kelso, G. F.; Yang, Y.; Hearn, M. T. W. *Green Chem.* **2014**, *16*, 1399.

5. Do Pham, D. D.; Kelso, G. F.; Yang, Y.; Hearn, M. T. W. *Green Chem.* **2012**, *14*, 1189–1195.

6. Liu, Z. D.; Wang, G.; Li, R.; Liu, Y. R.; Liu, H. Y.; Sun, Z. M.; Wang, X. N.; Wu, Z. *Appl. Mech. Mater.* **2014**, *685*, 133–136.

7. Napoly, F.; Kieffer, R.; Jean-Gérard, L.; Goux-Henry, C.; Draye, M.; Andrioletti, B. *Tetrahedron Lett.* **2015**, *56*, 2517–2520.

8. Li, R.; Wang, G.; Liu, Y.; Chen, X.; Sun, Z.; Liu, H.; Wang, X.; Wu, Z.; Liu, Z. *Appl. Mech. Mater.* **2014**, *723*, 601–604.

9. Kwon, E.; Cho, K.-B.; Hong, S.; Nam, W. *Chem. Commun.* **2014**, *50*, 5572–5575.

10. Panda, C.; Debgupta, J.; Díaz, D. D.; Singh, K. K.; Gupta, S. Sen; Dhar, B. B.; Díaz Díaz, D.; Singh, K. K.; Sen Gupta, S.; Dhar, B. B. *J. Am. Chem. Soc.* **2014**, *136*, 12273–12282.

11. George, P. *Biochem. J.* **1953**, *54*, 267–276.

12. Chanda, A.; Shan, X.; Chakrabarti, M.; Ellis, W. C.; Popescu, D. L.; De Oliveira, F. T.; Wang, D.; Que, L.; Collins, T. J.; Münck, E.; Bominaar, E. L. *Inorg. Chem.* **2008**, *47*, 3669–3678.

13. Popescu, D. L.; Vrabel, M.; Brausam, A.; Madsen, P.; Lente, G.; Fábián, I.; Ryabov, A. D.; Van Eldik, R.; Collins, T. J. *Inorg. Chem.* **2010**, *49*, 11439–11448.

14. Collins, T. J. *Science* **2001**, *291*, 48–49.

15. Ghosh, A.; de Oliveira, F. T.; Yano, T.; Nishioka, T.; Beach, E. S.; Kinoshita, I.; Münck, E.; Ryabov, A. D.; Horwitz, C. P.; Collins, T. J. *J. Am. Chem. Soc.* **2005**, *127*, 2505–2513.

16. Collins, T. J. *Acc. Chem. Res.* **2002**, *35*, 782–790.

17. de Oliveira, F. T.; Chanda, a; Banerjee, D.; Shan, X. P.; Mondal, S.; Que, L.; Bominaar, E. L.; Munck, E.; Collins, T. J. *Science* **2007**, *315*, 835–838.

18. Kundu, S.; Thompson, J. V. K.; Shen, L. Q.; Mills, M. R.; Bominaar, E. L.; Ryabov, A. D.; Collins, T. J. *Chem.–Eur. J.* **2015**, *21* (4, 1803–1810.

19. Ren, Q.; Guo, Y.; Mills, M. R.; Ryabov, A. D.; Collins, T. J. *Eur. J. Inorg. Chem.* **2015**, *201*, 1445–1452.

20. Ghosh, M.; Singh, K. K.; Panda, C.; Weitz, A.; Hendrich, M. P.; Collins, T. J.; Dhar, B. B.; Gupta, S. Sen. *J. Am. Chem. Soc.* **2014**, *136*, 9524–9527.

21. Espenson, James, H. *Chemical Kinetics and Reaction Mechanisms*; McGraw-Hill, Inc.: New York, 1995.

22. Kochi, K. *J. Am. Chem. Soc.* **1962**, *84*, 1193–1197.

23. Lente, G.; Fábáin, I. *Pure Appl. Chem.* **2010**, *82*, 1957–1973.

24. Bowry, V. W.; Ingold, K. U. *J. Am. Chem. Soc.* **1992**, *114*, 4992–4996.

25. Nishida, Y.; Morimoto, Y.; Lee, Y. M.; Nam, W.; Fukuzumi, S. *Inorg. Chem.* **2013**, *52*, 3094–3101.

26. Berezin, I. V; Denisov, E. T.; Emanuel, N. M. *The Oxidation of Cyclohexane*; Pergamon: Oxford, 1966.

27. Polshin, V.; Popescu, D. L.; Fischer, A.; Chanda, A.; Horner, D. C.; Beach, E. S.; Henry, J.; Qian, Y. L.; Horwitz, C. P.; Lente, G.; Fabian, I.; Münck, E.; Bominaar, E. L.; Ryabov, A. D.; Collins, T. J. *J. Am. Chem. Soc.* **2008**, *130*, 4497–4506.

28. Sullivan, S. Z.; Ghosh, A.; Biris, A. S.; Pulla, S.; Brezden, A. M.; Collom, S. L.; Woods, R. M.; Munshi, P.; Schnackenberg, L.; Pierce, B. S.; Kannarpady, G. K. *Chem. Phys. Lett.* **2010**, *498*, 359–365.

29. Hill, G.; Rossiter, B. E.; Sharpless, B. *J. Org. Chem.* **1983**, *48*, 3607–3608.

30. Kundu, S.; Thompson, J. V. an K.; Shen, L. Q.; Mills, M. R.; Bominaar, E. L.; Ryabov, A. D.; Collins, T. J. *Chem.–Eur. J.* **2015**, *21*, 1803–1810.

Chapter 3

Chemical and Electrochemical Generation and Characterization of Iron(IV) and Iron(V) TAML Complexes in Pure Water

3.1 Introduction

Biomimetic and bioinspired inorganic complexes are of interest to chemists for the primary reason that metalloenzymes can perform incredible and unparalleled chemical transformations under generally mild conditions. Cytochrome P450 and methane monooxygenase enzymes are prime examples, because they perform two of the most sought-after transformations in one catalytic cycle, the activation of dioxygen and the oxidation of carbon-hydrogen bonds.[1,2] Inorganic chemists model enzymes for two fundamental reasons. The first is to perform chemical transformations similar to those performed by enzymes but without the cost inhibitions of isolating them. The second reason is that preparing synthetic models of enzymes can aid in understanding the enzyme's catalytic mechanism.

Cytochrome P450 provides an example for the interest in determining the nature of the high-valent catalytic intermediates of enzyme active sites. In Nature, the highest oxidation states of peroxidases and cytochrome P450 enzymes are the Compound I states, which are two oxidation equivalents above the iron(III) resting state. These species are formally iron(IV) oxo units with radical cation porphyrin ligands. These compounds are capable of abstracting hydrogen from bound substrates with quite high observed rate constants. Human P450 21A2 hydroxylates progesterone with a V_{max}/K_M value of 1.3×10^7 s^{-1},[3] 1B1 hydroxylates estradiol with a V_{max}/K_M value of 1.8×10^3 s^{-1},[4] 1A1 hydroxylates 17α-ethinylestradiol with a V_{max}/K_M of 2.1×10^3 s^{-1}.[5] The question that puzzled chemists was how the abstraction of a hydrogen atom from a C–H bond, requiring a reduction potential of 1.5 V, could take place within a protein scaffold with relatively easy to oxidize tyrosine and tryptophan residues.[6]

Green's work with cytochrome P450 has shown that thiolate ligation increases the pK_a of the one-electron reduced Compound II intermediate by 8.5 units relative to the histidine-ligated porphyrins found in peroxidase enzymes.[6] This shift in pK_a favors an iron(IV)hydroxo compound for the one-electron-reduced Compound II species of cytochrome P450 enzymes rather than an iron(IV)oxo complex. This in turn, favors productive substrate oxidation over the oxidation of tyrosine residues from the protein scaffold by 10,000 fold.[6] No synthetic iron(IV)hydroxide complexes have yet been reported in the literature, exemplifying the unique ability of cytochrome P450 to control the local environment of the active site to favor productive catalysis.

For a long time, inorganic model compounds that were isoelectronic with Compound I states were unknown for mimetics of the active sites of these enzymes. The first thoroughly characterized example of an iron(V)oxo unit formed from an iron(III) precursor was reported in 2007 by the oxidation of Generation 1 TAML activator **1a** (Figure 3-1).[7] This compound was prepared from **1a** and *m*CPBA at low temperatures in organic nitriles. The following representatives of the iron(V)oxo core were all made in non-aqueous solvents.[8–12] Due to the instability of these complexes, preparing them in pure water as a solvent remained a huge challenge.[13] Using TAMLs **2** of Generation 3, Panda, et al., reported the formation of their iron(V)oxo derivatives in a 50% water-acetonitrile mixture[14] and the water content was then increased to 90%.[15] Water markedly decreases the stability of the iron(V)oxo species. At 90% water the iron(V)oxo species degrade 10 times faster than in pure acetonitrile.[15]

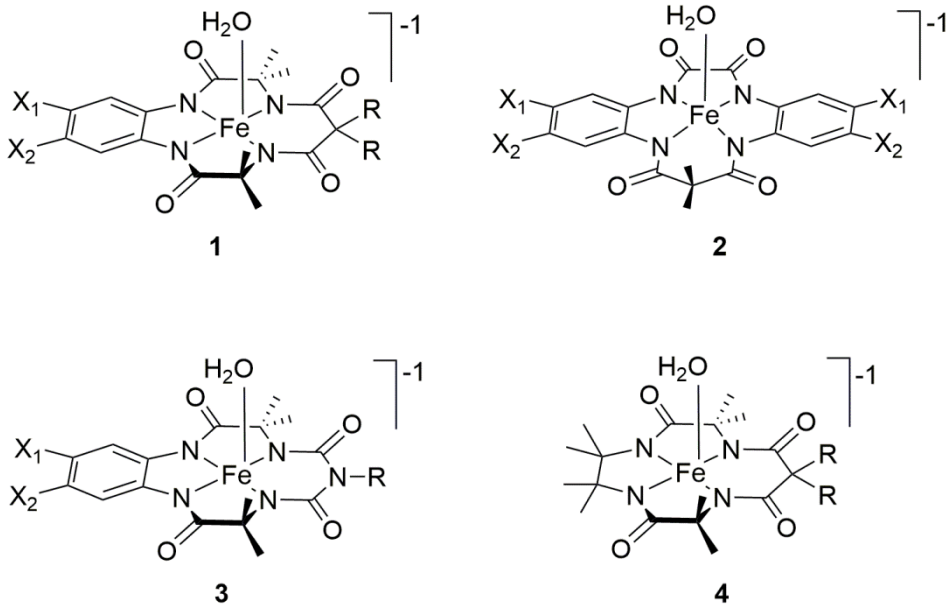

Figure 3-1. TAML Activator generations **1**, **2**, **3** and **4**

Here we show that several high-valent iron species, including the iron(V)oxo and a proposed iron(IV)hydroxo species of a TAML activator are affordable in pure water without any organic co-solvent, and can both be generated chemically or electrochemically. This became possible using the recently introduced TAML activator **4**,[16] which in contrast to TAMLs **1**, **2**, and **3,** does not have aromatic ring at the head part of the molecule (a 'beheaded' TAML). The iron(V)oxo unit is rapidly and quantitatively produced by reacting **4** with NaClO at pH 2 and 10.6 at 13 °C. Under basic conditions (pH 13) this species is not formed and the iron(IV)oxo unit is generated instead. Remarkably, the iron(V)oxo species is converted to iron(IV)oxo by increasing pH from 2 to 13, whereas decreasing pH from 13 to 2 induces disproportionation of iron(IV)oxo to form iron(V)oxo and iron(III) species (Scheme 1-1).

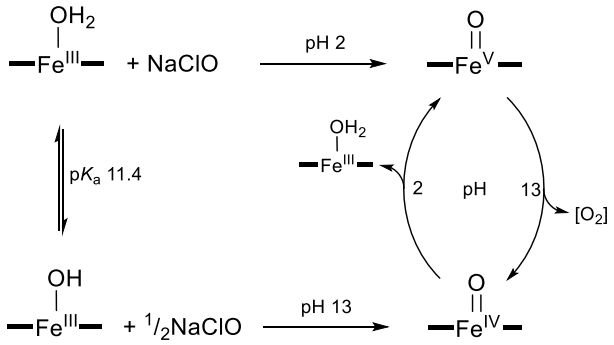

Scheme 3-1. pH-Dependent transformations of **4** in aqueous solutions in the presence and in the absence of NaClO at 13 °C.

3.2 Results and Discussion

3.2.1 Investigation of Dimerization of 4 in Acetonitrile

The oxidation of **4** with both *m*CPBA and TBHP in acetonitrile at –40 °C was discussed in detail in Chapter 2, Section 2.2.3. Unlike **1a**, which dimerizes readily at –40 °C in MeCN, **4** reacts with either *m*CPBA or TBHP to yield the iron(V)oxo species in high yield. This was considered an advantage in studying the oxidized states of **4** in water, as **1a** is known to dimerize at pH<10.5 and form the iron(IV)oxo at pH>12.[17] This is especially true with electrochemical generation of high-valent species of **4** in aqueous solution, as TAML activators had previously given voltammograms with the two examples being a cyclic voltammogram of surface bound **1a** in 0.1 M HNO_3,[18] and a differential pulse voltammogram of the same catalyst at pH 12.6.[19]

3.2.2 Oxidation of 4 with NaClO in water

The advantages of using NaClO over *m*CPBA as an oxidant for aqueous studies include higher reactivity and unlimited solubility in water. Figure 1-1 shows the spectra of **4** and the products formed in the presence of NaClO at pH 10.6 and 13. At pH 10.6, the reaction is completed within 2 min when 1 equivalent of NaClO is added. The oxidation is beneficially clean. There are just two absorbing species in solution supported by five isosbestic points at 265, 293, 312, 347 and 384 nm. The inset to Figure 3-2A confirms the 1:1 reaction stoichiometry implying that the product should be two oxidation equivalents above the iron(III) resting state. It is worth noting that similar results were obtained at all pH up to 10.5.

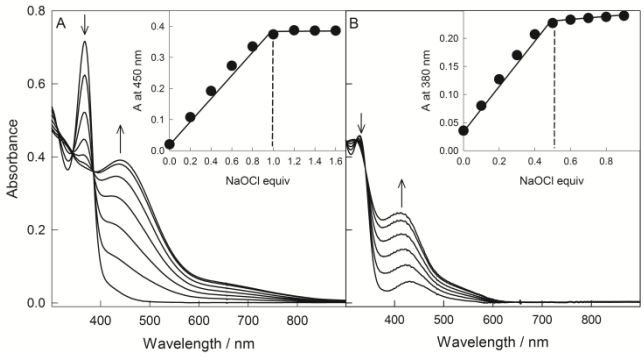

Figure 3-2. Titration of **4** with NaClO at pH 10.6 (A) and 13 (B). Each spectrum represents the spectral change resulting from the addition of an aliquot of NaClO. The insets show the absorbance at the λ_{max} (450 nm) of the new species. Conditions: 1×10^{-4} M **4**, 0.01 M phosphate buffer, 13 °C.

EPR and ^{57}Fe Mössbauer spectroscopy confirm the quantitative conversion of iron(III) to iron(V) upon reaction with NaClO. As seen in Figure 3-3, the broad signal of **4** ($S = {}^{3}/_{2}$) at pH 2 disappears entirely on addition of 1 equivalent of NaClO with

concomitant generation of the new much sharper S ½ resonance. Note that the identical matching signal was registered in MeCN where iron(III) TAMLs are converted into iron(V)oxo species at –40 °C.

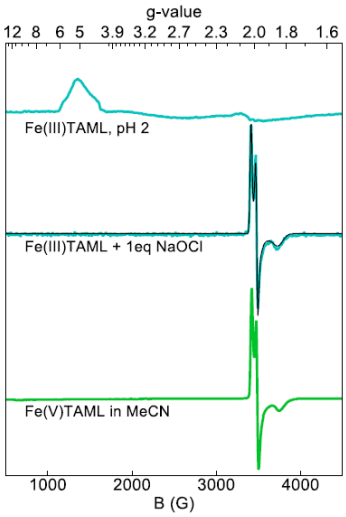

Figure 3-3. EPR spectra of **4** (5×10^{-4} M) registered at pH 2 in the absence and in the presence of 1 and 0.5 eq NaClO, respectively, and the spectrum of **4** in MeCN recorded in the presence of 1 eq *m*CPBA.

The spectrum of the product generated similarly at pH 13 is presented in Figure 3-2B. This oxidation is very clean as well, with isosbestic points at 302, 324, and 341 nm. The inset to Figure 3-2B reveals, however, a 2:1 iron to hypochlorite stoichiometry pointing to an iron(IV) product. Thus, the oxidation state of iron in the product of oxidation of **4** by NaClO in pure water is rather unexpectedly dictated by pH (Scheme 3-1).

EPR studies at pH 13 agree with the formation of iron(IV) product also because the broad signal from **4** disappeared on addition of 0.5 equivalents NaClO (Figure 3-2B).

No new signal was registered consistent with the formation of EPR silent (S 1) iron(IV) species.[20]

Mössbauer spectra were also recorded for the iron(III), iron(IV) samples at high and low pH (vide infra), and iron(V) samples (Figure 3-4). The iron(III) samples at high and low pH displayed similar isomer shifts (δ), of 0.14 mm s^{-1} at pH 2 and 0.11 mm s^{-1} at pH 13. The quadrupole splitting ($|\Delta E_Q|$) for these two species, however, showed more significant differences, with values of 3.59 mm s^{-1} at pH 2 and 2.94 mm s^{-1} at pH 13. The iron(V) species displayed a doublet with an isomer shift of -0.50 mm s^{-1} and quadrupole splitting ($|\Delta E_Q|$) of 4.68 mm s^{-1}. This compares closely with the values for iron(V) derivative of 1a, which were δ = -0.46 and $|\Delta E_Q|$ = 4.25 mm s^{-1}. The values for the isomer shift and quadrupole splitting of iron(IV)oxo **4**, of δ = -0.18 mm s^{-1} and $|\Delta E_Q|$ = 4.06 mm s^{-1}, also correlate with those of iron(IV)oxo **1a**, with values of δ = -0.19 mm s^{-1} and $|\Delta E_Q|$ = 3.95 mm s^{-1}. The high-spin iron(IV) complex generated at low pH has an δ value of -0.12 mm s^{-1}, similar to that for the iron(IV)oxo species, however the quadrupole splitting is much smaller, with $|\Delta E_Q|$ = 0.82 mm s^{-1}.

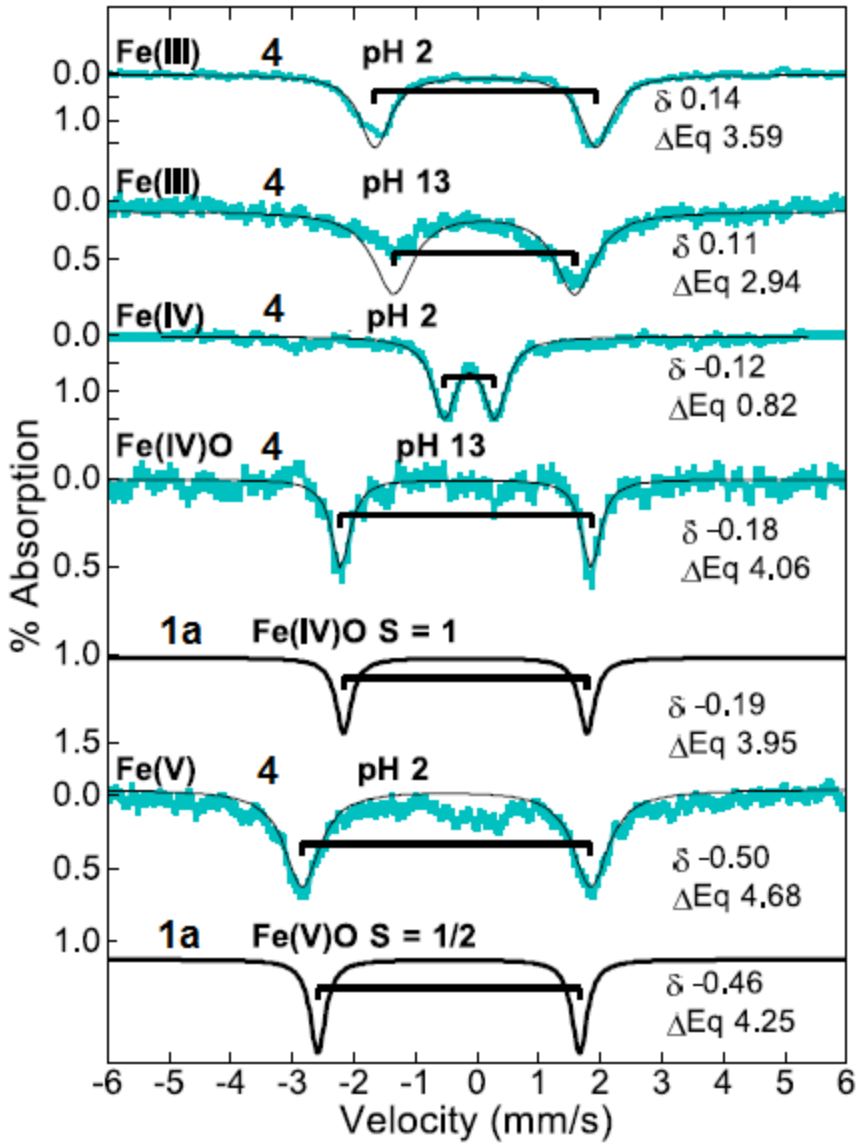

Figure 3-4. Mössbauer spectra for **4** in the III, IV, and V oxidation states. Conditions: 1×10^{-3} M **4.** Spectra for **4** recorded at 4.2 K in water with 10 % glycerol. Data for **1a** simulated using the parameters found in reference 17 for iron(IV)oxo **1a** and reference 7 for iron(V)oxo **1a**.

3.2.3 Electrochemical Studies of 4

The conversion of **4** by NaClO into iron(V)oxo species occurs without the intermediacy of iron(IV) which can be seen in Figure 3-2A. Such behavior of a TAML activator is unique. The oxidations of **1** by NaClO and *m*CPBA in MeCN at –40 °C and below occur with spectrally detectable diiron(IV)(μ-oxo) species[21] because the $Fe^{III} \rightarrow Fe^{IV}$ process is much faster than the $Fe^{IV} \rightarrow Fe^{V}$ conversion.[22,23] It is very likely that the diiron(IV)(μ-oxo) dimer is not formed from **4** for steric reasons created by the four adjacent methyl groups but this does not rule out other iron(IV) derivatives of **4**. In fact, there is plenty of evidence that iron(IV) can be produced from **4**. The first piece of evidence was obtained by cyclic voltammetry. Although all TAMLs of previous generations provided non-informatively broad and poorly reproducible cyclic voltammograms (CVs) in water, TAML **4** revealed quite the opposite case in the form of the textbook Nerstian one-electron CV at pH 2 (Figure 3-5). The peak separation of 58 mV, identical anodic and cathodic currents ($i_a = i_c$) and the linearity of i_a or i_c against square root of the scan rate ($v^{½}$) are observed at v in the range of 10–150 mV s^{-1}.

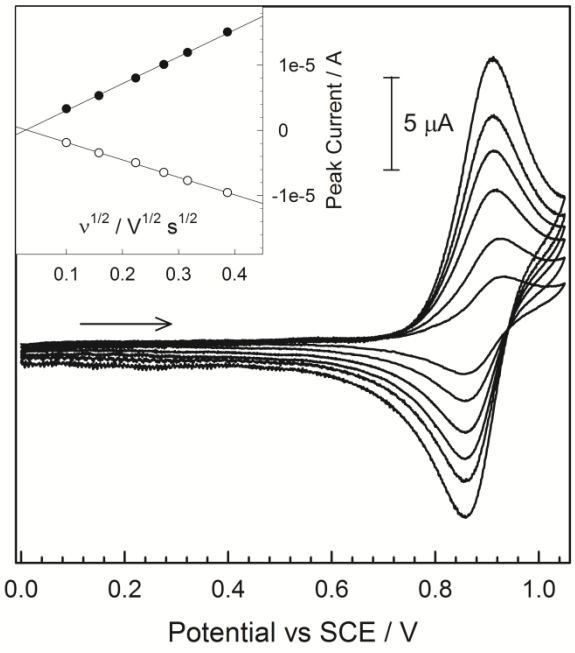

Figure 3-5. Cyclic voltammograms of **4** at different scan rates at pH 2. Scan rates from smallest to largest are 10, 25, 50, 75, 100 and 150 mV s^{-1}. The inset shows the dependence of the anodic peak current on the square root of the scan rate. Conditions: 2 mM **4**, 0.1 M $NaClO_4$ adjusted to pH 2 with $HClO_4$, 25°C.

Spectroelectrochemical study has shown that the uv-vis spectrum generated by applying a constant potential of 1.2 V versus SCE (Figure 3-8) does not match that generated from **4** by NaClO (Figure 3-2). The "electrochemical" spectrum can be produced by one electron oxidation of **4** by Ce(IV). Therefore, the above mentioned spectrum should correspond to the iron(IV) species which most likely does not contain the oxo ligand.[12] These facts combined strongly point to the concerted mechanism of formation of the iron(V)oxo unit from **4** and NaClO. A less probable option would be that the iron(IV) intermediate produced is oxidized much faster than iron(III), which makes iron(IV) spectrally undetectable.

3.2.4 Examination of the electrochemical properties of 4 with changing pH

The pH-dependent formation of either iron(IV)oxo or iron(V)oxo derivatives of **4** upon reaction with NaClO led us to study the electrochemistry of this compound in the pH range 2-13. The general equation for a pH-dependent redox couple is given in Equation 3–1.

$$\mathrm{Ox} + n\mathrm{e}^- + m\mathrm{H}^+ \rightleftharpoons \mathrm{Red}(\mathrm{H}^+)_m \qquad (3-1)$$

The measured reduction potential ($E_{1/2}$) is predicted by the Nernst equation to have a pH dependence according to Equation 3–2 Where D_O and D_R are the diffusion coefficients for the oxidized and reduced species.[24]

$$E_{1/2} = E^{o\prime} - [\frac{0.059}{n}]\log(\frac{D_O}{D_R})^{\frac{1}{2}} - 0.059\left(\frac{m}{n}\right)\mathrm{pH} \qquad (3-2)$$

This analysis can be used to generate Pourbaix diagrams that reveal which species are stable under a given set of conditions. Cyclic voltammograms of **4** taken every 0.5 pH units reveal a complicated electrochemical oxidation scheme. The cyclic voltammograms obtained in the range from pH 10.6 to 13 are shown in Figure 3-6A. The quasi-reversible wave at pH 10.6 splits into two smaller quasi-reversible waves as the pH is raised to 13. The wave at 0.51 V (versus SCE) remains in place as another peak drifts toward more negative potential. This drift occurs with a slope of 50 mV/pH, which is close to the Nernstian 59 mV/pH slope indicating a $1e^-/1H^+$ coupled electron transfer (Figure 3-7). In this region, the iron(III)hydroxo species undergoes proton-coupled electron transfer to give the iron(IV)oxo, followed by further one-electron oxidation to yield the iron(V)oxo species. In the pH ranges 2-7.5, and 7.5-10.5 (Figure 3-6 B and C), the interpretation of the waves is somewhat less straightforward. From pH 2 to 4.5, the reversible wave

remains at 0.91 V. However the current increases by approximately two-fold. Also in this region the anodic peak begins to drift on changing the pH from 4.5 to 7.5, but with a slope of 29 mV/pH. The cathodic peak at 0.88 V corresponding to the reversible wave at pH 2 shrinks, and a new peak at 0.51 begins to appear. This cathodic peak matches exactly the peak from the quasi-reversible wave at pH 10.5 shown in figure 3-6A. From pH 7.5 to 10.5 the anodic peak at 0.86 V moves to more negative potential, with decreasing current. At the same time a new anodic peak appears with increasing current as it moves to more negative potential. The potential of the cathodic peak shows no significant change in this pH range, however there is a slight increase in the current. If the potentials of the quasi-reversible waves at pH 4 and 10.5 are compared, the slope is 62 mV/pH, very close to the value for a $1H^+/1e^-$ (or $2H^+/2e^-$) transfer. Based on this data, we propose that the pseudo-reversible peak at pH 10.5 represents the oxidation of iron(III)aqua species to iron(V)oxo. It is unclear from this data whether this occurs through two sequential $1H^+/1e^-$ steps or some other mechanism. Especially difficult to rationalize is the existence of an iron(IV) species from pH 4 to 10.5, as both the iron(IV)oxo complex and the iron(IV) species generated at pH 2 are unstable in this range as shown by other experiments conducted and discussed below.

Alternatively, the somewhat confusing trends between pH 4 and 10.5 may result from the Pourbaix diagram being prepared by plotting the anodic peak potential versus pH, due to the lack of classical reversible waves at every pH. While not ideal, Bordwell has shown that plotting only the anodic peaks versus pH is comparable to plotting the reversible potentials in the generation of Pourbaix diagrams for the elucidation of proton-

coupled electron transfer mechanisms.[25] However, for this system, it may not be sufficient to completely characterize what is happening in solution.

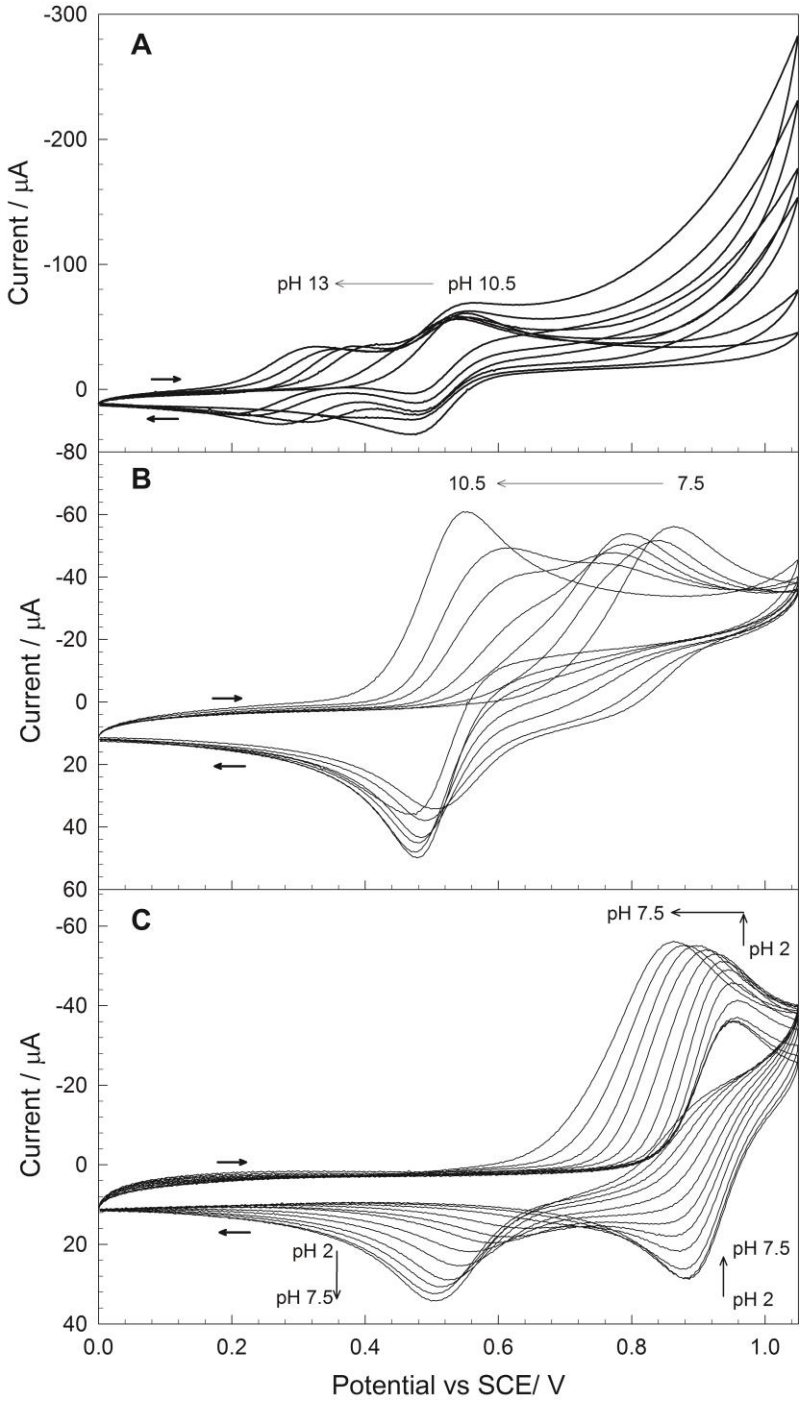

Figure 3-6. Cyclic voltammograms of **4** at three different pH ranges. From 10.5 to 13 (A), 7.5 to 10.5 (B), and 7.5 to 2 (C). Voltammograms are taken every 0.5 pH units. Conditions: 5 mM **4**, 1 M $NaClO_4$, 100 mV/s scan rate.

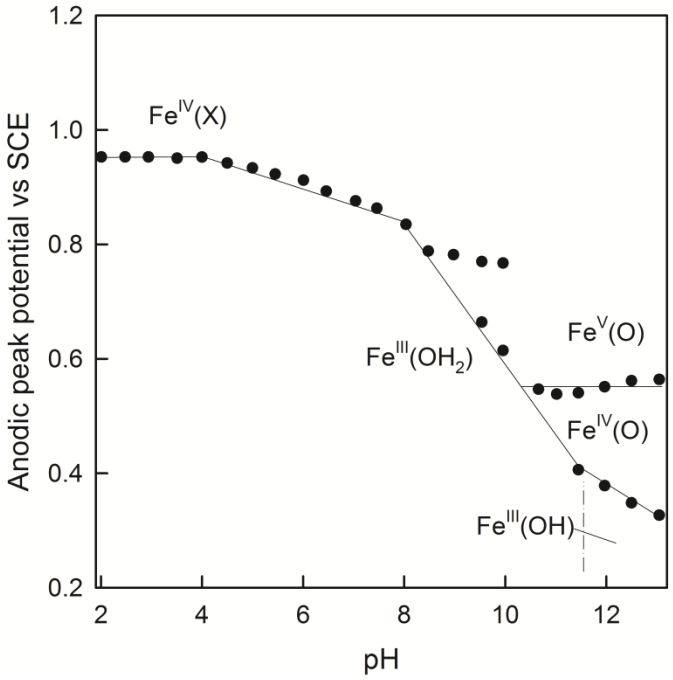

Figure 3-7. Pourbaix diagram of 4. The diagram was prepared by plotting the anodic peaks of the voltammograms in Figure 4 versus pH. See Figure 4 caption for conditions.

3.2.5 Spectroelectrochemical studies of 4

Spectroelectrochemical studies of **4** were conducted at pH 2 and 13. At pH 2, a green species which is presumably an iron(IV) complex is generated readily at 1.2 V (Figure 3-8A). At 1.5 V, a brown species is generated that has a uv-vis spectrum that matches that of iron(V)oxo generated with NaClO (Figure 3-8B). The iron(V)oxo is generated at 72 % yield after 50 minutes under these conditions.

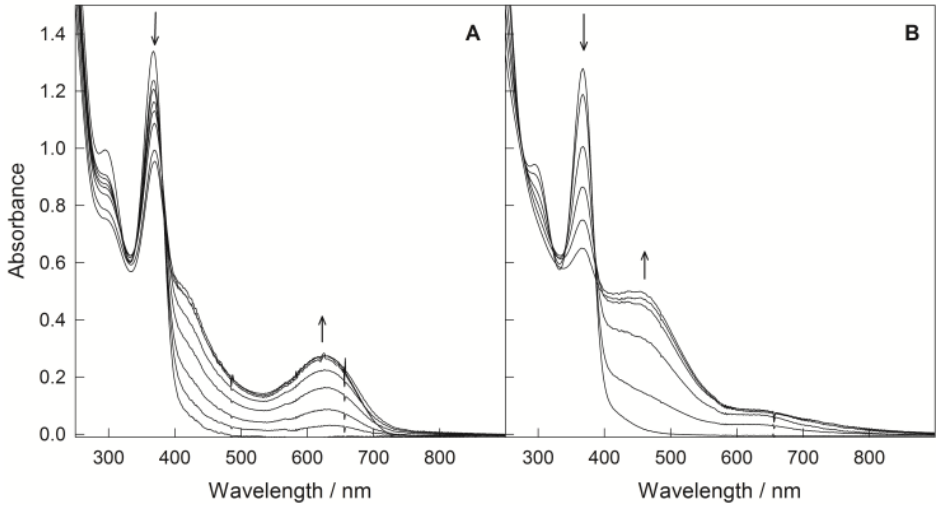

Figure 3-8. Spectra of species generated by bulk electrolysis of **4** at 1.2 V (A) and 1.5 V (B) at pH 2. Conditions:1 mM **4**, 0.1 M $NaClO_4$, 0 °C. In Figure 3-8A spectra are recorded every five minutes, in Figure 3-8B spectra are recorded every ten minutes.

At pH 13 only the iron(IV)oxo species could be generated via bulk electrolysis at potentials up to 1.2 V versus SCE, despite the evidence from cyclic voltammetry (Figure 3-6) for the existence of the iron(V)oxo species. This result agrees with that of oxidation by NaClO at pH 13, that the iron(V)oxo derivative of **4** at is unstable at pH 13.

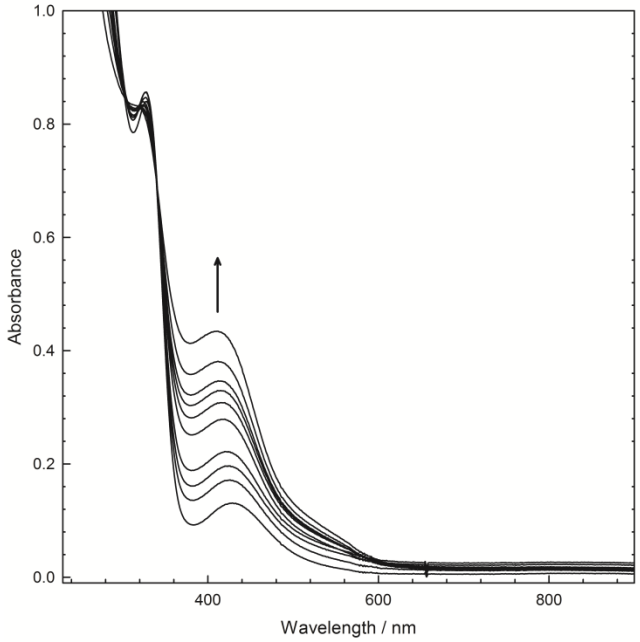

Figure 3-9. Spectra of species generate by bulk electrolysis of **4** at pH 13. Conditions: 1 mM **4**, 0.1 M $NaClO_4$, 0 °C. First three spectra from bottom were obtained after 10, 20 and 40 minutes at 0.75 V. The next three spectra are were obtained at ten minute intervals after increasing the voltage to 0.85 V. The final two spectra were obtained at ten minute intervals after increasing the voltage to 1.2 V.

While the iron(IV)oxo and iron(V)oxo species could be quantitatively generated with NaClO or in moderate yield (70-75%) electrochemically, the green one-electron oxidized species generated at pH 2 and below could be generated in only minor amounts electrochemically (Figure 3-8A) and in trace amounts with NaClO at pH 2. However, by lowering the pH to 1, one equivalent of ceric ammonium nitrate (CAN) was able to produce the iron(IV) species quantitatively at 4 °C (Figure 3-10). At this pH, no further oxidation was seen with additional equivalents of CAN. Assuming complete conversion to iron(IV), the extinction coefficient at 620 nm was determined to be 5,100 M^{-1} cm^{-1}.

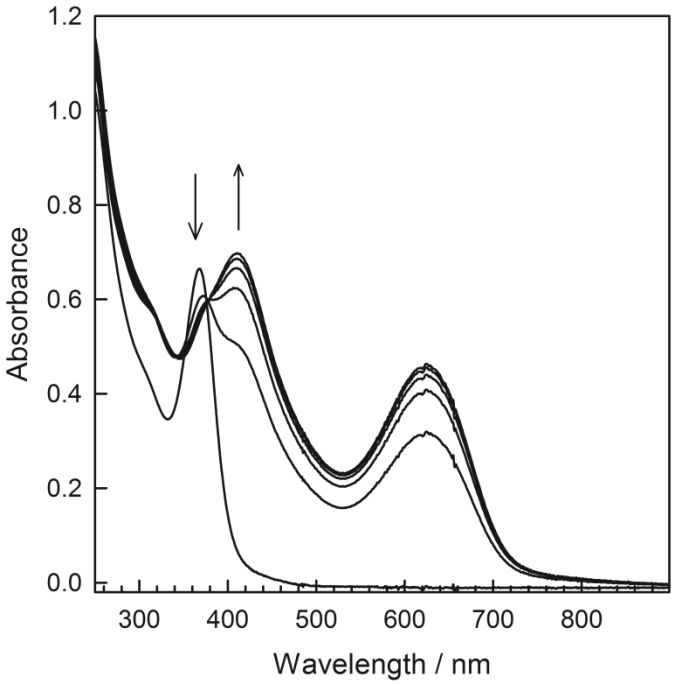

Figure 3-10. Oxidation of **4** with CAN at pH 1. Conditions: 1×10^{-4} M **4**, = 1×10^{-4} CAN M, 0.1 M $HClO_4$ 4 °C. Spectra were recorded in one second intervals after addition of CAN.

3.2.6 Reversibility of the oxidized states of 4

The observations that NaClO converts **4** into different oxidized states at different pH prompted us to study the fate of iron(V)oxo and iron(IV)oxo species generated at pH 2 and 13 on reverting the solution pH to 13 and 2, respectively. When iron(IV)oxo was generated from **4** by 0.5 equivalent NaClO at pH 13 and the solution was acidified to pH 2 with concentrated phosphoric acid, the compound underwent rapid disproportionation to afford equal quantities of iron(III) and iron(V)oxo derivatives (Scheme 1), as shown by uv-vis spectroscopy (Figure 3-11). In the former case the bands at 368 and 450 nm were developed which correspond to iron(III) and iron(V)oxo species, respectively. The EPR

evidence was even more striking because the corresponding two signals originated from the EPR silent solution of iron(IV)oxo derivative. Upon aging of the solution after disproportionation, a peak corresponding to that of iron(IV) species began to appear (Spectrum 4, Figure 3-11). Based on the minimal change to the peak at 368 nm, it is proposed that this species is generated by spontaneous one-electron reduction of the iron(V)oxo species in acidic solution to either the iron(IV)hydroxo or aqua derivative of **4**. It is also worth mentioning that the uv-vis spectrum of the iron(IV) species as shown in Figure 3-11, Spectrum 4 is produced on aging the iron(V)oxo solution at pH 2. The exponential self-decay of the oxidized derivative of **4** into the iron(IV) product occurs rather slow at 13 °C, the pseudo first-order rate constant k_{obs} being 0.013 ± 0.03 s^{-1}. In turn, iron(IV) slowly decays further to afford a mixture of **4** together with products of its deep degradation. The pseudo first-order rate constant k_{obs} for this process equals (3.1 ± 0.2) × 10^{-3} s^{-1}. The stability of the iron(IV)oxo product generated at pH 13 is much higher.

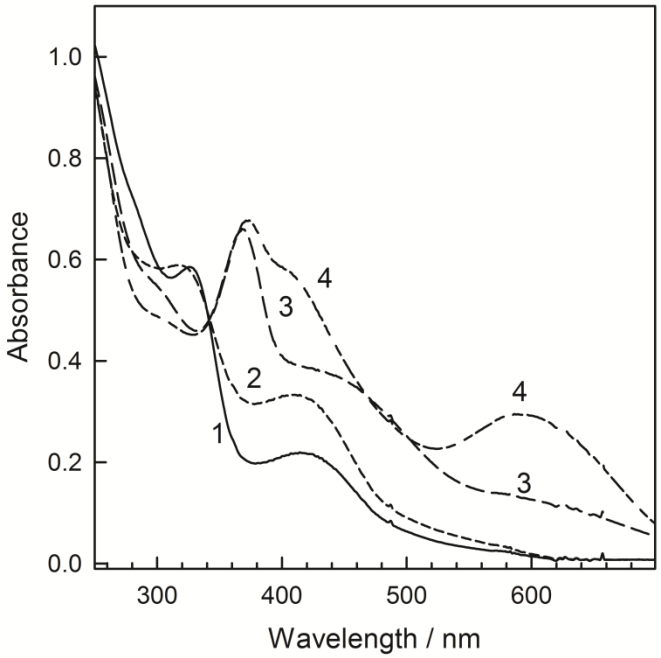

Figure 3-11. Oxidation of **4** at pH 13 followed by acidification with H_3PO_4.Conditions: 1×10^{-4} M **4**, 13 °C. Spectrum 1 is the iron(III)hydroxo form of **4**. Spectrum 2 shows the iron(IV)oxo species resulting from oxidation with 0.5 equivalents of NaClO. Spectrum 3 shows the disproportionation of iron(IV)oxo into iron(III)aqua, characterized by the peak at 368 nm, and iron(V)oxo, characterized by the broad peak at 450 nm resulting from the addition of concentrated H_3PO_4 to the reaction mixture. Spectrum 4 is the aging of this acidified solution resulting in the formation of either iron(IV)aqua or hydroxo.

The instability of iron(IV)oxo at pH 10.6 was also explored by addition of the one-electron reductant potassium ferrocyanide to a solution of iron(V)oxo **4**. Addition of one equivalent of potassium ferrocyanide to the iron(V)oxo generated at pH 10.6 with one equivalent of NaClO results in fast disproportionation into a 1:1 mixture of iron(III) and iron(V)oxo. Another equivalent of potassium ferrocyanide results in the complete recovery of iron(III) (Figure 3-12).

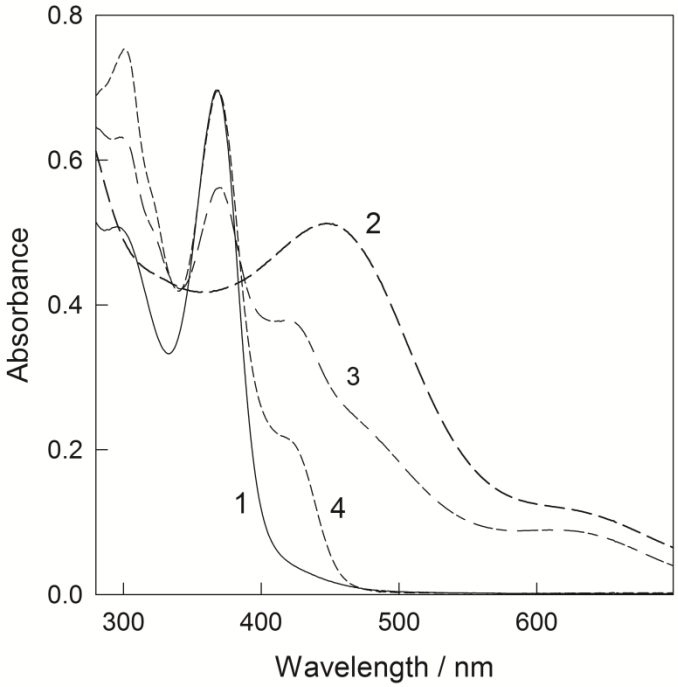

Figure 3-12. Reduction of iron(V)oxo 4 with $K_4Fe(CN)_6$ at pH 10.6. Conditions: 1×10^{-4} M **4**, 13 °C. Spectrum 1 is iron(III)aqua **4**. Spectrum 2 is the iron(V)oxo derivative upon oxidation by one equivalent of NaClO. Spectra 3 and 4 show the result of addition of two consecutive aliquots of one equivalent $K_4Fe(CN)_6$. Spectrum 3 matches the average of 2 and 4.

Further evidence of the instability of iron(IV) at intermediate pH and the unavailability of iron(V)oxo at pH 13 was obtained upon basification of a sample of iron(V)oxo **4** generated with one equivalent of NaClO at pH 10.6. After conversion of iron(III)aqua to iron(V)oxo was complete, another aliquot of iron(III) **4** was added to the sample. No reaction occurred, and the characteristic peaks for iron(III) and iron(V)oxo were both visible. When the pH was adjusted to 13, this mixed spectrum of iron(III) and iron(V)oxo changed rapidly to that of iron(IV)oxo suggested by the shift of the absorbance maximum from 450 to 410 nm (Figure 3-13). This observation raised the

question for a target for the second oxidation equivalent of NaClO at pH 13. The most likely explanation is that an iron(III) molecule is oxidized to iron(V)oxo, followed by comproportionation with a remaining iron(III) molecule to form two iron(IV)oxo molecules. A similar mechanism is seen with **1a**, however the result of comproportionation is the iron(IV)(μ-oxo) dimer species. This was tested by adding ¼ of an equivalent of sodium hypochlorite to a solution of iron(III) **4** at pH 13. Both uv-vis and EPR spin quantification showed 50 % of iron(III) remained, as opposed to 75 % had the iron(V) intermediate been reduced by some other electron donor.

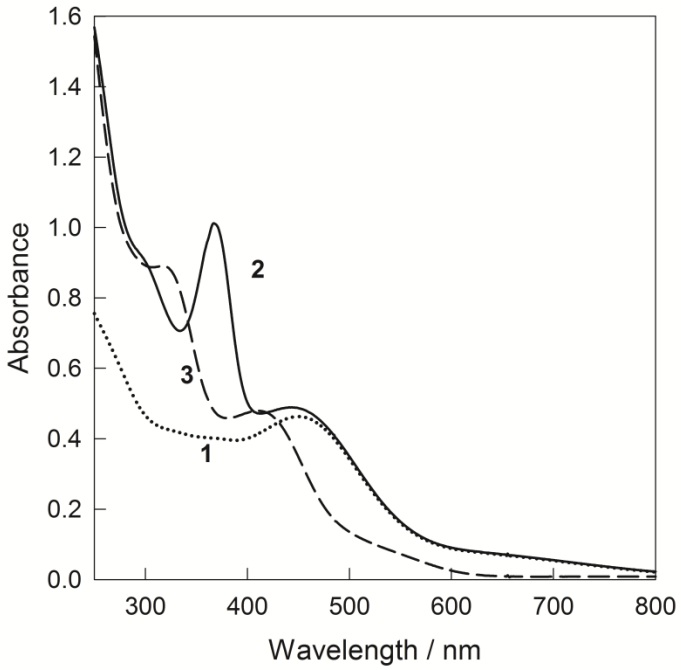

Figure 3-13. Spectral changes occurring from the addition of base to iron(V)oxo **4** Conditions: 2 aliquots of 1×10^{-4} M **4**, Carmody buffer at pH 10.6, 13 °C. Spectrum 1 shows the iron(V)oxo species generated with one equivalent of NaClO at pH 10.6. Spectrum 2 shows the addition of an additional aliquot of iron(III)aqua to the reaction mixture. Spectrum three is obtained upon addition of concentrated NaOH.

3.2.7 Nature of the Iron(IV) Product Generated at Low pH

The iron(IV)oxo and iron(V)oxo complexes generated chemically and electrochemically in this work were straightforward to characterize as they have precedent, although not in water for the iron(V)oxo. The nature of the iron(IV) complex generated at low pH was of significant interest to us due to its novelty. Of additional interest, EPR evidence indicates that this species is a high-spin (S = 2) iron complex. High-spin iron(IV)oxo complexes are of great interest in the inorganic chemistry community, due to their higher reactivity and similarity to metalloenzymes.[26,27] However, Collins' [$Fe^{IV}Cl(\eta^4$-MAC*)] (Figure 3-14) remains the only reported non-oxo high-spin iron(IV) complex.[28]

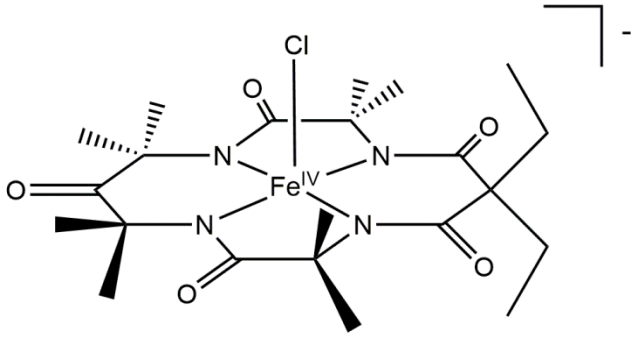

Figure 3-14. High-spin iron(IV) complex [$Fe^{IV}Cl(\eta^4$-MAC*)]

The most likely options for the iron(IV) species in question would be iron(IV)aqua or iron(IV)hydroxo. As discussed in Section 3.2.4 the cyclic voltammograms for **4** are reversible and show no change in potential from pH 2 to 4. This indicates a one-electron transfer, producing the iron(IV)aqua complex. Similar chemistry was reported by Meyer and coworkers in the pH-dependent redox couples of $[(trpy)(bpy)M(OH_{2})]^{+}$ (M = Ru, Os; trpy = 2,2',2"-terpyridine; bpy = 2,2'-bipyridine).

For both ruthenium and osmium at pH 1.5 and below the M(III/II) couple is pH independent, indicating no proton-coupled electron transfer. At high potential, there is a pH dependent M(IV/III) couple with a slope of 120 mV/pH, indication a $2H^+/1e^-$ proton-coupled oxidation.[29]

The characterization of an iron(IV)hydroxo complex would be intriguing, as no synthetic iron(IV)hydroxo complexes have yet been prepared. It is possible that the iron(IV) species seen at low pH is the hydroxo complex. However, it could be that the iron(IV)hydroxo derivative of **4** is unstable, leading to the disproportionation seen upon acidification of the iron(IV)oxo complex, as well as from adding $K_4Fe(CN)_6$ to iron(V)oxo at intermediate pH. This may also explain the somewhat confusing pH dependent cyclic voltammograms seen in the range of 4.5 to 10.5. The iron(IV)hydroxo complex may be produced by proton-coupled electron transfer, followed by disproportionation to iron(III)aqua and iron(V)oxo.

Chloride ions are known to bind to TAML activators as axial ligands in aqueous solution according to Equation 3–3, although usually only at high $[Cl^-]$. As **4** is synthesized from iron trichloride, and both NaClO and the saturated calomel reference electrode could introduce trace amounts of chloride into solution, the existence of an iron(IV)chloro species could not be ruled out. Therefore the equilibrium constant for both iron(III) and iron(IV) **4** at pH 1 were measured by spectrophotometric titration. Figure 3-15 shows the changes in the uv-vis spectra of **4** upon addition of sodium chloride up to 2 M. For the iron(III) **4**, increasing $[Cl^-]$ results in a light decrease in the absorbance at 368 nm. For iron(IV) **4** the peak at 620 nm decreases and shifts to 600 nm at high $[Cl^-]$. Figure 3-16 shows the absorbance at 368 nm for iron(III) and 620 nm for iron(IV) plotted

as a function of [Cl^-]. The data in Figure 3-16 was fitted to Equation 3–4 in order to determine the equilibrium constants for each species. Here A is the absorbance at a given concentration of chloride, A_0 is the absorbance with no added chloride and A_∞ would be the absorbance at infinite [Cl^-], and K_{Cl} is the equilibrium constant for chloride binding to **4** in the axial position.

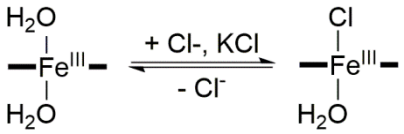

(3–3)

$$A = \frac{A_0 + A_\infty K_{Cl}[Cl^-]}{1 + K_{Cl}[Cl^-]} \qquad (3-4)$$

The equilibrium constants obtained from this data were 0.128 ± 0.007 M^{-1} for the iron(III)chloro species and 2.4 ± 0.5 for the iron(IV)chloro species. The equilibrium constant for the iron(IV) species is over an order of magnitude higher than that for iron(III), however, it would still require 0.4 M Cl^- in order for iron(IV)chloro to be present in solution in equimolar amounts with the iron(IV)aqua/hydroxo complex. This concentration is much higher than that introduced by adding NaClO as a reagent, or from ion leaching from the reference electrode into the electrolysis solution.

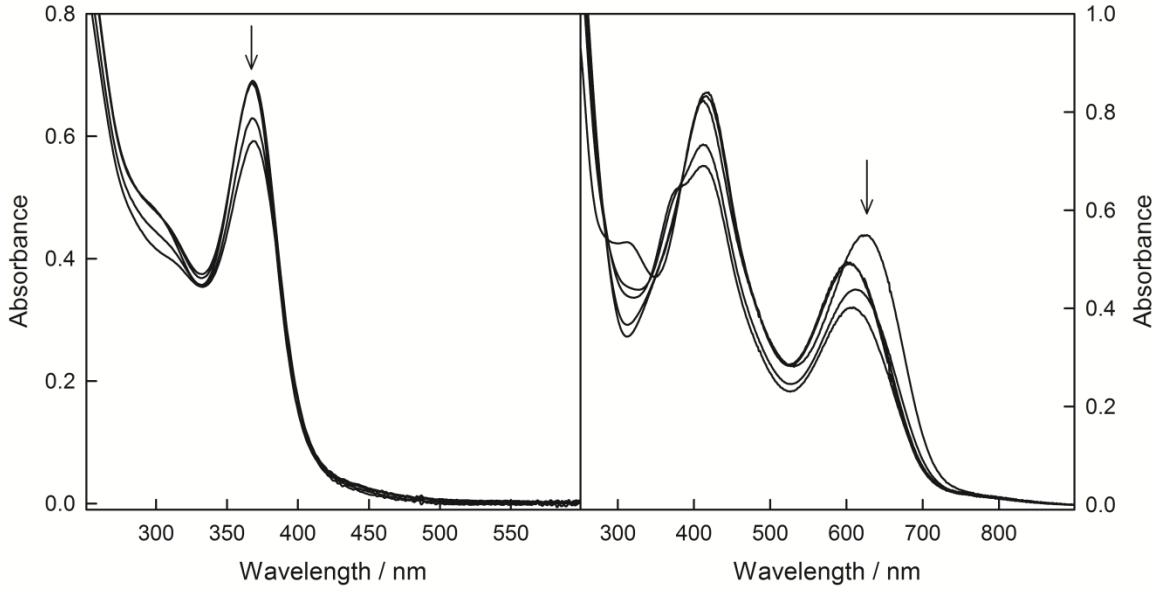

Figure 3-15. Spectral changes of iron(III) (left) and iron(IV) (right) **4** on increasing [Cl^-]. Conditions: 1×10^{-4} M **4**, 0-2 M Cl^-, 0.1 M $HClO_4$, 4 °C.

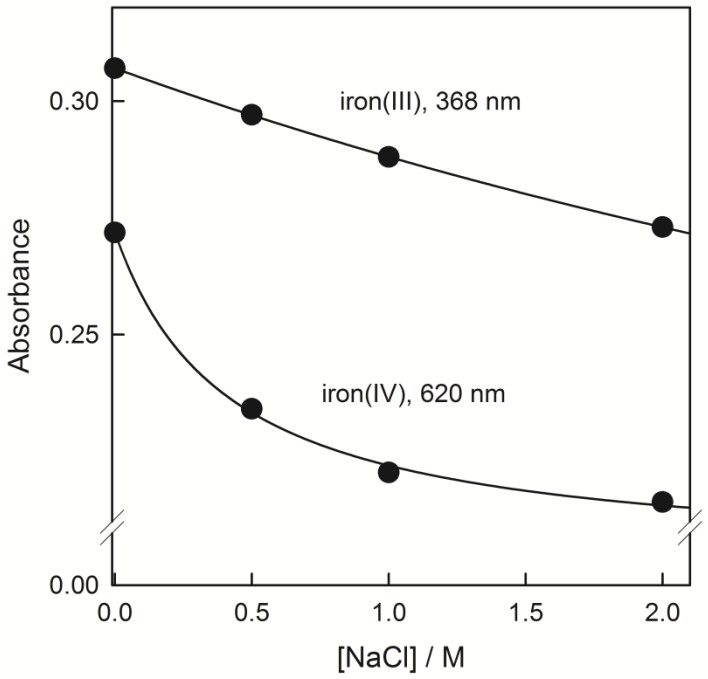

Figure 3-16. Absorbance at the λ_{max} for iron(III) and iron(IV) **4** as a function of [Cl^-]. Conditions: 1×10^{-4} M **4**, 0-2 M Cl^-, 0.1 M $HClO_4$, 4 °C.

To further prove that iron(IV)chloro is not present in significant concentrations in the chemical or electrochemically prepared iron(IV) samples, an EPR sample was prepared in the presence of 1 M NaCl using CAN at pH 1, where the concentration of the iron(IV)chloro species should be greater than 85% (Figure 3-17). The spectrum of the high chloride sample was distinctly different than the sample prepared with no added chloride, although both were high spin complexes.

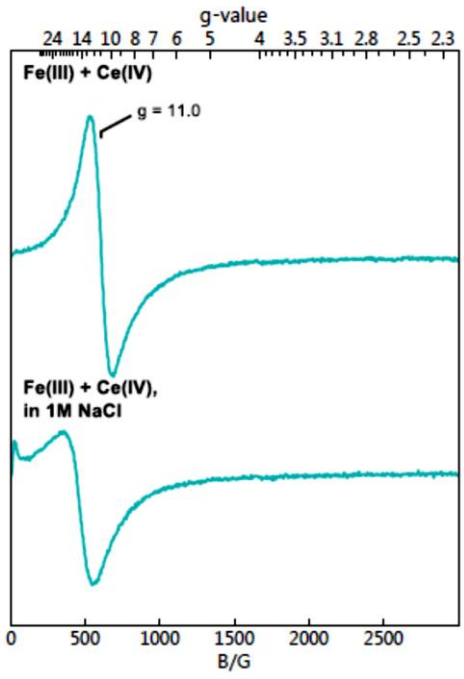

Figure 3-17. EPR spectra of iron(IV) samples generated by oxidation with CAN with and without added chloride. Conditions: 5×10^{-4} M **4,** 5×10^{-4} M CAN, 0.1 M $HClO_4$, 25 °C, 10 % glycerol.

3.3 Conclusion

In conclusion, TAML activator **4** allows for the chemical and electrochemical generation of a number of high-valent iron complexes in water. The iron(V)oxo derivative of TAMLs activator **4** can be readily generated by NaClO throughout the pH range of 2.0–10.5 and is sufficiently stable at 13 °C for investigating its properties and reactivity. This species can also be generated by electrolysis at 1.5 V versus SCE at pH 2. At pH 13 the iron(V)oxo species is not produced and the iron(IV)oxo compound is formed instead. Acidification of the latter induces the unprecedented disproportionation leading to the mixture of iron(III) and iron(V)oxo species.

Furthermore, at pH 2, a novel high-spin iron(IV) species can be generated by electrolysis at 1.2 V, or by reaction with one equivalent of CAN. This species can exist as either an iron(IV)aqua or hydroxo species, or as the iron(IV)chloro complex. These complexes would represent the first spectroscopically characterized S = 2 iron(IV) non-oxo complexes reported since 1993.

3.4 Experimental

3.4.1 Materials

TAML **4** was synthesized as previously described.[11] The ^{57}Fe-enriched **4** was prepared by metalation with ^{57}Fe-enriched $FeCl_3$. The ^{57}Fe-enriched $FeCl_3$ was synthesized by bubbling HCl gas through a suspension of ^{57}Fe-enriched iron powder in dry ethanol. After two hours the solvent was removed with rotary evaporation. The remaining solid was put under high vacuum overnight and used without further purification. Sodium hypochlorite solutions were obtained from Fisher Scientific and standardized daily by measuring the absorbance at 292 nm in pH 11 phosphate buffer ($\varepsilon = 360\ M^{-1}\ cm^{-1}$).[30]

3.4.2 Uv-vis spectroscopy

UV-Vis spectral studies were carried out using an HP 8453A diode array spectrophotometer. Low-temperature spectral studies were preformed using a liquid nitrogen cooled cryostat set-up from UNISOKU Scientific Instruments, Japan.

3.4.3 Electrochemistry

Electrochemical studies were performed with an Autolab PGSTAT100. The working electrode was a glassy carbon disk, with a saturated calomel reference electrode and

platinum wire counter electrode. For bulk electrolysis, the working electrode was a platinum coil.

3.4.4 Spectrophotometric Chloride Titration

Solutions of 1×10^{-4} M **4** were prepared in 0.1 M $HClO_4$ with the desired concentration of sodium chloride. This was cooled to 4 °C using the cryostat set-up. The initial spectrum was recorded and saved as iron(III). One equivalent of a fresh cerium(IV) ammonium nitrate solution in 0.1 M $HClO_4$ was added to produce the iron(IV) complex. The spectrum at maximum absorbance at 620 nm was recorded as the final spectrum.

3.4.5 EPR Spectroscopy

EPR Spectroscopy X-band EPR spectra was recorded on a Bruker 300 spectrometer equipped with an Oxford ESR-910 liquid helium cryostat. The signal was quantified relative to a CuEDTA spin standard. For both instruments, the microwave frequency was calibrated with a frequency counter and the magnetic field with an NMR gaussmeter. A modulation frequency of 100 kHz was used for the EPR spectra. The EPR simulation software (Spin Count) was written by one of the authors.[31] The software diagonalizes the spin Hamiltonian, (Equation 3–5) where S is the total spin of the complex (unless explicitly stated otherwise) and the parameters have the usual definitions. The quantitative simulation was least-squares fit of the experimental spectra generated with consideration of the intensity factor, which allows the computation of simulated spectra for a specified sample concentration.

$$\mathrm{H} = \beta \mathrm{eBgS} + \mathrm{S.D.S} + \mathrm{S.A.I} \qquad (3-5)$$

3.4.6 Mössbauer Spectroscopy

Mössbauer spectra were recorded with two spectrometers using a Janis Research SuperVaritemp dewar. The isomer shift was reported relative to Fe metal. The simulation of the Mössbauer spectra was calculated with least-square fitting using the program *SpinCount* and the standard spin Hamiltonian (Equation 3–6)

$$H = \beta eBgS + S.D.S + S.A.I - g_n b_n B.I + \frac{eQV_{zz}}{12}\left[3I_z^2 - I(I+1) + \eta\left(I_x^2 - I_y^2\right)\right] \quad (3-6)$$

3.5 References

1. Tinberg, E. C.; Lippard, J. S. *Acc. Chem. Res.* **2011**, *44*, 280–288.

2. Coon, M. J. *Annu. Rev. Pharmacol. Toxicol.* **2005**, *45*, 1–25.

3. Pallan, P. S.; Wang, C.; Lei, L.; Yoshimoto, F. K.; Auchus, R. J.; Waterman, M. R.; Guengerich, F. P.; Egli, M. *J. Biol. Chem.* **2015**, *290*, 13128-13143.

4. Hanna, I. H.; Dawling, S.; Roodi, N.; Guengerich, F. P.; Parl, F. F. *Cancer Res.* **2000**, *60*, 3440–3444.

5. Wang, B.; Sanchez, R. I.; Franklin, R. B.; Evans, D. C.; Huskey, S.-E. W. *Drug Metab. Dispos.* **2004**, *32*, 1209–1212.

6. Yosca, T. H.; Rittle, J.; Krest, C. M.; Onderko, E. L.; Silakov, A.; Calixto, J. C.; Behan, R. K.; Green, M. T. *Science* **2013**, *342*, 825–829.

7. de Oliveira, F. T.; Chanda, A.; Banerjee, D.; Shan, X. P.; Mondal, S.; Que, L.; Bominaar, E. L.; Munck, E.; Collins, T. J. *Science* **2007**, *315*, 835–838.

8. Lyakin, O. Y.; Bryliakov, K. P.; Britovsek, G. J. P.; Talsi, E. P. *J. Am. Chem. Soc.* **2009**, *131*, 10798–10799.

9. Pan, Z.; Wang, Q.; Sheng, X.; Horner, J. H.; Newcomb, M. *J. Am. Chem. Soc.* **2009**, *131*, 2621–2628.

10. Van Heuvelen, K. M.; Fiedler, a. T.; Shan, X.; De Hont, R. F.; Meier, K. K.; Bominaar, E. L.; Munck, E.; Que, L. *Proc. Natl. Acad. Sci.* **2012**, *109*, 11933–11938.

11. Kwon, E.; Cho, K.-B.; Hong, S.; Nam, W. *Chem. Commun. (Cambridge, U. K.)* **2014**, *50*, 5572–5575.

12. Ren, Q.; Guo, Y.; Mills, M. R.; Ryabov, A. D.; Collins, T. J. *Eur. J. Inorg. Chem.* **2015**, *2015*, 1445–1452.

13. Ryabov, A. D. *Adv. Inorg. Chem.* **2013**, *65*, 117–163.

14. Panda, C.; Debgupta, J.; Díaz, D. D.; Singh, K. K.; Gupta, S. Sen; Dhar, B. B.; Díaz Díaz, D.; Singh, K. K.; Sen Gupta, S.; Dhar, B. B. *J. Am. Chem. Soc.* **2014**, *136*, 12273–12282.

15. Singh, K. K.; Tiwari, M. K.; Ghosh, M.; Panda, C.; Weitz, A.; Hendrich, M. P.; Dhar, B. B.; Vanka, K.; Sen Gupta, S. *Inorg. Chem.* **2015**, *54*, 1535–1542.

16. DeNardo, M. A.; Mills, M. R.; Ryabov, A. D.; Collins, T. J. *J. Am. Chem. Soc.* **2016**, *138*, 2933–2936.

17. Chanda, A.; Shan, X.; Chakrabarti, M.; Ellis, W. C.; Popescu, D. L.; De Oliveira, F. T.; Wang, D.; Que, L.; Collins, T. J.; Münck, E.; Bominaar, E. L. *Inorg. Chem.* **2008**, *47*, 3669–3678.

18. Demeter, E. L.; Hilburg, S. L.; Washburn, N. R.; Collins, T. J.; Kitchin, J. R. *J. Am. Chem. Soc.* **2014**, *136*, 5603–5606.

19. Popescu, D. L.; Vrabel, M.; Brausam, A.; Madsen, P.; Lente, G.; Fábián, I.; Ryabov, A. D.; Van Eldik, R.; Collins, T. J. *Inorg. Chem.* **2010**, *49*, 11439–11448.

20. Chanda, A.; Shan, X.; Chakrabarti, M.; Ellis, W. C.; Popescu, D. L.; De Oliveira, F. T.; Wang, D.; Que, L.; Collins, T. J.; M??nck, E.; Bominaar, E. L. *Inorg. Chem.* **2008**, *47*, 3669–3678.

21. Ghosh, A.; de Oliveira, F. T.; Yano, T.; Nishioka, T.; Beach, E. S.; Kinoshita, I.; Münck, E.; Ryabov, A. D.; Horwitz, C. P.; Collins, T. J. *J. Am. Chem. Soc.* **2005**, *127*, 2505–2513.

22. Mills, M. R.; Burton, A. E.; Mori, D. I.; Ryabov, A. D.; Collins, T. J. *J. Coord. Chem.* **2015**, *68*, 3046–3057.

23. Kundu, S.; Van Kirk Thompson, J.; Ryabov, A. D.; Collins, T. J. *J. Am. Chem. Soc.* **2011**, *133*, 18546–18549.

24. Slattery, S. J.; Blaho, J. K.; Lehnes, J.; Goldsby, K. A. *Coord. Chem. Rev.* **1998**, *174*, 391–416.

25. Bordwell, F. G.; Cheng, J.-P.; Ji, G. Z.; Satish, A. V.; Zhang, X. *J. Am. Chem. Soc.* **1991**, *113*, 9790–9795.

26. Bae, S. H.; Seo, M. S.; Lee, Y.-M.; Cho, K.-B.; Kim, W.-S.; Nam, W. *Angew. Chemie Int. Ed.* **2016**, *55*, 8027–8031.

27. Kleespies, S. T.; Oloo, W. N.; Mukherjee, A.; Que, L. *Inorg. Chem.* **2015**, *54*, 5053–5064.

28. Kostka, K. L.; Fox, B. G.; Hendrich, M. P.; Collins, T. J.; Rickard, C. E. F.; Wright, L. J.; Munck, E. *J. Am. Chem. Soc.* **1993**, *115*, 6746–6757.

29. Takeuchi, K. J.; Thompson, M. S.; Pipes, D. W.; Meyer, T. J. *Inorg. Chem. J. Chem. Phys* **1984**, *23*, 1845–1851.

30. Hussain, A.; Trudell, P.; Repta, A. J. *J. Pharm. Sci.* **1970**, *59*, 1168–1170.

31. Petasis, D. T.; Hendrich, M. P., *Methods Enzymol.* **2015,** *563*, 171-208.

Chapter 4

Properties of TAML Activators as Homogeneous and Heterogeneous Electrocatalysts for Oxygen Evolution from Water under Alkaline Conditions

4.1 Introduction

One of the major components of sustainability is clean energy production. Carbon-based energy production results in the release of massive amounts of carbon dioxide into the environment, which is already having effects on global climate.[1–4] Renewable energy is increasing as a portion of the energy market,[5] but the most common types of renewable energy, wind and solar, suffer from intermittency issues. As such, the photochemical generation of fuels offers a great deal of promise in the storage and transport of solar energy. Photochemical water splitting to produce hydrogen and oxygen gas would mimic photosynthesis and offers one of the most desirable systems for producing solar fuel. The half-reactions for hydrogen and oxygen production from water are given in equations 4–1 and 4–2, respectively, with the overall reaction given in equation 4–3. Hydrogen gas produced from water splitting is of special interest, in that it offers the potential for a closed-loop system, as it can be used in combustion or fuel cells, and the resulting product would be water.

$$4\ H^+ + 4\ e^- \rightarrow 2\ H_2 \qquad (4–1)$$

$$2\ H_2O \rightarrow O_2 + 4\ H^+ + 4\ e^- \qquad (4–2)$$

$$2\ H_2O \rightarrow 2\ H_2 + O_2 \qquad (4–3)$$

These seemingly simple half-cell reactions belie the complex chemistry that must occur in order to achieve this process efficiently. Much work on hydrogen production has resulted in quite efficient catalysts for this purpose.[6] A greater challenge remains with the complementary half-reaction, water oxidation to dioxygen, especially for photo-catalyzed evolution of oxygen from water.[7]

A number of molecular water oxidation catalysts have been prepared, with the first report being the 'blue dimer' ruthenium compound synthesized by Meyer and coworkers.[8] Since then molecular catalysts for oxygen evolution featuring ruthenium,[9–13] iridium,[14–17] manganese,[18–20] cobalt,[21–23] copper,[24–26] and iron[27–31] have been prepared. The ruthenium and iridium catalysts tend to offer the best activity of these catalysts, but have limited large-scale potential due to costs of the metal. Iron, cobalt, and copper offer advantages on a cost basis but are limited by performance or stability issues. TAML activators are among the iron-based catalysts that have been shown to catalytically oxidize water. Under acidic conditions, TAML activators evolve oxygen with cerium(IV) ammonium nitrate (CAN) as a sacrificial oxidant.[27] Sen Gupta and others have performed photochemical water oxidation with a biuret-modified TAML catalyst at pH 8.7 and found TON of 220 and turnover frequency (TOF) of 0.67 s^{-1}.[30] TAML activators have also been bound to an electrode for heterogeneous oxygen evolution from acidic solution.[32] Except for that of photochemical oxygen evolution, these studies utilized TAML activators at low pH, thereby limiting TOF due to lower reactivity of the catalysts at low pH and the TON due to acid-induced demetalation of the catalysts. However, to date, no studies have been conducted with TAML activators for the catalyzed oxidation of water to dioxygen under alkaline conditions. With the increasing interest in earth-abundant metal catalysts for the oxygen evolution reaction this work was undertaken with the goal of determining whether TAML activators could act as highly efficient electrocatalysts for this reaction.

4.2 Results and Discussion

4.2.1 TAML activators as Homogeneous Electrocatalysts for Oxygen Evolution.

In studying the electrochemical properties of **4**, it was observed that at high pH (>10.5), a catalytic wave began to appear at around 0.7 V versus SCE. The current continues to increase as the pH is increased to 13 even with background correction. Upon completion of a scan from 0 to 1.05 V at pH 13, bubbles could be seen on the working electrode. When the potential of the working electrode was held at 1 V versus SCE, extensive production of gas was observed. The most likely explanation for voltammograms exhibiting catalytic waves in the absence of any added substrate and the evolution of gas from the working electrode would be the oxidation of water (or hydroxide) to form dioxygen. Similar irreversible waves for **1a** had been observed previously in our group at pH 12.6 and attributed to the existence of multiple oxidized species.[33] Considering the possibility that these waves instead indicated electrocatalytic oxygen evolution, the cyclic voltammograms for both **1a** and **4** at pH 13 were therefore run under similar conditions for comparison (Figure 4-1).

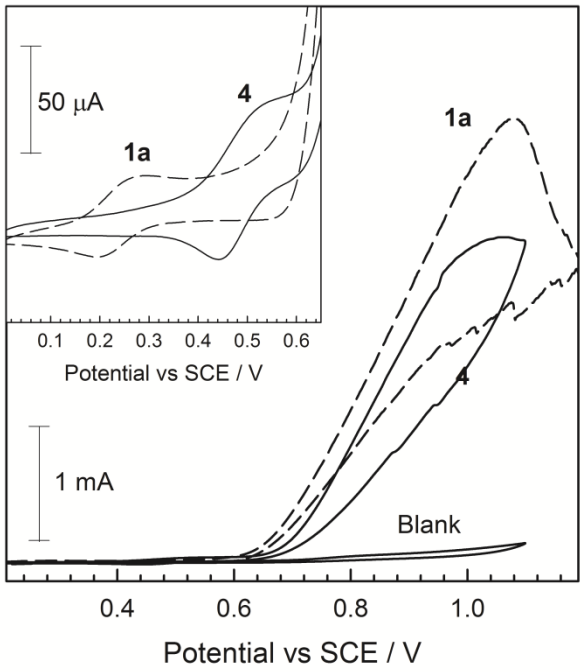

Figure 4-1. Cyclic voltammograms for **1a** and **4** at pH 13. Conditions: 5 mM catalyst, 0.1 M NaOH, 100 mV s^{-1} scan rate.

Figure 4-1 shows that with 5 mM catalyst, large catalytic waves are seen for both **1a** and **4**. Catalyst **1a** shows both increased current and more negative onset potential relative to **4**. The inset to Figure 4-1 shows quasi-reversible waves for both **1a** and **4** preceding the onset of the catalytic wave. Of interest is that splitting of the iron(IV/III) and iron(V/IV) waves of **4** discussed in Section 3.2.4 is not apparent. This difference may be due to the absence of buffer in the samples measured in Figure 4-1. Also of note, is that potential of the iron(IV/III) wave for **1a** occurs is 200 mV more negative than for **4**. This would seem counterintuitive, as **4** is significantly more electron rich than **1a**. However this may be justified if the wave for **4** represents an iron(V/III) couple. If this is the case the catalytic waves for both catalysts initiate upon reaching the iron(V) state. For

1a only the catalytic wave is seen, indicating that iron(V) **1a** very rapidly turns over. The catalytic wave for **4** occurs slightly after the presumed iron(V) species is formed, possibly indicating slower catalytic performance. This would be consistent with the decreased reactivity of **4** relative to **1a** with respect to the oxidation of Orange II with hydrogen peroxide as discussed in Chapter 1. With this in mind, further studies to determine the efficiency of oxygen evolution were performed with **1a**, as it is more effective than **4**, and is more representative of TAML catalysts in general.

4.2.2 Determination of Turnover Frequency for 1a in Homogeneous Oxygen Evolution.

Under purely kinetic conditions, where the rate of electron transfer to the catalyst is not rate-limiting, voltammograms should display a plateau current, which is independent of scan rate.[34] The determination of rate constants for homogeneous electrocatalytic water splitting should be thus straightforward using cyclic voltammetry. The plateau current can be calculated by Equation 4–4, where n_{cat} is the number of electrons transferred in the catalytic reaction, F is Faraday's constant, A is the surface area of the electrode in cm^{-2}, [cat]* is the concentration of catalyst in bulk solution in mol cm^{-3}, D is the diffusion coefficient of the catalyst in cm s^{-1} , ν is the scan rate in V s^{-1} , and k_{cat} is the pseudo-first order rate constant ($k_{cat} = k[S]$), often reported as TOF.

$$i_{cat} = n_{cat}FA[cat]^{*}\sqrt{k_{cat}D} \qquad (4-4)$$

The Randles-Sevcik equation (4–5) gives the peak current for a reversible wave, where n_p is the number of electrons transferred in redox couple.

$$i_{\mathrm{p}} = n_{\mathrm{p}}\mathrm{FA}[\mathrm{cat}]^{*}\sqrt{\frac{n_{\mathrm{p}}\mathrm{FD}\nu}{\mathrm{R}T}} \qquad (4-5)$$

Dividing i_{cat} by i_p yields Equation 4–6.

$$\frac{i_{\mathrm{cat}}}{i_{\mathrm{p}}} = \frac{n_{\mathrm{cat}}}{0.4463 n_{\mathrm{p}}}\sqrt{\frac{k_{\mathrm{cat}}\mathrm{R}T}{n_{\mathrm{p}}\mathrm{F}\nu}} \qquad (6)$$

Thus, by plotting i_{cat} / i_p versus $\nu^{-1/2}$ the pseudo-first order rate constant k_{cat} can be obtained from the slope.

In the case of TAML catalysts in 1 M NaOH, this analysis is not so straightforward, as no reversible scan could be seen under these conditions. However, if the diffusion coefficient for the catalyst were known, Equation 4–4 would allow us to calculate the TOF from the scan rate-independent plateau currents. In Chapter 3 the unique electrochemical properties of **4**, which displays classical reversible voltammograms at pH 2, were discussed. Analysis of the dependence of the peak currents versus the square root of the scan rate allowed us to calculate a diffusion coefficient of 3.4×10^{-6} cm^2 s^{-1} (Figure 3–4). While it would be more desirable to determine this value at pH 14, **4** does not show completely reversible behavior at this pH. The calculated value for D is close to those of similar transition metal catalysts in water and Costentin has used the generic value of 5×10^{-6} cm^2 s^{-1} to compare catalysts for which no diffusion constant was reported. Therefore the value of 3.4×10^{-6} cm^2 s^{-1} for D was used for all TAML catalysts in this study.

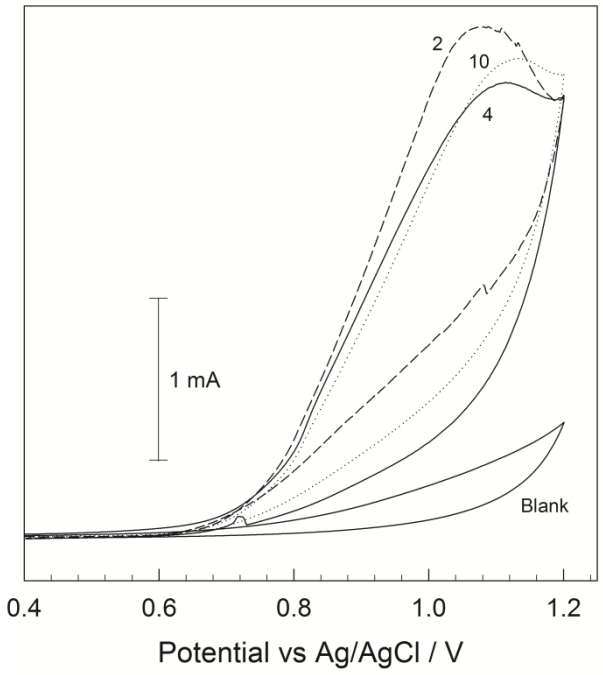

Figure 4-2. Cyclic voltammograms of **1a** in 1 M NaOH. Scans were conducted at 2, 4, 6, 8, and 10 mV s^{-1}. Conditions: [**1a**] = 5×10^{-4} M, 25 °C.

Figure 4-2 shows the voltammograms from scan rates 2-10 mV s^{-1}, with plateau currents between 1.1 and 1.2 V, which are all approximately equal at 2.2 mA. This corresponds to a value for k_{cat} or TOF of 1000 ± 100 s^{-1}. This value is approximately half that of a pentanuclear iron catalyst in a recently published report claiming a TOF of 1900 s^{1}.[31] The advantage of **1a** is that it is stable in 1 M NaOH, while the other study was conducted in an acetonitrile/water mixture. Catalyst **1a** also greatly outperforms the first reported iron-based molecular electrocatalyst for homogeneous oxygen evolution, published by Meyer and coworkers in 2014, which had a TOF of 1 s^{-1} in propylene carbonate with 8% water.[28] No other iron-based catalysts higher TOF values for electrocatalytic oxidation of water to dioxygen.

4.2.3 In-Situ Generated Heterogeneous Catalyst

The scans shown in Figure 4-2 were obtained immediately after preparing the electrode by polishing with 0.05 μm alumina, followed by oxidation at 1.2 V vs Ag/AgCl in 1 M NaOH for 30 minutes. When trying to apply Equation 4–6 to **1a**, it became apparent that homogeneous water oxidation was note the sole reaction occurring. Successive scans at the same scan rate yielded higher peak currents each time, especially at lower scan rates (Figure 4-3). As the catalytic currents increased with successive scans, the possibility that **1a** was undergoing electrodeposition onto the working electrode was investigated.

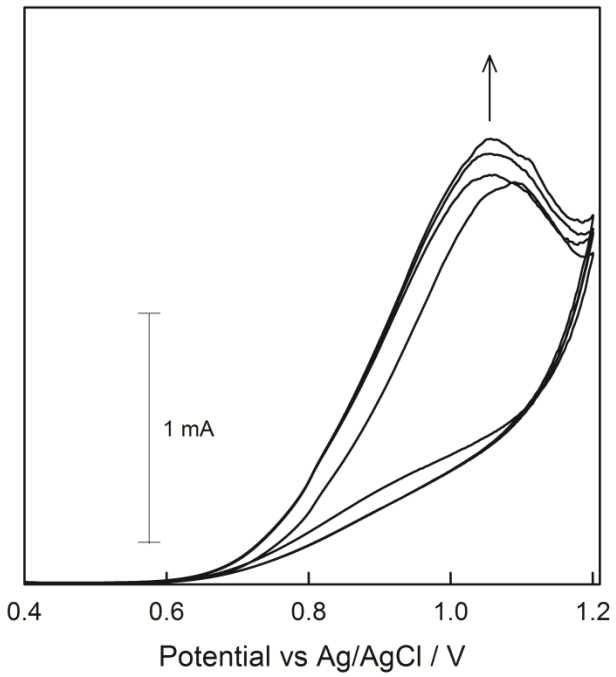

Figure 4-3. Four successive cyclic voltammograms of **1a** with increasing peak current. Conditions: 5×10^{-4} M **1a**, 1 M NaOH, 2 mV s^{-1}, 25 °C.

4.2.4 Catalytic Activity of TAML-Activated Electrode

4.2.4.1 Electrodeposition of 1a and Resulting Overpotential

A recent report by McCrory, Peters and Jaramillo has outlined a protocol for benchmarking heterogeneous water oxidation catalysts.[35] As this report gave a set of standard tests that could be conducted under alkaline conditions that were favorable to TAML-catalyzed electrocatalytic water oxidation it was used as a template for analyzing the reactivity of a TAML-activated electrode.

The first study conducted was to determine when the electrode was effectively saturated with **1a**. This was done by conducting a potentiometric study wherein the current was set to 1.96 mA with a glassy carbon disk set to rotate at 1600 rpm in a solution of 5×10^{-4} M **1a**. The value of 1.96 mA corresponds to 10 mA per square centimeter of electrode, which is approximately the current density expected at the anode in a 10% efficient solar water-splitting device under 1 sun illumination.[35] As seen in Figure 4-4, the potential required to provide 10 mA cm^{-2} was initially 1.3 V versus Ag/AgCl, but drops to 0.60 V over the course of one hour as the catalyst is electrodeposited. That is a 700 mV decrease in the potential required to generate the desired current. After electrodeposition of the catalyst is complete, a current density of 10 mA cm^{-2} is produced at an overpotential (η) of 400 mV with respect to the thermodynamic potential of 200 mV vs Ag/AgCl at pH 14. This is comparable performance to several of the metal oxides tested by the authors of the benchmarking paper.[35] A freshly polished electrode with no catalyst in solution required a potential of 1.47 V versus Ag/AgCl in order to produce 10 mA cm^{-2}, and maintained this potential

over two hours. The electrodeposition process took approximately 60 minutes for completion, but it is possible that the time could be shortened if more concentrated catalyst solution was used. That catalyst **1a** can be easily electrodeposited onto a glassy carbon working electrode through a potentiometric study was a surprising result, especially as it yields an activated electrode for heterogeneous electrocatalytic oxygen evolution from 1 M NaOH. In terms of overpotential, the **1a**-activated electrode is on par with metal oxides such as IrO_x (η = 320 mV), CoO_x (η = 390 mV), $CoFeO_x$ (η = 370 mV), and $NiMO_x$ (M = Ce, Co, Cu, Fe, La; η = 350-430 mV).[35]

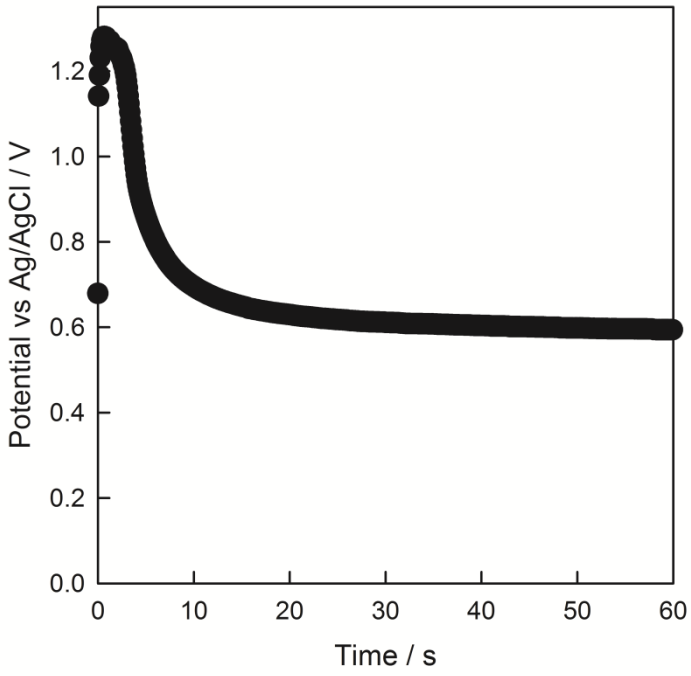

Figure 4-4. Potentiometric study of in-situ preparation of **1a**-activated electrode. Conditions: 1 M NaOH, current set to 1.96 mA. 0.196 cm^2 glassy carbon working electrode, 1600 rpm rotation rate, 25 °C.

4.2.4.2 Faradaic Efficiency of 1a-Catalyzed Water Oxidation

Qualitatively, the homogeneous electrocatalytic oxygen evolution, discussed in Section 4.2.2, and heterogeneous electrocatalytic oxygen evolution, discussed in Section 4.2.3, is quite efficient, as bubbles readily appeared on the electrode on oxidation. In fact, bubble formation on the working electrode was a significant hindrance to performing still cyclic voltammetry experiments, as the bubbles would cover the electrode surface making the voltammograms quite noisy. However, in order to effectively compare the **1a**-catalyzed system, it was necessary to quantify the amount of oxygen produced compared to the energy input. Therefore, the Faradaic efficiency (FE) of the system was tested with a rotating ring-disk coulometric study. A rotating ring-disk electrode system consists of a central disk electrode (glassy carbon in this case), surrounded by a second electrode in the shape of a ring around the central disk. The two electrodes are separated by an insulating material, and the potential for each electrode can be set separately by the potentiostat. By measuring the current due to oxygen reduction to hydrogen peroxide at the platinum ring electrode and dividing by the current of the working electrode and adjusting for the collection efficiency (*N*) of the system. This is shown in Equation 4–7, where i_{ring} is the ring current, i_d is the current at the disk electrode, and *N* is the collection efficiency, a measure of how much of the product of oxidation at the disk electrode is subsequently reduced at the ring electrode. The collection efficiency of the system used was determined by reduction of potassium ferricyanide, $K_3Fe(CN)_6$ at the working electrode and its subsequent oxidation at the ring. The collection efficiency was determined to be 23.4% in 1 M NaOH. This value closely matches the geometric collection efficiency for this system, which is 25.6%.

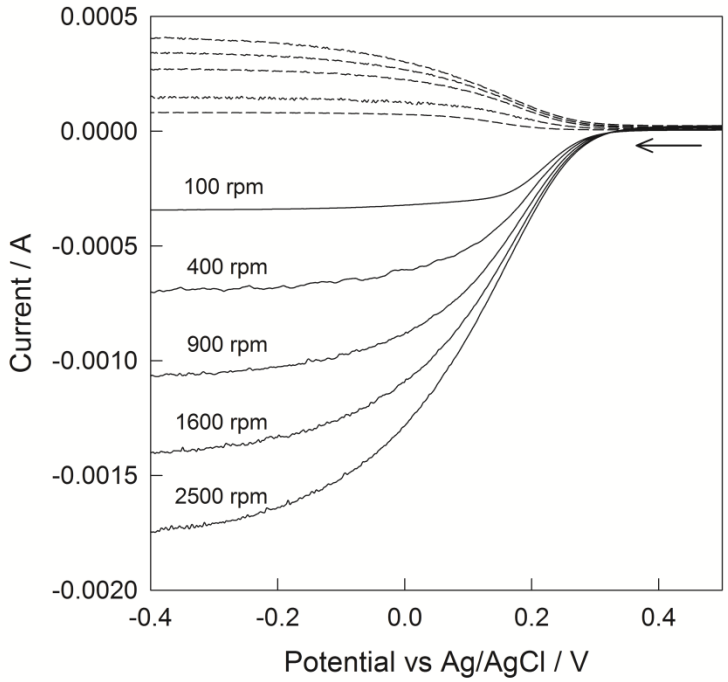

Figure 4-5. Rotating ring-disk scans of $K_3Fe(CN)_6$ at various rotation rates for determination of collection efficiency. Conditions: 10 mM $K_3Fe(CN)_6$, 1 M NaOH, ring potential set to 0.525 V versus Ag/AgCl.

In the coulometric study, the disk potential was set to 0 V for ten minutes, with the ring current set to -0.75 V in order to determine the background current for the ring. The potential of the working electrode was then set to 0.55 V versus Ag/AgCl for 30 minutes (Figure 4-6), with the ring held at -0.75 V. The working electrode potential gives a current density of about 1 mA cm^{-2}, and was chosen because the current at the ring electrode when the disk is set to 0.6 V was too noisy to get reliable data, most likely due to bubble formation at the disk. The average disk current was 1.74×10^{-4} A and the ring current was 1.64×10^{-5} A above the background current. Using Equation 7 and 23.4% for the collection efficiency, the Faradaic efficiency was determined to be 82%. An 82%

Faradaic efficiency is fair for a heterogeneous system; however, the metal oxides tested by McCrory, Peters and Jaramillo all displayed Faradaic efficiencies of greater than 90%.

$$\mathrm{FE} = \frac{2\mathrm{i}_{\mathrm{ring}}}{\mathrm{i}_{\mathrm{d}} N} \tag{7}$$

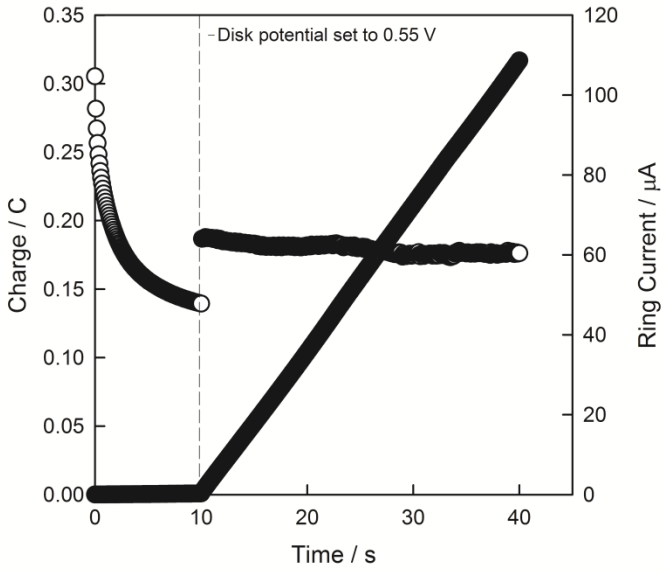

Figure 4-6. Coulometric study of **1a**-activated electrode at 0.55 V versus Ag/AgCl. Conditions: 1 M NaOH, 5×10^{-4} M **1a**, -0.75 V ring potential, 25 °C.

The stability of the TAML-activated electrode was tested by performing coulometry at 0.55 V versus Ag/AgCl in a fresh 1 M NaOH solution with no added catalyst. After 30 minutes, the catalytic efficiency was about 79% that of the system with 5×10^{-4} M **1a** in solution (Figure 4-7). The slope of charge over time continued at the same rate for two hours. This provides further evidence for the ability of **1a** to catalyze the oxidation of water to dioxygen both heterogeneously and homogeneously.

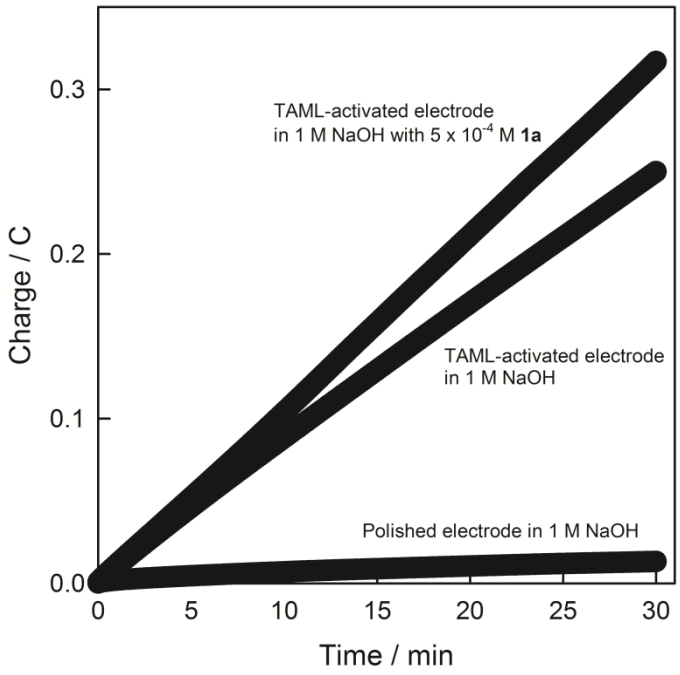

Figure 4-7. Coulometric traces of TAML-activated electrode with and without **1a** in solution. Conditions: 1 M NaOH, glassy carbon electrode held at 0.55 V vs Ag/AgCl, 1600 rpm rotation rate.

4.2.4.3 Characterization of the Activated Working Electrode

The characterization of the TAML-activated electrode was especially interesting due to its high efficiency for heterogeneous oxygen evolution from water, under alkaline conditions. The true nature of the catalytic species on the electrode remains to be determined. Of especial interest is whether **1a** is reversibly or irreversibly binding to the glassy carbon electrode unchanged, releasing iron at the electrode surface to form an iron-based catalyst, or merely oxidizing the electrode and making it more effective. We consider it unlikely that non-TAML iron compounds are acting as the active site for heterogeneous catalysis for the following reasons. First, the electrode surface itself still

appears freshly polished after activation, with no visible deposit. Second, researchers seeking to electrodeposit iron onto working electrodes, such as glassy carbon and indium-tin oxide, avoid iron(III) and alkaline conditions based on the tendency for iron(III)hydroxide to precipitate out. Finally, there is the high activity of the electrode surface. For example, Singh and coworkers have reported an electrodeposited iron oxyhydroxide film on indium-tin oxide electrodes that achieved a current density of 10 mA cm^2 at 495 mV in 1 M NaOH.[36] This film was electrodeposited from acetonitrile in two minutes. In order to probe the nature of the TAML-activated electrode, several studies were conducted.

First, the electrochemically active surface area (ECSA) of the TAML-activated electrode was calculated by measuring the non-Faradaic currents at different scan rates in 1 M NaOH with no added catalyst (Figure 6). The ECSA is determined by dividing the calculated double-layer capacitance (C_{DL}) by the capacitance of an atomically smooth electrode under the same conditions (C_S) (Equation 4–8).[35]

$$i_C = \nu C_{DL} \qquad (4-8)$$

The value was calculated from the voltammograms seen in Figure 4-8, and by plotting the nonFaradaic current at -0.05 V, the C_{DL} was calculated to be 0.0531 ± 0.0001 mF, which gives an ECSA of 1.33 ± 0.03 cm^2. By dividing the ECSA by the geometric surface area (0.196 cm^2), the roughness factor (RF) is obtained, which was found to be 6.8. This RF is quite low, in fact it is lower than the RF reported by McCrory, Peters and Jaramillo for the glassy-carbon electrode with no catalyst present. This should indicate that the surface area of the electrode is approximately the same before and after activation, meaning that no large clusters of particles have been formed.

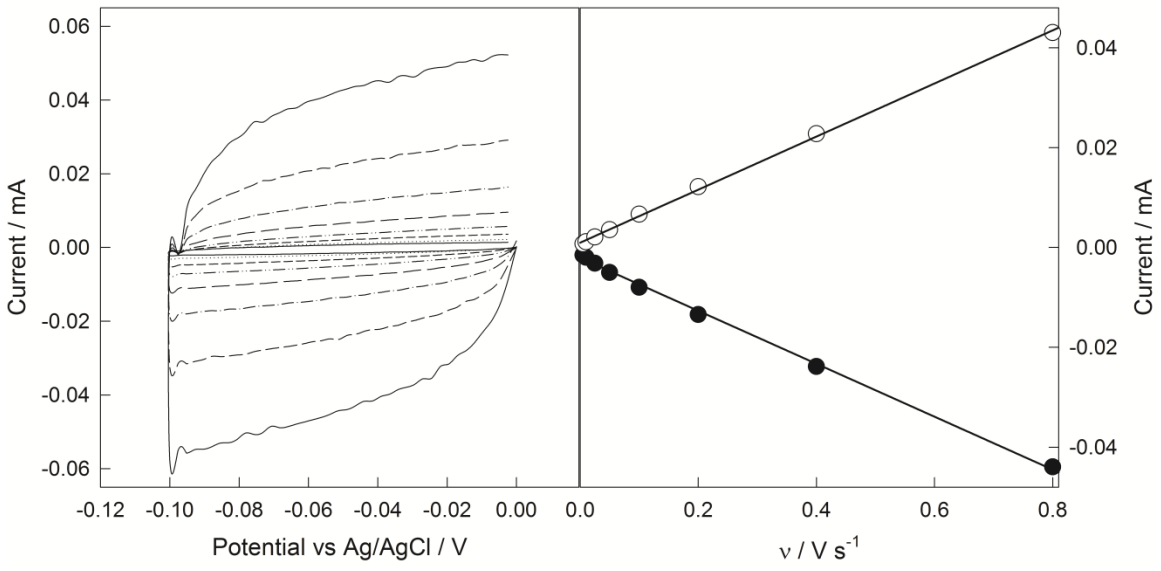

Figure 4-8. Determination of the double-layer capacitance of the **1a**-activated electrode Conditions: **1a**-activated electrode in 1 M NaOH, 5, 10, 25, 50, 100, 200, 400, 800 mV s^{-1} scan rates. Scans were from 0 to -0.1 V, with the potential held at the vertex for 10 s.

4.3 Conclusion

TAML activator **1a** has been found to be among the most active iron-based homogeneous water oxidation catalysts under any conditions. Moreover, **1a** is stable in water with no cosolvent and is highly efficient under alkaline conditions. The TOF value of 1000 s^{-1} compares favorably to the highest reported iron based water oxidation catalyst, which not stable in pure water, which has a TOF of 1900 s^{-1}.

In addition to the high homogeneous electrocatalytic activity **1a** activates the glassy carbon through a simple electrodeposition process to produce an electrode with heterogeneous electrocatalytic behavior that is comparable to several metal oxides in terms of overpotential and stability. The potential required to produce 1.96 mA or a

current density of 10 mA cm^{-2} is 0.6 V versus Ag/AgCl, or an overpotential of only 400 mV.

4.5 References

1. Field, C. B.; Barros, V. R.; Dokken, D. J.; Mach, K. J.; Mastrandrea, M. D.; Bilir, T. E.; Chatterjee, M.; Ebi, K. L.; Estrada, Y. O.; Genova, R. C.; Girma, B.; Kissel, E. S.; Levy, A. .; MacCracken, S.; Mastrandrea, P. R.; White, L. L. IPCC, 2014: Summary for Policymakers, *Climate Change 2014: Impacts, Adaptation, and Vulnerability. Part A: Global and Sectoral Aspects. Contribution of Working Group II to the Fifth Assessment Report of the Intergovernmental Panel on Climate Change*; Cambridge University Press: Cambridge, United Kingdom and New York, NY, USA, **2014**.

2. Hansen, J.; Sato, M.; Hearty, P.; Ruedy, R.; Kelley, M.; Masson-Delmotte, V.; Russell, G.; Tselioudis, G.; Cao, J.; Rignot, E.; Velicogna, I.; Tormey, B.; Donovan, B.; Kandiano, E.; Von Schuckmann, K.; Kharecha, P.; Legrande, A. N.; Bauer, M. *Atmos. Chem. Phys.* **2016**, *16*, 3761–3812.

3. Schulte, D. M.; Dridge, K. M.; Hudgins, M. H. *Sci. Rep.* **2015**, *5*, 17890.

4. Ainsworth, T. D.; Heron, S. F.; Ortiz, J. C.; Mumby, P. J.; Grech, A.; Ogawa, D.; Eakin, C. M.; Leggat, W. *Science* **2016**, *352*, 338–342.

5. Nejat, P.; Jomehzadeh, F.; Taheri, M. M.; Gohari, M.; Abd. Majid, M. Z. *Renew. Sustain. Energy Rev.* **2015**, *43*, 843–862.

6. McDaniel, N. D.; Bernhard, S. *Dalton Trans.* **2010**, *39*, 10021–10030.

7. Cline, E. D.; Adamson, S. E.; Bernhard, S. *Inorg. Chem.* **2008**, *47*, 10378–10388.

8. Gersten, S. W.; Samuels, G. J.; Meyer, T. J. *J. Am. Chem. Soc.* **1982**, *104*, 4029–4030.

9. Sens, C.; Romero, I.; Rodriguez, M.; Llobet, A.; Parella, T.; Benet-Buchholz, J. *J. Am. Chem. Soc.* **2004**, *126*, 7798–7799.

10. Kärkäs, M. D.; Verho, O.; Johnston, E. V.; Åkermark, B. *Chem. Rev.* **2014**, *114*, 11863–12001.

11. Kaveevivitchai, N.; Zong, R.; Tseng, H.-W.; Chitta, R.; Thummel, R. P. *Inorg. Chem.* **2012**, *51*, 2930–2939.

12. Bernet, L.; Lalrempuia, R.; Ghattas, W.; Mueller-Bunz, H.; Vigara, L.; Llobet, A.; Albrecht, M. *Chem. Commun.* **2011**, *47*, 8058–8060.

13. Duan, L.; Bozoglian, F.; Mandal, S.; Stewart, B.; Privalov, T.; Llobet, A.; Sun, L. *Nat. Chem.* **2012**, *4*, 418–423.

14. McDaniel, N. D.; Coughlin, F. J.; Tinker, L. L.; Bernhard, S. *J. Am. Chem. Soc.* **2008**, *130*, 210–217.

15. Blakemore, J. D.; Schley, N. D.; Balcells, D.; Hull, J. F.; Olack, G. W.; Incarvito, C. D.; Eisenstein, O.; Brudvig, G. W.; Crabtree, R. H. *J. Am. Chem. Soc.* **2010**, *132*, 16017–16029.

16. Lalrempuia, R.; McDaniel, N. D.; Mueller-Bunz, H.; Bernhard, S.; Albrecht, M. *Angew. Chemie, Int. Ed.* **2010**, *49*, 9765–9768.

17. Petronilho, A.; Rahman, M.; Woods, J. A.; Al-Sayyed, H.; Mueller-Bunz, H.; Don MacElroy, J. M.; Bernhard, S.; Albrecht, M. *Dalt. Trans.* **2012**, *41*, 13074–13080.

18. Gao, Y.; Crabtree, R. H.; Brudvig, G. W. *Inorg. Chem.* **2012**, *51*, 4043–4050.

19. Poulsen, A. K.; Rompel, A.; McKenzie, C. J. *Angew. Chemie, Int. Ed.* **2005**, *44*, 6916–6920.

20. Young, K. J.; Takase, M. K.; Brudvig, G. W. *Inorg. Chem.* **2013**, *52*, 7615–7622.

21. Wasylenko, D. J.; Palmer, R. D.; Schott, E.; Berlinguette, C. P. *Chem. Commun.* **2012**, *48*, 2107–2109.

22. Nakazono, T.; Parent, A. R.; Sakai, K. *Chem. Commun.* **2013**, *49*, 6325–6327.

23. Rigsby, M. L.; Mandal, S.; Nam, W.; Spencer, L. C.; Llobet, A.; Stahl, S. S. *Chem. Sci.* **2012**, *3*, 3058–3062.

24. Zhang, T.; Wang, C.; Liu, S.; Wang, J.-L.; Lin, W. *J. Am. Chem. Soc.* **2014**, *136*, 273–281.

25. Barnett, S. M.; Goldberg, K. I.; Mayer, J. M. *Nat. Chem.* **2012**, *4*, 498–502.

26. Zhang, M.-T.; Chen, Z.; Kang, P.; Meyer, T. J. *J. Am. Chem. Soc.* **2013**, *135*, 2048–2051.

27. Ellis, W. C.; McDaniel, N. D.; Bernhard, S.; Collins, T. J. *J. Am. Chem. Soc.* **2010**, *132*, 10990–10991.

28. Coggins, M. K.; Zhang, M. T.; Vannucci, A. K.; Dares, C. J.; Meyer, T. J. *J. Am. Chem. Soc.* **2014**, *136*, 5531–5534.

29. Fillol, J. L.; Codola, Z.; Garcia-Bosch, I.; Gomez, L.; Pla, J. J.; Costas, M. *Nat. Chem.* **2011**, *3*, 807–813.

30. Panda, C.; Debgupta, J.; Díaz, D. D.; Singh, K. K.; Gupta, S. Sen; Dhar, B. B.; Díaz Díaz, D.; Singh, K. K.; Sen Gupta, S.; Dhar, B. B. *J. Am. Chem. Soc.* **2014**, *136*, 12273–12282.

31. Okamura, M.; Kondo, M.; Kuga, R.; Kurashige, Y.; Yanai, T.; Hayami, S.; Praneeth, V. K.; Yoshida, M.; Yoneda, K.; Kawata, S.; Masaoka, S. *Nature* **2016**, *530*, 465–468.

32. Demeter, E. L.; Hilburg, S. L.; Washburn, N. R.; Collins, T. J.; Kitchin, J. R. *J. Am. Chem. Soc.* **2014**, *136*, 5603–5606.

33. Popescu, D. L.; Vrabel, M.; Brausam, A.; Madsen, P.; Lente, G.; Fábián, I.; Ryabov, A. D.; Van Eldik, R.; Collins, T. J. *Inorg. Chem.* **2010**, *49*, 11439–11448.

34. Savéant, J.-M. *Chem. Rev.* **2008**, *108*, 2348–2378.

35. McCrory, C. C. L.; Jung, S.; Peters, J. C.; Jaramillo, T. F. *J. Am. Chem. Soc.* **2013**, *135*, 16977–16987.

36. Chowdhury, D. R.; Spiccia, L.; Amritphale, S. S.; Paul, A.; Singh, A. *J. Mater. Chem. A* **2016**, *4*, 3655–3660.

Chapter 5

Removal of Ecotoxicity of 17α-Ethinylestradiol Using TAML/Peroxide Water Treatment

5.1 Introduction

Water is one of the most valuable natural resources. Access to clean water is imperative for healthy individuals and communities. According to the U.S. Geological Survey, 86 % of Americans get water from public supply and 63 % of that comes from surface water.[1] Unfortunately, surface water receives effluent from municipal wastewater treatment, which can contain micropollutants such as pharmaceuticals, detergent metabolites and plasticizers that persist through the treatment process.[2,3] Numerous communities with limited water supplies even use treated wastewater as a source of drinking water. Examples of large urban centers that indirectly use treated wastewater as a source of drinking water are Orange County, California with the Groundwater Replenishment System (GWRS), Singapore with the Newater system and London, U.K., which is downstream of several urban centers that discharge wastewater into the River Thames. All three of these communities have treated wastewater entering sources of drinking water. This situation is amplified in the U.K. because, depending on the season, the effluent from a wastewater treatment plant can be up to 100% of the volume of the receiving water.[4] This results in the accumulation a number of persistent micropollutants in streams that receive wastewater effluent, which can harm aquatic wildlife. Effective secondary and tertiary treatment methods necessary to remove these compounds require high capital investment and operating cost.[3] In light of this, there is a need for an inexpensive, highly effective removal technology that is easy to implement given current infrastructural limitations.

One of the more notable effects of micropollutants entering the environment is the effect of fish feminization. Worldwide, male fish are being discovered that exhibit female

characteristics.[4,5] Male fish begin to grow oocytes in the testes and to produce vitellogenin, a protein found in egg yolk and only secreted by females in normal populations. This condition is referred to as intersex, and can ultimately lead to the collapse of fish populations in bodies of water with high levels of estrogenic compounds.[6]

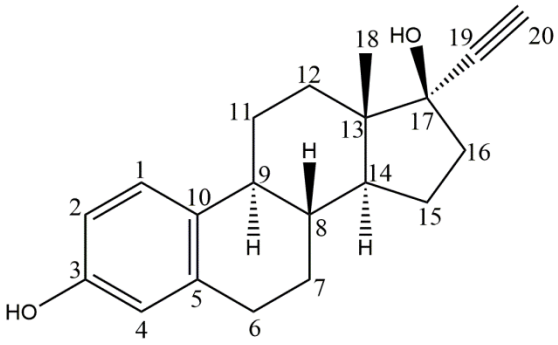

Figure 5-1. 17α-ethinylestradiol with numbered carbon atoms

17α-ethinylestradiol (EE2), one of the principal active ingredients in oral contraceptives (the birth control pill), is a pharmaceutical commonly found in wastewater.[2] It varies from natural estrogen, estradiol (E2), in having an acetylene unit at C17 (Figure 5-1), which makes it less susceptible to oxidative degradation through biological processes with rates of 2-hydroxylation by P450 enzymes in the liver decreasing from 12 to over 100% relative to estradiol.[7] Oral contraceptives, which are over 99% effective at preventing pregnancy when taken properly, typically contain twenty to thirty micrograms of EE2. Because of its resistance to biological degradation, women taking the birth control pill can excrete up to 10 µg per day of EE2, which can enter the environment through the municipal wastewater system.[8] Another factor in the concern over EE2 is that in most organisms it is a more potent estrogen than naturally

occurring estrogens. It can be ten to one hundred times as potent of an estrogen as E2 in fish, depending on the species.[9] EE2 is so potent that it has been shown to feminize male fish at concentrations as low as 4 parts per trillion (ppt).[10] Conventional wastewater treatment plants (WWTP) are capable of removing EE2 but results vary based on a variety of infrastructural and environmental conditions. The Weisbaden WWTP in Germany was able to decrease the EE2 concentrations in effluent from two ppt in 1997 to non-detectable after increasing their active-sludge holding time from less than four days to twelve days.[11] This is not an option for every WWTP due to the capital cost and space requirements of such a long treatment time. Environmental evidence that EE2 is not being adequately removed from wastewater comes from a 1999-2000 study examining 70 waterways in the United States that found EE2 in 11 samples, with a median level of 73 ppt.[2] EE2 at these levels in environmental waters is of concern not just to wildlife, but also for humans because these are the sources of drinking water for many communities. The human developmental effects of EE2 at low doses are not fully known but it is well established that fetuses, infants and young children are much more susceptible to exogenous hormones, and exposure to these chemicals at certain stages of development can have disastrous effects. Diethylstilbestrol, a non-steroidal artificial estrogen formerly given to pregnant women who were considered high-risk for miscarriage, has been shown to cause increased risk of a number of reproductive system abnormalities in the offspring of women who had taken it.[12] Female greenhouse workers in Denmark who are occupationally exposed to a variety of pesticides, including known endocrine disruptors, were shown to be three times more likely to have a son with one or both undescended testes at three months of age compared to a control group.[13] While undesired exposure to

compounds such as 17α-ethinylestradiol can have negative effects on the environment, their use can contribute positively to the environment and society when applied correctly. Population control is an essential component of long-term sustainability, but damage to aquatic ecosystems stemming from the use of contraceptives may be an unfortunate tradeoff. Due to the potential environmental and public health implications EE2 is gaining increased attention nationally and internationally, with the U.S., U.K. and Europe monitoring and considering regulation of sewage effluents. An effective way of preventing environmental contamination of EE2 without limiting consumer use of this essential compound would be of great benefit.

A potential solution to the problem of ineffective remediation of micropollutants in municipal wastewater treatment is the use of TAML activators with hydrogen peroxide. As discussed throughout this work, these catalysts activated hydrogen peroxide in water to oxidize a wide variety of substrates, including industrial dyes and pharmaceuticals.[14–21] In light of this, TAML/peroxide technology shows great promise in treating municipal and industrial wastewater. If implemented into wastewater treatment, the developing TAML/peroxide technology would require little capital investment. The TAML catalyst and peroxide can be added near the end of the treatment process in a holding tank with minimal additional equipment needed. However, in order to make this technology applicable to wastewater treatment in light of impending regulation, environmentally relevant concentrations of EE2 would have to be destroyed within the limitations of time, space and water conditions (temperature, pH, etc.) permitted at a given treatment plant.

With the increased attention on EE2, it is important that any treatment technology be able to address the life-cycle concerns of treatment. The goal of this research is to study the entire degradation of EE2 with TAML catalysts and hydrogen peroxide. This includes kinetic studies to determine the rates at which TAML activators can degrade 17α-ethinylestradiol under a wide range of conditions, characterization of degradation products, minimization of catalyst and peroxide loading and determination of estrogenicity and toxicity of EE2 containing water treated with TAML/peroxide using biological assays.

5.2 Results and Discussion

5.2.1 Kinetics

Two catalysts were used for the experiments studying the degradation of EE2, **1a** and **1b** (1a: X = H, R = Me; 1B: $X_1 = NO_2$, R = F). As can be seen in Figure 5-2, the oxidation of EE2 is much faster with **1b** than **1a**. In this research, EE2 is consistently degraded by over 98% by both catalysts, however the time needed to reach full degradation ranged from four minutes (pH 9, **1b**) to days (pH 6, **1a**) depending on pH and catalyst used. With **1b** at pH 6, degradation was complete in about three hours, making it as a promising candidate for use in wastewater treatment. After establishing that both **1a** and **1b** were capable of oxidizing EE2 from pH 6-9, remaining studies were conducted at pH 7, which is most relevant to wastewater treatment.

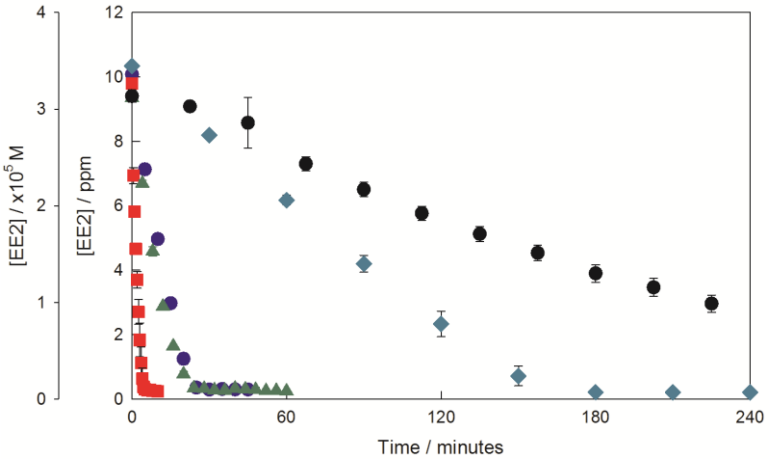

Figure 5-2. Degradation of EE2 with TAML catalysts and peroxide. Conditions: 3.4×10^{-5} M (10 ppm) EE2, 1×10^{-3} M H_2O_2, 0.01 M phosphate buffer and 80 nM catalyst at room temperature. Catalyst and pH: **1b** at pH 9 (red squares), **1a** at pH 9 (green triangles), **1b** at pH 7.5 (blue circles), **1b** at pH 6 (light blue diamonds) and **1a** at pH 7.5 (black circles).

Extensive prior mechanistic work has established that TAML catalysts perform catalytic oxidations through a two-step mechanism as shown in Scheme 5-1 and described in detail in Chapter 1. The degradation of EE2 at pH 7 with hydrogen peroxide catalyzed by **1a** was conducted in order to measure the rate constants k_I and k_{II}, which were found to be 35 M^{-1} s^{-1} and $(8.6 \pm 0.5) \times 10^5$ M^{-1} s^{-1}, respectively (Figure 5-3A).

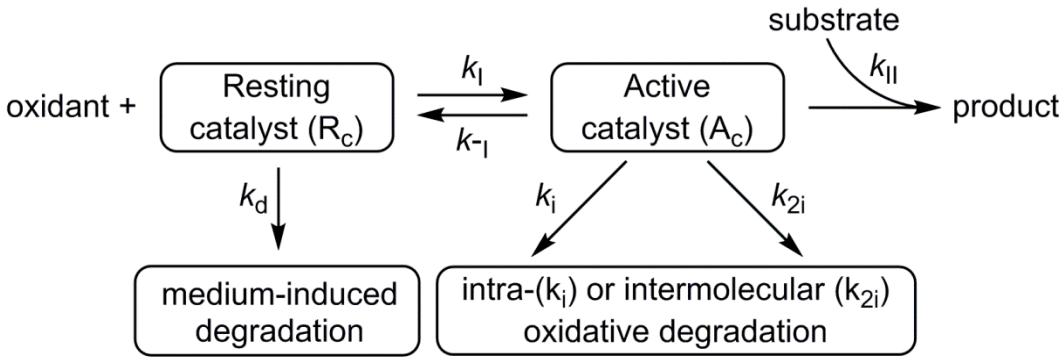

Scheme 5-1. Life-cycle analysis of catalytic oxidation of substrates by TAML catalysts and an oxidant.

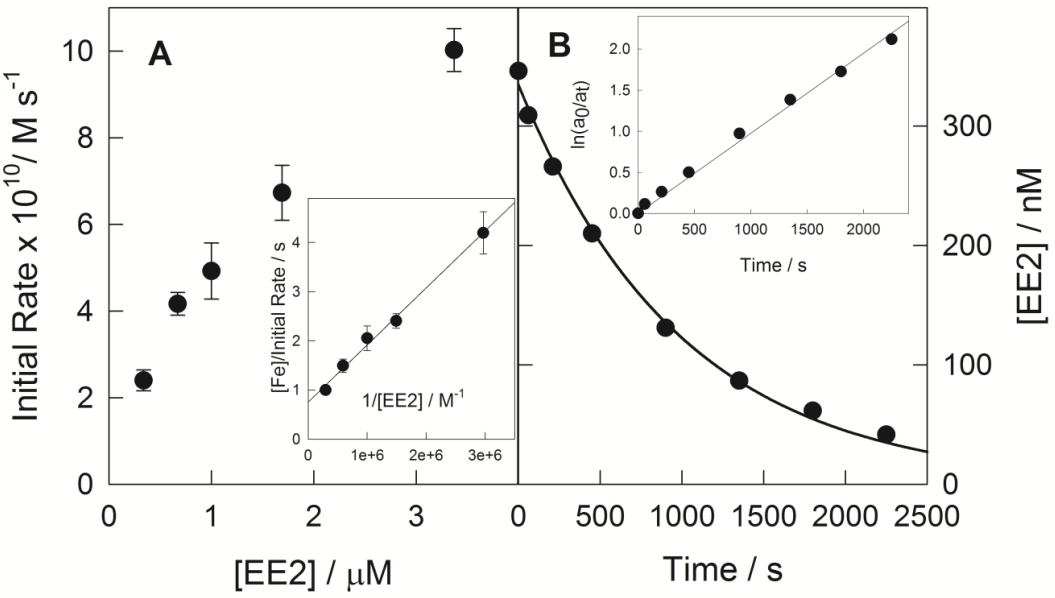

Figure 5-3. Kinetic plots used for determination of rate constant k_{II} for **1a** with EE2. Figure 5-3A shows the hyperbolic dependence of the initial rate on EE2 concentration, and the inset is the linearization of the data using a double inverse plot. Figure 5-3B shows the exponential decay of EE2 at very low EE2 concentration so that $k_I[H_2O_2] >> k_{II}[EE2]$. The inset to 5-3B is the linearization of the data used to obtain k_{II}. Conditions: 1×10^{-9} M **1a**, 0.01 M H_2O_2, 0.01 M phosphate buffer at pH 7, 25 °C.

The value of k_{II} was verified by oxidizing EE2 under conditions where the oxidation of the substrate by the active catalyst would be rate limiting and analyzing the exponential decay curve. From this experiment, the value of k_{II} was determined to be (9.4 ± 0.2) × 10^5, which is in good agreement with the previous value (Figure 5-3B). The value for k_I is consistent with values obtained in the oxidation of other substrates with **1a** so there does not appear to be any inhibition by EE2.[22] The value of 8.6×10^5 M^{-1} s^{-1} is quite high, and comparable to the reactivity of horseradish peroxidase, which was

reported as 2×10^6.[23] In comparison to other oxidative treatments with applicability to wastewater treatment, **1a**/peroxide performs quite well.[24] At the extremely low concentrations of EE2 that are commonly seen in wastewater treatment plants, the oxidation of the substrate by the activated catalyst would be the rate-limiting step. As seen in Figure 5-4, **1a**/peroxide treatment at pH 7 has a second-order rate constant similar to ozone. Compared to ozone, **1a**/peroxide has a lower required capital cost, as no ozone generators need to be built on site. The energy requirements are also lower relative to ozone.

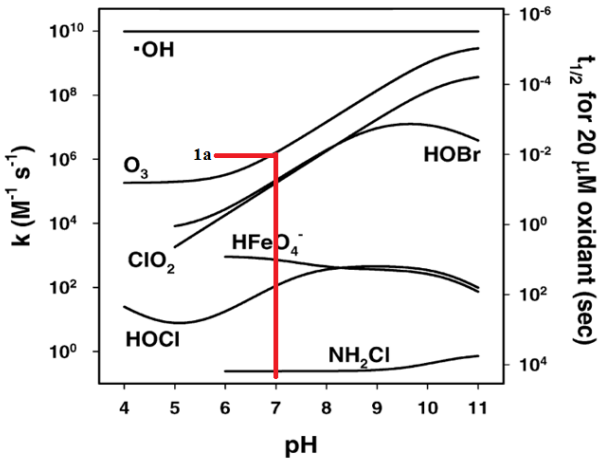

Figure 5-4. Comparison of the rate constant k_{II} for **1a** with EE2 to other oxidative treatments commonly used in wastewater treatment.

5.2.2 Characterization of degradation intermediates

The kinetic data discussed previously was collected by HPLC, and early in this investigation it was observed that two peaks were consistently seen with shorter retention times (3 and 3.5) minutes than EE2 (5.5 minutes). These peaks would increase in size

until EE2 concentration reached a minimum, at which time they too would decrease (Figure 5-5). We concluded that these were potential degradation intermediates, as the UV spectra obtained from the diode array detector were very similar to EE2. As we are concerned with removing all potential toxic effects of the initial compound, efforts were made to isolate and characterize these intermediates.

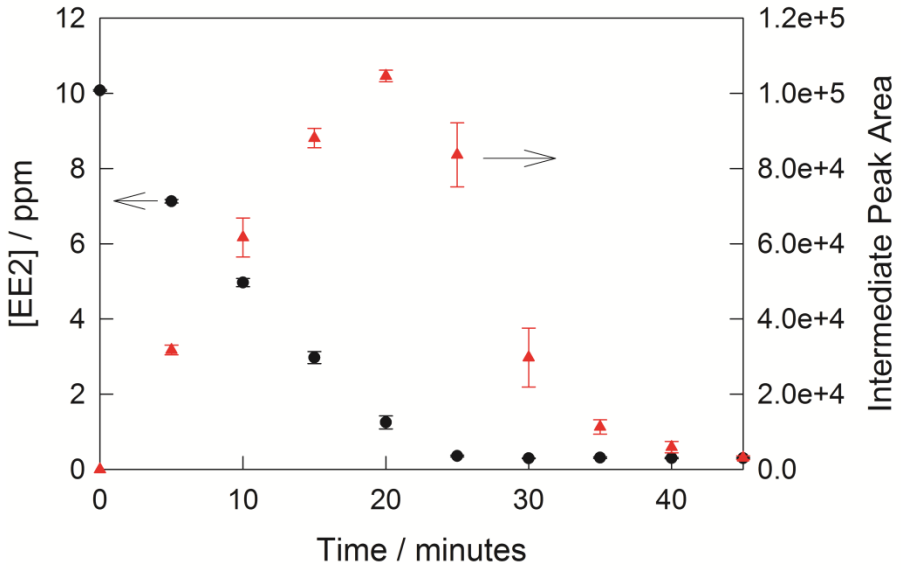

Figure 5-5. Appearance and subsequent disappearance of intermediate peaks that occurs during the degradation of EE2 with TAML catalysts and hydrogen peroxide. Conditions: 3.37×10^{-5} M (10 ppm) EE2, 3.37×10^{-4} M (11.5 ppm) H_2O_2, 80 nM **1b**, 0.01 M phosphate buffer at pH 7.5. The black circles represent the decay of EE2 and the red triangles represent the formation and subsequent decay of three early degradation intermediates.

The characterization of these intermediate species presented a significant challenge due to the extremely low solubility of EE2 in water of just over 10 mg/L. In order to capture these intermediates, reactions were scaled up to one liter and quenched

with catalase when intermediates were at the maximum concentration. The reaction mixture was then concentrated using solid phase extraction and isolated using preparative HPLC. Negative mode ESI-MS showed mass peaks of 293 (EE2 - H_2, -H) and 311 (EE2 + O, - H), corresponding to loss of H_2 and addition of an oxygen atom respectively. It was deemed most probable that the first step involved the oxidative loss of H_2 from EE2 to form alkenes. NMR spectra of the unknown compounds revealed that there were actually four compounds in the two isolated fractions, with all four compounds being present in different ratios in both fractions.

Based on the mass data, thorough 1D and 2D NMR analyses were conducted looking for possible dehydrogenated or oxygenated derivatives of EE2 (Figure 5-6). The presence of species **I1**, with the alkene between carbons 9 and 11 was confirmed through NMR analysis with a sample ordered from Dalton Pharma Services (Toronto, ON). Other likely products from benzylic dehydrogenation[25] were found not to be present. Further analysis of the ^{1}H and ^{13}C and 2D NMR spectra indicated a high probability that **I2**, **I3** and **I4** comprise the remaining members of the product mixture. A possible explanation for the HPLC and NMR data is that an initial oxidation intermediate forms which adds H_2O under the catalytic conditions to give the multiple observed alcohol oxidation products. Compound **I5** is primed for such water additions under catalytic conditions. An analogous product of electrochemical oxidation of E2 has been proposed.[26]

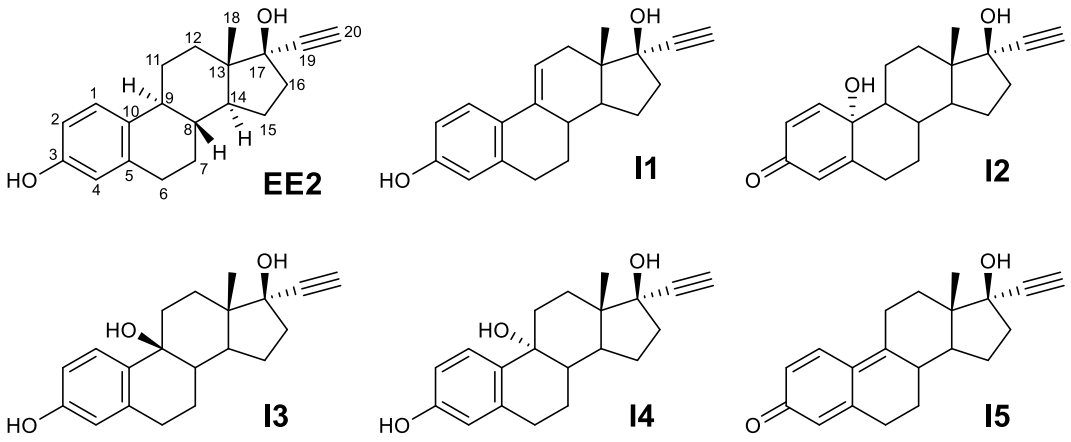

Figure 5-6. Characterized intermediates from the TAML-catalyzed oxidation of EE2.

In order to rationalize the seemingly contradictory NMR and HPLC data, an experiment was run using 0.05% phosphoric acid instead of pure water in the HPLC mobile phase. Degradation samples run under these conditions showed that the previous two peaks coalesced into one peak with a retention time that was intermediate between the original two peaks. Running isolated samples of the two peaks using the same mobile phase had the same effect. This further supports the idea of interconversion between **I1**, **I2**, **I3** and **I4**.

5.2.3 Determination of the Effect of TAML/Peroxide Treatment on Sample Estrogenicity

After showing that TAML/peroxide treatment could effectively eliminate measurable traces of EE2 and the initial oxidized products, our efforts moved toward assessing the ability of this system to mitigate the residual estrogenicity of treated samples. A series of biological assays were conducted at Brunel University in collaboration with the Institute

for the Environment. The first assay was the yeast estrogen screen (YES).[27] One liter samples of two ppt EE2 solutions were prepared either buffered or unbuffered. To these bottles were added an appropriate amount of TAML to give 80 nM catalyst (either **1a** or **1b**) and reactions were initiated with an appropriate amount of H_2O_2 stock solution to give an initial [H_2O_2] of 4.7×10^{-6}, 4.7×10^{-5} or 4.7×10^{-4} M (0.16, 1.60 and 16.0 ppb, respectively). After 45 minutes the reactions were quenched with catalase, concentrated with solid phase extraction, and eluted with ethanol. The ethanol was then concentrated to yield a final volume of one mL containing the organic compounds. Only the unbuffered sample containing **1a** and the lowest concentration of peroxide showed any level of estrogenicity according to the YES assay (Figure 5-7). This corroborates studies performed at higher concentration and demonstrates that TAML/peroxide treatment is an effective treatment for reducing both the measureable amount of EE2 in laboratory samples, as well as reducing the estrogenic effects that stem from it.

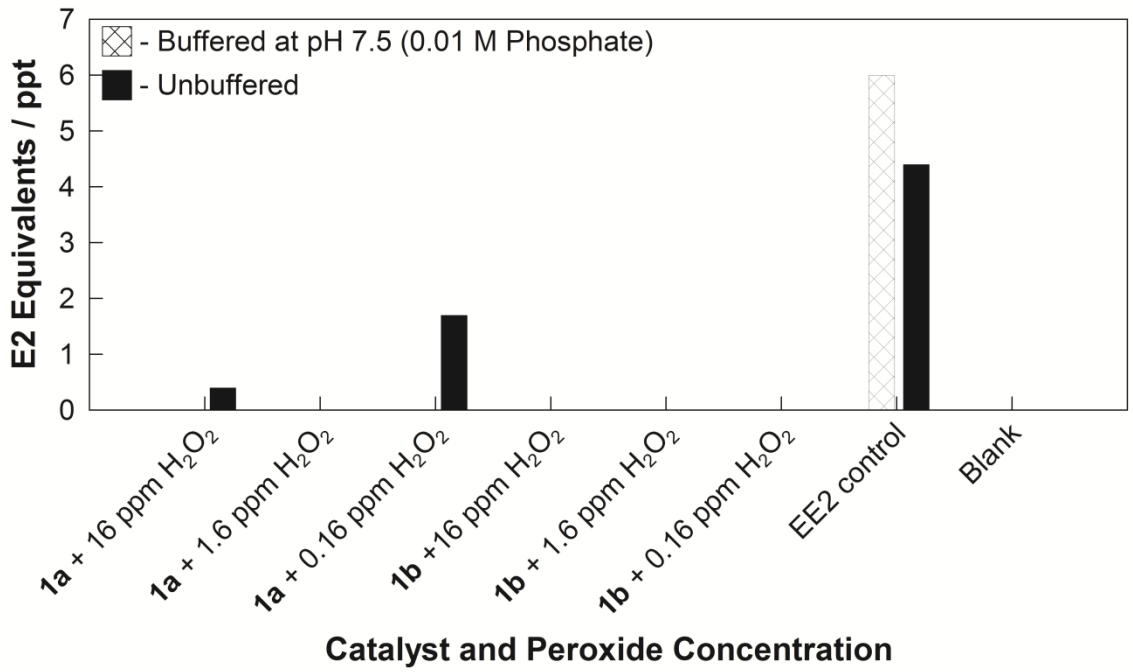

Figure 5-7. Reduction of estrogenicity of TAML/peroxide-treated samples of EE2 according to the yeast estrogen screen. Conditions: 8×10^{-8} M **1a** or **1b**, 2 ppt (6.7×10^{-12} M) EE2, 0.01 M phosphate buffer (gray bars) or unbuffered, room temperature. The estrogenicity is reported as E2 equivalents, and according to this screen, EE2 is three times as estrogenic as E2, which is why the EE2 standards are near six ppt instead of two ppt.

Studies were next conducted with fathead minnows under conditions which would simulate a small watercourse that receives a substantial portion of its volume from wastewater treatment effluent. Laboratory water was spiked with two ppt EE2 and treated for 45 minutes with 80 nM **1b** and 0.16 ppm (4.7 μM) H_2O_2 before being allowed to flow into tanks containing adult male fathead minnows. This was done in a continuous manner and the fish were exposed for a total of 21 days. During this time samples of the water in the treated tanks show an average concentration of 0.6 ppt (Figure 5-8, left axis), which is

approximately a 90% removal rate. Because EE2 is such a potent estrogen, this 10-fold decrease in the concentration correlated to a 100-fold decrease in the amount of vitellogenin produced by the fish in the treated tanks (Figure 5-8, right axis). As vitellogenin production in male fish is a sensitive indicator of sexual health, this 100-fold reduction in the treated samples is quite significant from an environmental health perspective. It also illustrates the importance of studying treatment options with a variety of methods, as endocrine disrupting compounds do not usually display simple monotonic dose-response curves in their effects on exposed organisms.

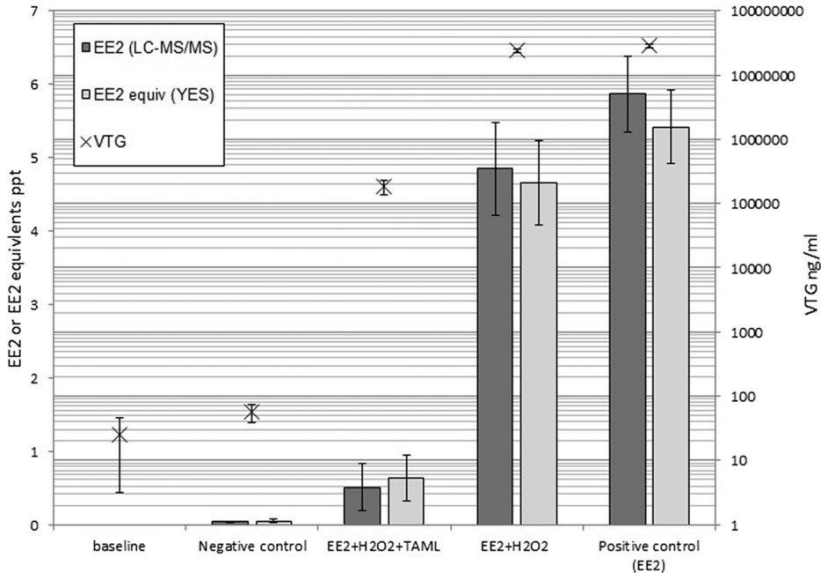

Figure 5-8. Average EE2 concentration and estrogenic activity in treated and untreated waters with plasma vitellogenin in male fish exposed to the treatments for 21 days. EE2 concentration (ng/l, ppt; dark grey bar, 1st Y-axis) was measured by LC-MS/MS, estrogenic activity (EE2 equivalent ng/l, ppt; light grey bar, 1st Y-axis) was measured via in vitro Yeast Estrogen Screen (YES). Plasma vitellogenin (ng/ ml or ppb; grey cross X, 2nd Y-axis log scale) concentration in male fathead minnows were measured via a quantitative enzyme-linked immunosorbent assay (ELISA). EE2 chemical analysis results reported as < 0.03 ppt EE2 (i.e. lower than detection limit (LOD)) were treated as having half LOD (i.e. 0.015 ppt EE2) for use in calculations of averages, standard error and statistical analysis. EE2 and estrogenic activity are average measured concentrations sampled over the 21 day exposure. Plasma VTG was measured prior to exposure (baseline) and after 21 days exposure. The treatment regime consisted of; Control (water only), **1b**/ H_2O_2 + EE2, H_2O_2 + EE2, and EE2-only. All error bars represent standard error of the mean in all cases.

5.2.4 Determination of the Effectiveness of TAML/Peroxide Treatment in Municipal Wastewater Effluent

The previously described studies have shown that TAML/peroxide treatment is an effective method for both decreasing the concentration of EE2 in treated water, with a rate of reaction comparable to ozone, and in mitigating the estrogenicity of these samples. In order for this technology to be widely applied, it needs to display the same performance in municipal effluent, where there are other oxidizable species in solution. In order to determine this, Dr. Rakesh Kanda, who worked for United Kingdom Water Industry Research Limited (UKWIR), performed studies Activated Sludge Process (ASP) effluent from a number of wastewater treatment plants in the UK. The treatment conditions used 40 nM **1a**, 10-150 ppm ($2.94 \times 10^{-4} - 4.41 \times 10^{-3}$ M) H_2O_2, pH 7-9, and 15-45 minutes of treatment time (Figure 5-9). Removal efficiencies above 90% were obtained in a number of tests, however under the mildest conditions, pH 7 with 10 ppm H_2O_2 and 15 minutes of treatment, removal was at about 22%. Doubling the peroxide concentration to 20 ppm increased the removal efficiency to 65% in the same amount of time.

The ability of TAML/peroxide treatment effectively remove EE2 from municipal wastewater effluent is incredibly important. This shows that the catalysts themselves are quite robust. It also demonstrates that with an extremely low catalyst loading of 40 nM, high catalytic performance remains.

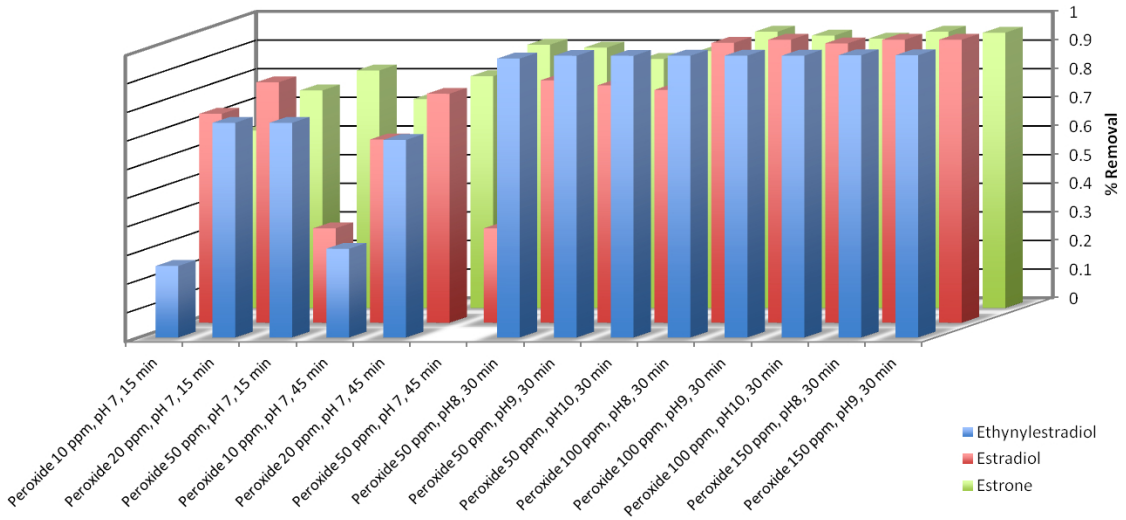

Figure 5-9. EE2 in ASP effluent using **1a** under varying conditions. Conditions: 40 nM **1a**, 25 °C.

5.3 Conclusions

This work shows that TAML/peroxide treatment is highly effective for the removal of EE2 from spiked laboratory samples, the mitigation of residual estrogenicity, and maintains this effectiveness in ASP effluent. The second-order rate constant for the oxidation of EE2 with the activated catalyst is comparable to ozone at pH 7, and significantly high than for other oxidative treatments such as hypochlorite and ferrate. During the course of oxidation, intermediates are formed which maintain some level of estrogenicity. However biological assays show that the estrogenic effects after treatment are greatly reduced. Treatment of municipal and industrial wastewater with TAML/peroxide is a high-performance technique that can be implemented with little capital costs. This work also highlights the importance of collaboration with researchers

across disciplines and sectors. As chemists, we would not have been able to show the disproportionate decrease of estrogenicity of treated water toward fathead minnows. Additionally, without our collaborators at UKWIR, we would not have known whether TAML/peroxide is a viable treatment for wastewater effluent.

5.4 Experimental Section

5.4.1 Materials

All solvents were HPLC-grade unless otherwise stated. Analytical-grade EE2 and catalase (from *Aspergillus niger*, 2350 U mg^{-1}) were obtained from Sigma-Aldrich. Hydrogen peroxide (30% w/w) was purchased from Fluka. The $-H_2$ EE2 derivatives **3**, **4** and **5** were purchased from Dalton Pharma Services (Toronto, ON). All other reagents and solvents (at least ACS reagent grade) were obtained from commercial sources (Aldrich, Fisher, Acros, and Fluka). TAML activator **1a** was obtained from ChemPacific and **1b** was obtained from GreenOx Catalysts (Pittsburgh, PA). Hydrogen peroxide stock solutions were standardized daily spectrophotometrically ($\varepsilon = 72.4\ M^{-1}\ cm^{-1}$).[23] Phosphate buffer (0.01 M) was used as the reaction medium. The pH of each reaction mixture was adjusted by addition of potassium hydroxide or phosphoric acid solutions. Stock solutions of EE2 were prepared in methanol or ethanol (no effect from the alcohol was observed in the degradation pathway or rate) and were stored under refrigeration. Stock solution of **1a** and **1b** were prepared in methanol and were stored under refrigeration. Stock solutions of catalase (~23,500 U mL^{-1}), used to quench the reactions by decomposing excess H_2O_2, were prepared in water and stored under refrigeration for a maximum of one week before disposal.

5.4.2 Instrumentation and Analysis

A Shimadzu HPLC system [Shimadzu CMB-20A controller, LC-20AB pump, DGU-20A$_3$ degasser, SPD-M20A diode array detector, RF-20A XS fluorimeter detector, CTO-20A column oven, and SIL-20A HT auto sampler] was used for monitoring the oxidative degradation of EE2. Chromatographic separation of EE2 and its degradation intermediates was achieved using an Agilent Microsorb-MV 100-5 C18 (250 mm x 4.6 mm, 5 µm particle size) column. HPLC analysis conditions were: 25-uL injection volume, 40 ˚C column temperature, and isocratic elution using 40% acetonitrile and 60% water at 1 mL min^{-1} flow rate. The HPLC diode array detector was set to a 200 – 450 nm range and the fluorimeter detector was set to λ_{ex} = 220 and λ_{em} = 305 nm. The retention times of EE2 and its estrogenic degradation intermediates under these conditions were, respectively, 5.2, 3.0, and 3.4 minutes. ESI-MS analyses were performed using a Finnigan LCQ MS ion trap with ESI detection. A Bruker 500 MHz NMR instrument was used for ^{1}H and ^{13}C NMR studies (1D and 2D) at 300 K. The pH measurements were acquired with a Corning 220 pH meter calibrated with standard buffer solutions at pH 4, 7, and 10.

5.4.3 Degradation Comparison at Varying pH

A volume of methanolic EE2 stock solution was added to an aqueous solution of phosphate buffer (0.01 M) at the desired pH (pH 6.0, 7.5, and 9.0) and was sonicated at 40 ˚C for 20 minutes to ensure a homogenous solution, then cooled to room temperature. To this solution, a volume of catalyst stock (**1a** or **1b)** solution was added to achieve a concentration of 80 nM. An aliquot of the reaction mixture was analyzed by HPLC to

measure the initial concentration. To the remaining reaction mixture, a volume of H_2O_2 was added to initiate the reaction. The concentration of EE2 was monitored by HPLC various time intervals (e.g. pH 7.5 - Figure 1), either by direct injection of the reaction mixture into the instrument (**1a**, pH 6 and 7.5), or by quenching 1 mL aliquots with 10 μL of catalase solution in an HPLC vial. The concentrations of each component in the reaction mixture are as follows: 33.7 μM (10.0 ppm) EE2, 80.0 nM (0.04 ppm) **1a** or **1b**, 337.4 μM (11.48 ppm) H_2O_2.

5.4.4 Determination of k_{II} at pH 7

The second-order rate constant k_{II} was determined by measuring the initial rate of degradation at varying concentrations of EE2. The concentration at given time points was determined by HPLC analysis as described in section 2.4.3. The data was then plotted in a modified Lineweaver-Burke plot to linearize the data, with the slope of the line being equal to $1/k_{II}$. The value of k_{II} determined in this manner was $(8.6 \pm 0.5) \times 10^5$ M^{-1} s^{-1}. To verify this value, EE2 was subjected to catalyzed degradation under conditions in which k_{II} would be rate-limiting ($k_I[H_2O_2] >> k_{II}[EE2]$). This resulted in an exponential decay curve for EE2 which was linearized by plotting $\ln(a_0/a_t)$ versus time (Figure 5-3B). The slope of the line is equal to k_{II}[**1a**]. This resulted in value for k_{II} of $(9.4 \pm 0.2) \times 10^5$ M^{-1} s^{-1}, which is within error of the previously calculated value.

5.4.5 Degradation of EE2 to Isolate Reaction Intermediates

An appropriate volume of EE2 stock solution was added to a 1L aqueous solution of pH 9.0 phosphate buffer (0.01 M) and was sonicated at 40 °C for 20 minutes to ensure a homogenous solution, then cooled to room temperature. To this solution, an appropriate

volume of **1a** stock solution was added. Degradation was then initiated by addition of an appropriate volume of H_2O_2 stock solution. At the experimentally determined time of maximum intermediate concentration, 1 mL of catalase was added to quench the remaining H_2O_2 in the reaction mixture. The concentrations of each component in the reaction mixture are as follows: 33.7 µM (10.00 ppm) EE2, 80.0 nM (0.04 ppm) **1a**, 337.4 µM (11.48 ppm) H_2O_2. This sample was concentrated using solid phase extraction (Phenomenex Strata-X, 12 mL Gigatubes with 1g sorbent). The SPE cartridges were eluted with acetonitrile and concentrated to 500 µL for purification with preparative HPLC.

5.4.6 Degradation of EE2 for Yeast Estrogen Screen (YES) assays

An appropriate volume of EE2 stock solution was added to a 500 mL aqueous solution of either unbuffered water or pH 7.5 phosphate buffer (0.01 M) to give a concentration of 6.75×10^{-12} M (2 ppt). To this solution, an appropriate volume of either **1a** or **1b** stock solution was added to achieve a concentration of 8×10^{-8} M. Degradation was then initiated by addition of an appropriate volume of hydrogen peroxide stock solution to give 4.7×10^{-6}, 4.7×10^{-5}, 4.7×10^{-4} M (0.16, 1.6, 16 ppm). After 45 minutes, the reaction was quenched with catalase, concentrated with SPE, and eluted with ethanol. The organic mixture in ethanol was then concentrated to yield a final volume of 0.5 mL. The concentrations of each component in the reaction mixture are as follows: 6.75 pM (2 ppt) EE2, 80.0 nM (0.04 ppm) **1a** or **1b**, 4.70 µM (0.16 ppm), 47.03 µM (1.6 ppm), or 470.31 µM (16 ppm) H_2O_2.

5.4.7 Degradation of EE2 and Removal of Estrogenicity towards Fathead Minnows

5.4.7.1 Test organism

Fathead minnows for the in vivo study were bred and reared at Brunel University's U.K. Home Office licensed aquatic facility. Adult male fathead minnows (18 months old) were maintained in the tanks at 25°C ± 1°C with a photoperiod of 16:8 h light:dark. Fish were fed frozen brine shrimp twice a day and flake food once a day.

5.4.7.2 Experimental design

For the *in vivo* assay the four treatments were 1) negative control (no chemicals added), 2) positive control (EE2 only), 3) hydrogen peroxide treated EE2 (H_2O_2 and EE2) and finally 4) **1b**/peroxide-treated EE2 **(1b**, H_2O_2 and EE2). Each treatment regime consisted of two replicate tanks each with 8 male fathead minnows. The experimental set up consisted of eight 11 L glass aquaria each fed with continuous flow of water (Figure 10). Individual chemical stock solutions (EE2 in 0.1% ethanol in double distilled water (ddH_2O), 80μM TAML 2 in ddH_2O and H_2O_2 in ddH_2O) and filtered dechlorinated water were delivered to mixing chambers (2 L aspirator bottles, working volume 1.5 L) at a rate of 0.033 mL/min (via Watson Marlow multichannel peristaltic pump) and 33.33 mL/min (via gravity fed flow meter) respectively. This gave a thousand-fold dilution and nominal concentrations (without reaction) in the mixing vessels of 2 ppt EE2, 80 nM **1b**, 0.16 ppm H_2O_2. Water in the mixing vessels was continuously stirred by magnetic stirrer, and mixing time within the vessel was approximately 45 minutes before entering the tanks.

Each chemical stock (EE2, H_2O_2 and **1b**) was prepared and dosed separately so that the reaction only occurred in the mixing vessels (Figure 5-10).

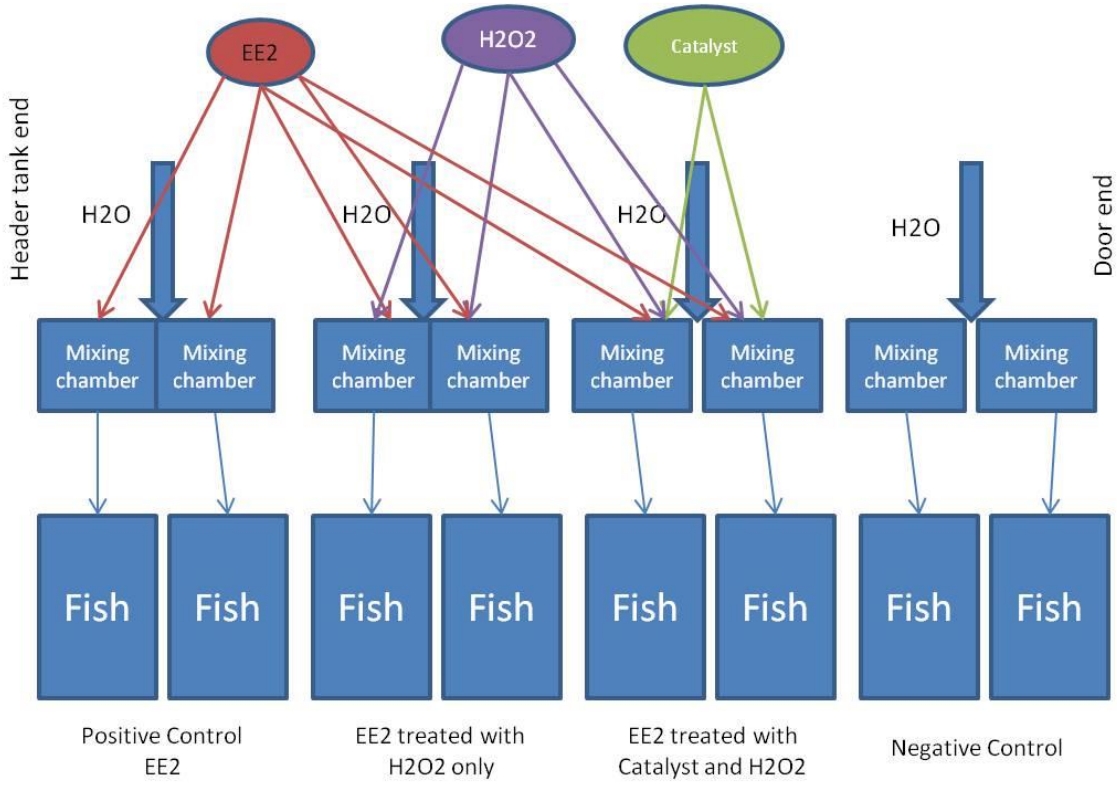

Figure 5-10. Diagram detailing the experimental setup for exposing fathead minnows to test solutions.

The fish (mean wet weight 3.9 ± 0.3 g) were placed into their tanks 1 week prior to chemical exposure to acclimatize. An additional 5 male fish were also included at this time to be sampled before chemical addition to provide baseline vitellogenin (VTG) data on day 0 of the assay. Dissolved oxygen (6.5 ± 0.4 mg/L), pH (8.3 ± 0.1) and water temperature (25.5 ± 0.2 °C) were recorded daily, as was the functioning of the dilution and dosing system. On days 6, 13 and 20 water samples were collected from the exposure

tanks for estrogenic (EE2 and estrogenic activity) analysis. Water samples were collected in large, 5 L silanized glass beakers and treated with catalase (Sigma-Aldrich) to a final concentration of 0.2 ppm to prevent further reaction. Water samples were split between LC-MS/MS EE2 analysis and YES analysis. Samples for EE2 analysis were fixed with an acidified copper nitrate ($HCl/Cu(NO_3)_2$) to prevent biological degradation. Analysis was conducted by LC-MS/MS with a limit of detection of 0.03 ppt. Technical replicates, blanks and EE2 spiked samples were also analysed (LC-MS/MS and YES).

On days 0 and 21 fish were sampled for plasma VTG. Fish were terminally anaesthetized with buffered MS-222 (Sigma-Aldrich) as approved by the U.K. Home Office (Animals (Scientific Procedures) Act 1986), and blood was collected from the caudal vein using a heparinized hemocrit tube. Plasma was collected by centrifugation at 7,000 g for 5 min at 4 °C and stored at -80 °C until analysis. Fish fork length and wet weight were measured and recorded for each fish sampled; condition factor was calculated as (fish weight/fork length^3) × 100. Plasma VTG concentrations were measured using a homologous VGT kit designed specifically for fathead minnows (Biosense Laboratories, Norway). Plasma samples were diluted 1:50, 1:5,000, and 1:500,000 and assayed in duplicate according to the manufactures protocol.

5.4.7.3 Statistical analysis

Data (fish metrics and EE2 concentrations) were tested for homogeneity of variance, parametric data was further analyzed using oneway ANOVA (followed by Least significant difference (LSD) post hoc analysis), non parametric data was analyzed using Kruskal-Wallis Test (followed by Mann-Whitney U test post hoc analysis). EE2 chemical

analysis results reported as <0.03ppt EE2 (i.e. lower than detection limit (LOD)) were treated as having half LOD (i.e. 0.015ppt EE2) for use in calculations of averages, standard error and statistical analysis. Data on biomarker responses were compared using oneway ANOVA followed by Turkey's post hoc test (VTG data were log10 transformed prior to analysis). For EE2 and VTG concentrations independent T-tests were also used to assess if any significant differences occurred between tanks of the same treatment regime (tank effects). Statistical analysis were conducted using SPSS version 18. Differences were considered significant at $p \leq 0.05$.

5.2.8 Degradation of estrogens in Activated Sludge Process (ASP) effluent

Effluent was received from activated sludge sewage treatment plants in the UK. Samples were divided into containers of 2.5 L volume and stored at room temperature. For samples tested at higher pH, the pH was adjusted with sodium hydroxide. Catalyst **1a** and H_2O_2 were added to each sample and allowed to react for the designated amount of time. The reaction was quenched by addition of a reducing agent (ascorbic acid) to stop the oxidation reaction after a pre-determined time. An aliquot (2.5 L) of the post reaction sample was transferred to a glass container, which was preserved with 3% v/v hydrochloric acid and 0.25% copper (II) nitrate. Samples were extracted using styrene-divinylbenzene solid phase extraction cartridges and cleaned up using aminopropyl solid phase cartridges followed by gel permeation chromatography and analysed using LC-MS/MS to determine the percent removal of the estrogens studied.

5.5 References

1. Maupin, M. A.; Kenny, J. F.; Hutson, S. S.; Lovelace, J. K.; Barber, N. L.; Linsey, K. S. Estimated use of water in the United States in 2010, *U.S. Geological Survey Circular 1405*, **2014**.

2. Kolpin, D. W.; Furlong, E. T.; Meyer, M. T.; Thurman, E. M.; Zaugg, S. D.; Barber, L. B.; Buxton, H. T. *Environ. Sci. Technol.* **2002**, *36*, 1202–1211.

3. Basile, T.; Petrella, A.; Petrella, M.; Boghetich, G.; Petruzzelli, V.; Colasuonno, S.; Petruzzelli, D. *Ind. Eng. Chem. Res.* **2011**, *50*, 8389–8401.

4. Jobling, S.; Nolan, M.; Tyler, C. R.; Brighty, G.; Sumpter, J. P. *Environ. Sci. Technol.* **1998**, *32*, 2498–2506.

5. Tyler, C. R.; Jobling, S. *Bioscience* **2008**, *58*, 1051.

6. Kidd, K. A.; Blanchfield, P. J.; Mills, K. H.; Palace, V. P.; Evans, R. E.; Lazorchak, J. M.; Flick, R. W. *Proc. Natl. Acad. Sci.* **2007**, *104*, 8897–8901.

7. Brian, W. R.; Sari, M. A.; Iwasaki, M.; Shimada, T.; Kaminsky, L. S.; Guengerich, F. P. *Biochemistry* **1990**, *29*, 11280–11292.

8. Johnson, A. C.; Williams, R. J. *Environ. Sci. Technol.* **2004**, *38*, 3649–3658.

9. Thorpe, K. L.; Cummings, R. I.; Hutchinson, T. H.; Scholze, M.; Brighty, G.; Sumpter, J. P.; Tyler, C. R. *Environ. Sci. Technol.* **2003**, *37*, 1142–1149.

10. Lange, A.; Paull, G. C.; Coe, T. S.; Katsu, Y.; Urushitani, H.; Iguchi, T.; Tyler, C. R. *Environ. Sci. Technol.* **2009**, *43*, 1219–1225.

11. Caldwell, D. J.; Mastrocco, F.; Anderson, P. D.; Länge, R.; Sumpter, J. P. *Environ. Toxicol. Chem.* **2012**, *31*, 1396–1406.

12. Hoover, R. N.; Hyer, M.; Pfeiffer, R. M.; Adam, E.; Bond, B.; Cheville, A. L.; Colton, T.; Hartge, P.; Hatch, E. E.; Herbst, A. L.; Karlan, B. Y.; Kaufman, R.; Noller, K. L.; Palmer, J. R.; Robboy, S. J.; Saal, R. C.; Strohsnitter, W.; Titus-Ernstoff, L.; Troisi, R. *N. Engl. J. Med.* **2011**, *365*, 1304–1314.

13. Andersen, H. R.; Schmidt, I. M.; Grandjean, P.; Jensen, T. K.; Budtz-Jørgensen, E.; Kjærstad, M. B.; Bælum, J.; Nielsen, J. B.; Skakkebæk, N. E.; Main, K. M. *Environ. Health Perspect.* **2008**, *116*, 566–572.

14. Chen, W. F.; Lin, H. Y.; Dai, S. A. *Org. Lett.* **2004**, *6*, 2341–2343.

15. Sen Gupta, S.; Stadler, M.; Noser, C. A.; Ghosh, A.; Steinhoff, B.; Lenoir, D.; Horwitz, C. P.; Schramm, K. W.; Collins, T. J. *Science* **2002**, *296*, 326–328.

16. Chanda, A.; Khetan, S. K.; Banerjee, D.; Ghosh, A.; Collins, T. J. *J. Am. Chem. Soc.* **2006**, *128*, 12058–12059.

17. Kundu, S.; Chanda, A.; Khetan, S. K.; Ryabov, A. D.; Collins, T. J. *Environ. Sci. Technol.* **2013**, *47*, 5319–5326.

18. Chahbane, N.; Popescu, D.-L.; Mitchell, D. A.; Chanda, A.; Lenoir, D.; Ryabov, A. D.; Schramm, K.-W.; Collins, T. J. *Green Chem.* **2007**, *9*, 49–57.

19. Mitchell, D. A.; Ryabov, A. D.; Kundu, S.; Chanda, A.; Collins, T. J. *J. Coord. Chem.* **2010**, *63*, 2605–2618.

20. Shen, L. Q.; Beach, E. S.; Xiang, Y.; Tshudy, D. J.; Khanina, N.; Horwitz, C. P.; Bier, M. E.; Collins, T. J. *Environ. Sci. Technol.* **2011**, *45*, 7882–7887.

21. Kundu, S.; Chanda, A.; Thompson, J. V. K.; Diabes, G.; Khetan, S. K.; Ryabov, A. D.; Collins, T. J. *Catal. Sci. Technol.* **2014**, 1775–1782.22. Denardo, M. A.; Mills, M. R.; Ryabov, A. D.; Collins, T. J. *J. Am. Chem. Soc.* **2016**, *138*, 2933–2936.

23. Auriol, M.; Filali-Meknassi, Y.; Adams, C. D.; Tyagi, R. D.; Noguerol, T. N.; Piña, B. *Chemosphere* **2008**, *70*, 445–452.

24. Lee, Y.; Escher, B. I.; Von Gunten, U. *Environ. Sci. Technol.* **2008**, *42*, 6333–6339.

25. Hwang, S.; Lee, D.-I.; Lee, C.-H.; Ahn, I.-S. *J. Hazard. Mater.* **2008**, *155*, 334–341.

26. Ngundi, M. M.; Sadik, O. A.; Yamaguchi, T.; Suye, S. *Electrochem. Commun.* **2003**, *5*, 61–67.

27. Routledge, E.; Sumpter, J. *Environ. Toxicol. Chem.* **1996**, *15*, 241–248.